

UNIVERSITA' DELLA CALABRIA

Dipartimento di FISICA

Scuola di dottorato

"SCIENZA E TECNICA BERNARDINO TELESIO"

Indirizzo

FISICA DEI SISTEMI COMPLESSI

Con il contributo di

COMMISSIONE EUROPEA, FONDO SOCIALE EUROPEO E REGIONE CALABRIA

CICLO

XXVI

TITOLO TESI

Astroparticle Physics as a Telescope for Solar Interior, Galactic and Extragalactic Structures

Settore Scientifico Disciplinare FIS/05

Direttore: Ch.mo Prof. Roberto Bartolino
Firma _____

Supervisore e Coordinatore: Ch.mo Prof. Vincenzo Carbone
Firma Vincenzo Carbone

Dottorando: Dott. Loris D'Alessi
Firma Loris D'Alessi




UNIVERSITA' DELLA CALABRIA

Department of Phyisics

Astroparticle Physics as a Telescope for Solar Interior, Galactic and Extragalactic Structures

---

A thesis submitted for the degree of
PHILOSOPHIAE DOCTOR (PHD)

Author:
D'Alessi LORIS

Supervisor:
Prof. Carbone VINCENZO

Director of Doctoral School:
Prof. Bartolino ROBERTO

"B. Telesio" School of Science and Technique, XXVI Cycle

December 2013

Alla mia Andreea

Abstract

Astroparticle physics provide a fundamental tool to investigate the astrophysical structures at different scales. In this thesis the results are presented of three years of research focused on time variations on solar neutrino flux, galactic cosmic rays and fine-structure constant as observed from quasar spectra. These topics are nowadays crucial to investigate structures which otherwise result difficult to probe. In particular time variations in solar neutrinos can give a real time description of the dynamics which take place in the inner regions of the Sun, while the study of galactic cosmic rays through the observation of muons produced by the interaction of the formers with the atmosphere, may give us precious informations on the interaction between TeV particles and heliospheric magnetic fields. Finally the recent observations of variations in the fine-structure constant value from the analysis of quasar absorption spectra, offer new possibilities to probe physical laws at cosmological scales. The thesis is structured as follows. In Chapter One are discussed quasi-biennial oscillations observed on solar neutrino flux and a phenomenological model is proposed to interpret the observed time variations. In the scenario described by the model, the interaction between solar neutrinos and solar matter mediated by magnetogravity modes, is modulated by a background magnetic field varying in time on quasi-biennial time scales. In Chapter Two the 11-yr component recently observed in cosmic muon data from Gran Sasso experiments of MACRO, LVD and Borexino has been reconstructed through the EMD analysis technique. In Chapter Three the data of fine-structure constant variations as observed in the quasar absorption spectra have been analyzed to search for temporal coherent structures. The thesis is completed by the description in appendix of a new algorithm based on Monte Carlo methods to assign a confidence interval to the IMFs extracted with the EMD analysis, and the application of this method to study the proton and neutrino distributions used in the OPERA experiment for the neutrino velocity measurement. Another appendix is dedicated to detailed description of the effects induced on the magnetogravity spectrum by a background magnetic field with a low-pass bandwidth, thus generalizing the theory of magneto-gravity modes in presence of a time-dependent background magnetic field.

Sommario

La fisica delle astroparticelle fornisce un fondamentale strumento di indagine per lo studio delle strutture astrofisiche a differenti scale. Nella presente tesi vengono presentati i risultati di tre anni di ricerca rivolte soprattutto sulle variazioni temporali nel flusso dei neutrini solari, nei raggi cosmici e nel valore della costante di struttura fine, quest'ultime osservate negli spettri di assorbimento delle quasar. Questi argomenti rivestono oggi un ruolo cruciale per indagare strutture altrimenti inaccessibili. In particolare le variazioni nel flusso dei neutrini solari sono in grado di fornire una descrizione in tempo reale delle dinamiche che hanno luogo nelle regioni interne del Sole, mentre lo studio dei raggi cosmici attraverso la misura del flusso dei muoni prodotti nell'interazione dei primi con l'atmosfera terrestre, permettono di ottenere informazioni sull'interazione tra le particelle con energie nell'ordine dei TeV e i campi magnetici eliosferici. In fine le recenti osservazioni sulle variazioni nella costante di struttura fine attraverso l'analisi degli spettri di assorbimento di quasar, aprono a nuove possibilità per lo studio delle leggi fisiche su scale cosmologiche. La tesi si struttura come segue. Nel Capitolo 1 sono discusse le oscillazioni quasi-biennali osservate nel flusso dei neutrini solari e un modello fenomenologico viene proposto all'origine di tali oscillazioni. Nello scenario descritto dal modello, l'interazione tra i neutrini solari e la materia degli strati interni del Sole attraverso i modi magnetogravitazionali, sarebbe modulata da un campo magnetico di background variabile nel tempo su tempi scala quasi-biennali. Nel Capitolo 2 il segnale undecennale recentemente osservato nei dati dei muoni cosmici misurati negli esperimenti del Gran Sasso di MACRO, LVD e Borexino è stato ricostruito attraverso la tecnica di analisi EMD. Nel Capitolo 3 i dati sulle variazioni della costante di struttura fine ottenuti dagli spettri di assorbimento delle quasar sono stati analizzati per ricercare delle strutture temporali coerenti. La tesi è completata da una descrizione in appendice di un nuovo algoritmo basato su un metodo Monte Carlo per l'assegnazione di un intervallo di fiducia alle IMF estratte con la tecnica EMD e l'applicazione di questo nuovo metodo per lo studio delle distribuzioni dei protoni e dei neutrini, utilizzate nell'esperimento di OPERA per la misura della velocità del neutrino. Un'altra appendice è dedicata alla dettagliata descrizione degli effetti indotti nello spettro dei modi magnetogravitazionali da un campo magnetico di background caratterizzato da una banda in frequenze di tipo passa-basso, generalizzando così la teoria dei modi magnetogravitazionali in presenza di un campo magnetico di background dipendente dal tempo.

Acknowledgements

I would like to express my sincere gratitude to my supervisor, Prof. Vincenzo Carbone. Throughout these six years of collaboration, since my work on the first level degree thesis, our fruitful discussions helped me to become a scientist. During this adventure I had the opportunity to find a precious collaborator and a sincere friend in Antonio Vecchio.
I thank Carlos Peña Garay for proposing me to work on several ideas which contributed to enrich the structure of this project.

I would like to aknowledge hospitality in Valencia during my period at Instituto de Física Corpuscolar (IFIC).

This thesis is partially supported by grant of the European Commission, European Social Fund and Regione Calabria. The author is the only responsible of this thesis and the European Commission and Regione Calabria decline every responsability about the use which could be done of the informations here included.

I would like to thank the Research Group of Astrophysics and Plasma Physics as well as the whole Department of Physics of UNICAL for the friendly and stimulating research environment.

I thank all my friends for their support and my family for their love.

Contents

List of Figures

List of Tables

Chapter 1

Solar Neutrinos

1.1 Standard Solar Model

The Standard Solar Model describes the Sun as a gas sphere in mechanical equilibrium with the gravitational field generated by itself [1, 2]. In the model the effects induced by differential rotation and magnetic fields are neglected. Within this assumption, the equilibrium between atmospheric pressure and gravity forces is expressed by the equation of motion, which can be written in the form

$$\frac{d}{dr}P\left(r\right) = -G\frac{M\left(r\right)\rho\left(r\right)}{r^2} \tag{1.1}$$

where $P\left(r\right)$ denotes the pressure at distance r from the center of the Sun, G is the gravitational constant, M and ρ are the mass and density of matter respectively.
The mass included in a sphere of radius r is given by

$$M\left(r\right) = 4\pi\int_0^r dr' r'^2 \rho\left(r'\right) \tag{1.2}$$

In its differential form, Eq. (1.2) becomes

$$\frac{d}{dr}M\left(r\right) = 4\pi r^2 \rho\left(r\right) \tag{1.3}$$

By combining Eq. (1.3) with Eq. (1.1), we obtain an equation which relates pressure with density, that is

$$\rho = -\frac{1}{4\pi G}\frac{1}{r^2}\frac{d}{dr}\left(\frac{r^2}{\rho}\frac{dP}{dr}\right) \tag{1.4}$$

A particular class of solutions of the equation can be found assuming a functional dipendence of P versus ρ of the form:

$$P = A\rho^{\gamma}$$

where A and γ are constants. The substitution of P in Eq. (1.4) with the above expression gives the Lane-Emden equation, which solutions give an approximate dependence of the variables from r. In order to have a more accurate model, the equation of state for the solar plasma need to be considered, which in its general form can be written as

$$P = P\left(\{X_i\}, \rho, T\right) \tag{1.5}$$

where T is the temperature (as a function of radius) and $\{X_i\}$ denotes a set which elements are the mass fraction of the different elements which constitute the Sun. For simplicity only mass fraction of hydrogen, helium and the mass fraction of all the remnants elements are considered. The mass fraction of hydrogen and helium are indicated with X and Y, respectively, while the mass fraction of the other elements is indicated by Z and is related to X and Y by the condition $X + Y + Z = 1$.
The equation of state introduces the new variables of temperature and concentration of the different chemical species, to determine the evolution of which other equations are required. The equation of temperature depends by which mechanism is responsible of the energy transport.
In the inner regions of the Sun the energy propagates as radiation. The flux of energy here is proportional to the gradient of temperature

$$\mathbf{f} = -A\nabla T \tag{1.6}$$

where A depends on the opacity of matter. We will explicit this dependence in the definitive expression for gradient temperature without demonstration. If we define the luminosity as the energy flux through a shell at radius r for unit time, that is

$$L\left(r\right) = 4\pi r^2 f\left(r\right)$$

we can write Eq. (1.6) in the form

$$\left[\frac{d}{dr}T\right]_{rad} = -\frac{3}{64\pi}\frac{L}{\sigma r^2}\frac{\kappa_R \rho}{T^3} \tag{1.7}$$

where the coefficient of proportionality has been written as a function of Rosseland opacity coefficient κ_R and σ is the Stefan-Boltzmann constant.
In the upper regions of the Sun convective motions of the matter become the main responsible of the conduction of energy. In this region, temperature gradient can be expressed as function of gas pressure

$$\left[\frac{d}{dr}T\right]_{conv} = \frac{dP}{dr}\frac{T}{P}\nabla_S = -\rho g\frac{T}{P}\nabla_S \tag{1.8}$$

where g is the gravitational field and $\nabla_S \equiv (\partial \ln T/\partial \ln P)_S$, with the pedix S denoting derivation evaluated at constant entropy.
If we introduce the pressure gradient into Eq. (1.7) by obtaining ρ from Eq. (1.1) and by defining ∇_{rad} as

$$\nabla_{rad} = \frac{3}{64\pi}\frac{L}{\sigma}\frac{\kappa_R P}{GMT^4} \tag{1.9}$$

then we can express the transition from radiative to convective region through the condition $\nabla_{rad} = \nabla_{conv}$.
The last equation needed to close the system is the equation for the luminosity. This is obtained by the energy conservation law, which can be expressed in the form

$$\frac{\partial u}{\partial t} + \nabla \cdot \mathbf{f} = \rho\epsilon \tag{1.10}$$

where u is the energy density and ϵ is the energy produced (or lost) per unit mass and time.
The energy is produced by the fusion of 4 protons and 2 electrons which gives a nucleus of ^4He and energy through the reaction

$$4p + 2e^- \rightarrow^4 He + 2v_e + Q \tag{1.11}$$

where $Q = 26.73$ MeV is the energy released from the difference between the total mass given by the initial particles and the total mass of the final particles. The fusion of protons and electrons is obtained through two cycles, namely *pp*-chains and CNO bi-cycles. The former is responsible for 98.4% of energy release, the latter provides the remnant 1.6% energy output. This difference is due to the temperature in the core of the Sun, which value ($\sim 15 \cdot 10^7 K$) is smaller than that is required from CNO cycle to be more significant ($\sim 18 \cdot 10^7 K$) [3, 4]. Carbon, nitrogen and oxygen involved in the cycle act more as catalysts to lead the fusion. The steps of the different chains are summarized in Tab. 1.1 [2].

1.2 Solar Neutrinos

The energy produced in the nuclear reactions are transported through photons and neutrinos. The latter has a crucial role in the investigation of the interior of the Sun. This importance is due to the fact that they interact weakly with matter, so that, while a photon produced in the core of the Sun, because of its several interactions with matter, needs 10^4 yr to arrive at the surface[1], a neutrino requires only 8 min to arrive at the Earth, i.e. the

[1]The time needed to a photon to arrive at the solar surface can be estimated assuming that the elastic scattering processes between the photon and the electrons in the Sun (Compton scattering) result in a random-walk pattern and the total time interval elapsed from the center to the photosphere is given by $T \sim N^2 l/c$, where $N = R_{sun}/l$ and l is the mean free path for the photon in the Sun which is of ~ 1 cm.

TABLE 1.1: Nuclear reactions in the Sun (adapted from [2]). In the third and fourth columns Q and $\langle Q_\nu \rangle$ represent the energy (in MeV) released from the reaction and the mean neutrino's energy, respectively. In the fifth column, are indicated the name used to label neutrinos produced in the specific reaction.

Chain	Reaction	Q(MeV)	$\langle Q_\nu \rangle$(MeV)	Label
ppI	$p + p \rightarrow {}^2H + e^+ + \nu_e + \gamma$	1.442	0.265	pp
	$p + p + e^- \rightarrow {}^2H + \nu_e$	1.442	1.442	pep
	${}^2H + p \rightarrow {}^3He + \gamma$	5.49	-	
	${}^3He + {}^3He \rightarrow {}^4He + 2p + \gamma$	12.86	-	
ppII	${}^3He + {}^4He \rightarrow {}^7Be + \gamma$	1.586	-	
	${}^3Be + e^- \rightarrow {}^7Li + \nu_e$	0.862 (90%)	0.862	^{7}Be
		0.384 (10%)	0.384	^{7}Be
	${}^7Li + p \rightarrow {}^4He + {}^4He + \gamma$	17.347	-	
ppIII	${}^7Be + p \rightarrow {}^8B + \gamma$	0.137	-	
	${}^8B \rightarrow {}^4He + {}^4He + \nu_e + \gamma$	17.98	6.710	^{8}B
	${}^3He + p \rightarrow {}^4He + e^+ + \nu_e + \gamma$	19.795	9.625	hep
CN	${}^{12}C + p \rightarrow {}^{13}N + \gamma$	1.943	-	
	${}^{13}N \rightarrow {}^{13}C + e^+ + \nu_e$	2.221	0.7067	^{13}N
	${}^{13}C + p \rightarrow {}^{14}N + \gamma$	7.551	-	
	${}^{14}N + p \rightarrow {}^{15}O + \gamma$	7.297	-	
	${}^{15}O \rightarrow {}^{15}N + e^+ + \nu_e$	2.754	0.9965	^{15}O
	${}^{15}N + p \rightarrow {}^{12}C + \alpha$	4.966	-	
NO	${}^{15}N + p \rightarrow {}^{16}O + \gamma$	12.128	-	
	${}^{16}O + p \rightarrow {}^{17}F + \gamma$	0.600	-	
	${}^{17}F \rightarrow {}^{17}O + e^+ + \nu_e$	2.762	0.9994	^{17}F

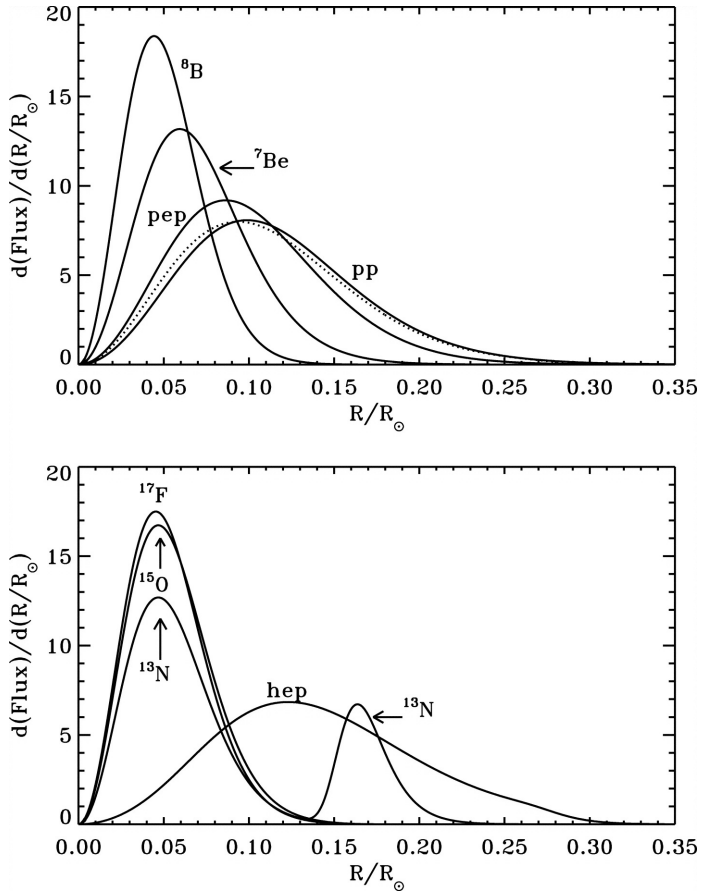

FIGURE 1.1: Solar neutrino flux versus radius for neutrinos produced in pp-chains (upper panel) and CNO-cycle (lower panel) [5]. Dotted line in the upper panel represents the production profile for the solar luminosity.

travel time needed to cover Sun-Earth distance at a velocity close to the speed of light, allowing a real time investigation of the properties of the Sun.

As shown in Tab. 1.1, there are 8 sources of neutrinos. Their flux as a function of solar radius is shown in Fig. 1.1, while their energy spectrum is shown in Fig. 1.2. Their energies cover a range from few hundreds keV of proton-proton reaction in the *ppI* chain up to ~ 20 MeV of *hep* reaction. In the next sections the several experiments dedicated to their detection will be described. All of them measure a flux of electron neutrinos smaller than the flux expected from SSM calculations. This difference is known as "Solar Neutrino Problem", which actually has been solved in favour of the MSW mechanism.

1.2.1 The Michaelev-Smirnov-Wolfenstein Effect

The basic principles for the Micheyev-Smirnov-Wolfenstein effect (MSW or matter effect) are that

- the neutrino flavour eigenstates are not the same of that of mass;

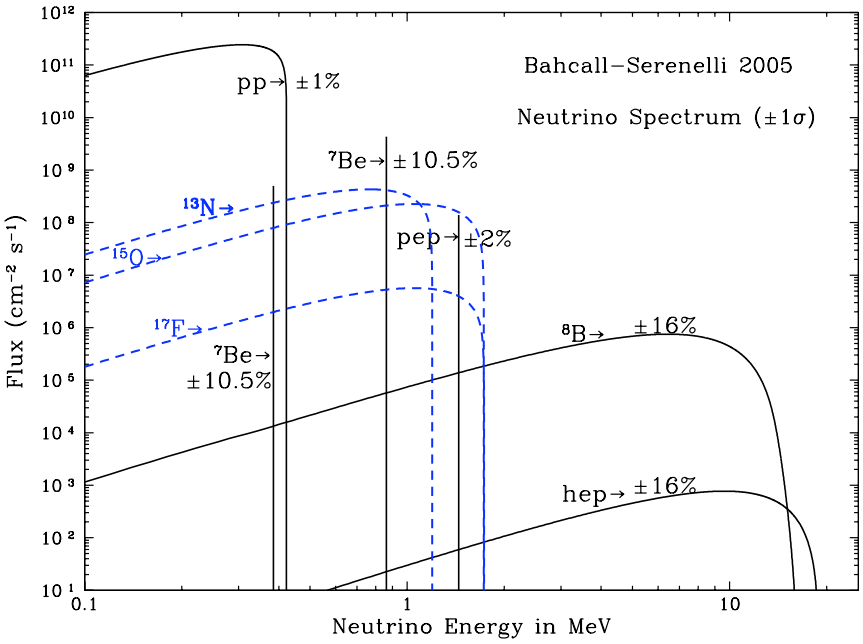

FIGURE 1.2: Solar neutrino energy spectrum from SSM BS05(GS98) [6].

- neutrinos interact with the particles of medium through coherent forward elastic scattering. The global effect of these interactions modifies the evolution of neutrinos flavour states.

Under these assumptions, and considering for simplicity two possible eigenstates for flavour, the transformation from one basis of eigenstates to the other can be written

$$\begin{pmatrix} \psi_e \\ \psi_x \end{pmatrix} = \begin{pmatrix} \cos(\theta_V) & \sin(\theta_V) \\ -\sin(\theta_V) & \cos(\theta_V) \end{pmatrix} \begin{pmatrix} \psi_1 \\ \psi_2 \end{pmatrix} \tag{1.12}$$

where θ_V is the mixing angle in vacuum.[2] Here we will resume brefly the main results of the model. For more details see [1] and [11]. The eigenstate of neutrino flavour can be written in terms of mass eigenstates as

$$|\psi_e\rangle = \cos(\theta_V)\,|\psi_1\rangle + \sin(\theta_V)\,|\psi_2\rangle \tag{1.13}$$

The time evolution of electron neutrino eigenstate behaves[3]:

[2]The hypotesis of neutrino oscillation was formulated for the first time by B. Pontecorvo, in analogy with K and $\bar{K}$ oscillations [7, 8]. The theory of interaction between neutrinos and high density matter was formulated by Wolfenstein [9], while the effect of varying density matter was studied by Mikheyev and Smirnov [10].

[3]Here and throughout the dissertation, the quantum mechanical calculations are performed using natural units ($\hbar = c = 1$).

$$|\psi_e\rangle = \cos(\theta_V)\, e^{-iE_1 t}\, |\psi_1\rangle + \sin(\theta_V)\, e^{-iE_2 t}\, |\psi_2\rangle \tag{1.14}$$

For ultrarelativistic neutrinos, taking into account the energy-momentum relation $E^2 = p^2 + m^2$ and using the approximation $E \simeq p$, the energy of the i-th neutrino can be written at first order in m_i^2 in the form:

$$E_i = E + \frac{m_i^2}{2E} \tag{1.15}$$

The energy of the two mass eigenstate are thus related through the condition

$$E_2 - E_1 = \frac{\Delta m^2}{2E} \tag{1.16}$$

with $\Delta m^2 \equiv m_2^2 - m_1^2$ and where we have assumed, without lack of generality, that $m_2 > m_1$. In terms of E_1 and Δ defined as $\Delta \equiv E_2 - E_1$, the time evolution of flavour eigenstate is described by Schrödinger equation

$$i\frac{d}{dt}\begin{pmatrix}\psi_e \\ \psi_x\end{pmatrix} = \left[\frac{\Delta}{2}\begin{pmatrix}-\cos(2\theta_V) & \sin(2\theta_V) \\ \sin(2\theta_V) & \cos(2\theta_V)\end{pmatrix} + \left(E_1 + \frac{\Delta}{2}\right) I_2\right]\begin{pmatrix}\psi_e \\ \psi_x\end{pmatrix} \tag{1.17}$$

where I_2 is the identity matrix of the second order. The second term in brakets can be eliminated by a shift in energy. When a neutrino pass through a layer with an high matter density, its path is influenced such as the particle is traveling in a region with refraction index n. In the presence of matter, Eq. (1.17) becomes

$$i\frac{d}{dr}\begin{pmatrix}\psi_e \\ \psi_x\end{pmatrix} = \begin{pmatrix}-\frac{\Delta}{2}\cos(2\theta_V) + V_e & \frac{\Delta}{2}\sin(2\theta_V) \\ \frac{\Delta}{2}\sin(2\theta_V) & \frac{\Delta}{2}\cos(2\theta_V) + V_n\end{pmatrix}\begin{pmatrix}\psi_e \\ \psi_x\end{pmatrix} \tag{1.18}$$

where $V_e = G_F(2N_e - N_n)/\sqrt{2}$ and $V_x = -G_F N_n/\sqrt{2}$. We consider for simplicity, $N_n = 0$. To evaluate the probability that a neutrino produced as electronic is detected at time t at the same flavour state, we have to take into account the electron density profile. Integrating Eq. (1.18) we obtain [12]

$$P_{ee} \equiv |\langle\psi_e(t)\,|\psi_e(0)\rangle|^2 = \frac{1}{2} + \frac{1}{2}(1 - P_{jump})\cos 2\theta_M^{(i)} \cos 2\theta_V \tag{1.19}$$

where $\theta_M^{(i)}$ is the oscillation angle in the presence of matter and is given by the relation

$$\tan 2\theta_M = \frac{\tan 2\theta}{1 - \frac{V_e}{\Delta\cos 2\theta_V}} \tag{1.20}$$

in this case the matter mixing angle is evaluated at the production point. P_{jump} represents the probability of transitions from ν_1 to ν_2. This probability is negligible in the Sun, so that the mass eigenstates evolves indipendently. The smooth profile with which the matter

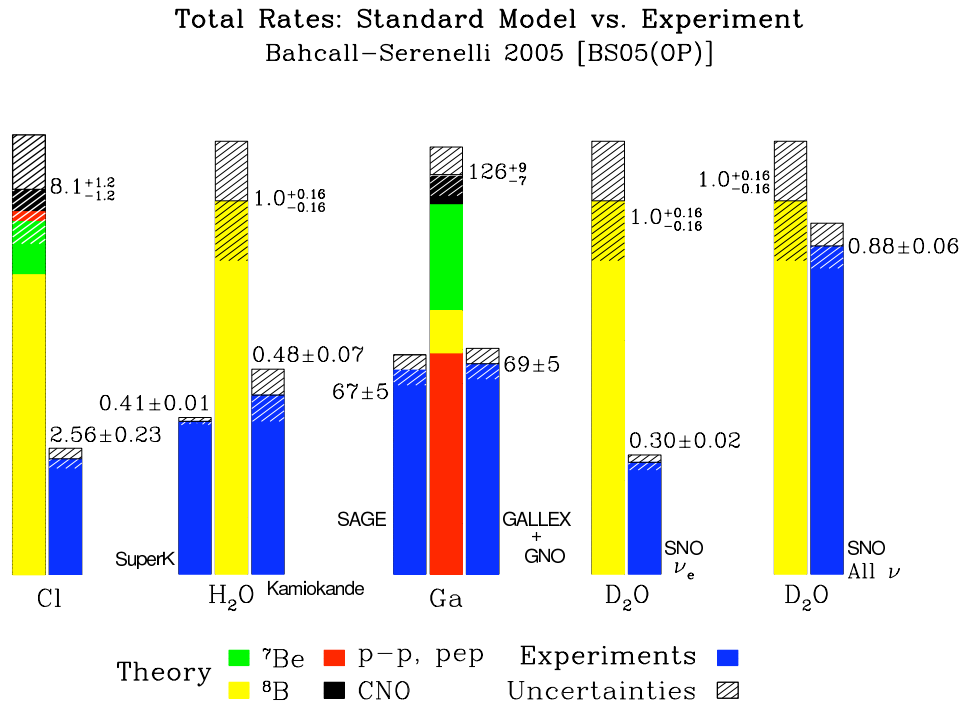

FIGURE 1.3: Histograms of the predicted versus observed integrated neutrino flux for different experiments [13]. For more details see section "Viewgraphs" at web site and reference therein.

density varies in the Sun allows the existence of a particular region where $\cos(2\theta_V) = V_e/\Delta$. This region, which depends on the energy of neutrinos, is called *resonant position*. At the resonance the probability of flavour conversion is maximal.

1.3 Solar Neutrino Detectors

In this section we will describe the neutrino detectors. The analysis of their data in the scenario of the MSW mechanism, toghether with KamLAND experiment results,[4] allows an estimation of neutrino parameters m_{12} and θ_{12} which value are measured [15]: $\Delta m_{12} = 7.50^{+0.18}_{-0.21} \times 10^{-5} eV^2$ and $\tan\theta_{12} = 0.457^{+0.038}_{-0.025}$, thus favouring the Large Mixing Angle (LMA) solution.

[4]We do not describe here the KamLAND experiment, since it is properly dedicated to the detection of antineutrino $\bar{\nu}_e$ coming from japanese nuclear reactors [14]. Their data can be combined with solar neutrino data to study neutrino oscillations in the three neutrino system.

1.3.1 Homestake

The Homestake Clorine Solar Neutrino Experiment was a 4400 mwe underground experiment located in Homestake Gold Mine at Lead, South Dakota. The detector took data from 1970 to 1994 [16, 17]. Here a tank of 6.1 m diameter and 14.6 m length was filled with 615 tons of tetrachloroethylene (C_2Cl_4). Elecron neutrinos arriving from the Sun were detected by means of their interaction with chlorine through the reaction

$$\nu_e + {}^{37}Cl \rightarrow {}^{37}Ar + e^- \tag{1.21}$$

The energy threshold for reaction is $E_{th} = 0.814$ MeV, allowing the detection of neutrinos produced in all neutrino sources, except that produced in *pp* reaction of *ppI* chain, which have energy less than 0.420 MeV. The argon produced were extracted by purging the tank with helium and collected in a proportional counter of 3 cm in length and 0.5 cm in diameter. ${}^{37}Ar$ decays by electron capture producing Auger electrons with total energy of 2.823 keV. Background comes mainly from ${}^{37}Ar$ produced from (p, n) reactions by protons formed in cosmic-ray muon interactions (0.01 ${}^{37}Ar$ atoms/day) and by rocks radioactivity (0.02 ${}^{37}Ar$ atoms/day). The average ${}^{37}Ar$ production rate for 108 solar runs is $0.478 \pm 0.03_{stat} \pm 0.029_{syst}$ atoms/day, which corrensponds to $2.56 \pm 0.16_{stat} \pm 0.16_{syst}$ SNU (Solar Neutrino Unit, or number of interactions per 10^{36} atoms) [17], which is about 1/3 of the flux predicted by SSM.

1.3.2 SAGE and GALLEX/GNO

Both the experiments of SAGE [18] and GALLEX/GNO [19, 20, 21, 22, 23, 24] are radiochemical experiments, where the target are gallium atoms, which interact with neutrinos through the reaction

$$\nu_e + {}^{71}Ga \rightarrow {}^{71}Ge + e^- \tag{1.22}$$

${}^{71}Ge$ produced in the reaction is collected in proportional counters where it deacays for electron capture. From the Auger electrons and X-rays spectrum produced from its decay, two peaks at 1.2 keV (L peak) and 10.4 keV (K peak) are measured. The energy threshold for the reaction ($E_{th} = 0.2332$ MeV) allows the detection of all electron neutrinos produced in the Sun. The main contribution to the flux comes from *pp* neutrinos.
The Soviet-American Gallium Experiment (SAGE) was located 4700 mwe underground in Mt. Andyrchi, in the northern Caucasus mountains of Russia. For the experiment 50 tonnes of molten gallium were used. The result for 168 runs from January 1990 to December 2007 is $65.4^{+3.1}_{-3.0}(\text{stat})^{+2.6}_{-2.8}(\text{syst})$ SNU [18].

GALLiumExperiment was installed at Laboratori Nazionali del Gran Sasso, in Italy, which are located 3800 mwe undergound. The experiment was operative from May 1990 to January 1997 (65 runs). After the improvements on the extraction process it starts the second phase of the experiment, called GNO (Gallium Neutrino Observatory), which collected 58 runs from May 1998 to September 2003. For both the phases of the experiment the target are 30.3 t of gallium in the form of a concentrated $GaCl_3 - HCl$ solution. For Gallex experiment the flux evaluated through a pulse-shape analysis gives a result of $73.4^{+6.1+3.7}_{-6.0-4.1}$ SNU [24], while the result for GNO the flux was $62.9^{+5.5+2.5}_{-5.3-2.5}$ SNU [23].
The combined results from both SAGE and GALLEX/GNO experiments gives 66.1 ± 3.1 SNU [18], which corrensponds to about 50% of the expected flux.

1.3.3 KamiokaNDE and SuperKamiokande

KamiokaNDE (Kamioka Neutrino Decay Experiment) [25] and its successor Super-Kamiokande [26, 27, 28] are Cerenkov light detection experiments situated 2700 mwe under Kamioka mine in Gifu Prefecture in Japan.
Both the experiments detect Cerenkov light emitted by electrons which have interacted with neutrinos through the elastic scattering process

$$\nu + e^- \rightarrow \nu + e^- \tag{1.23}$$

Neutrinos involved in the process may be of any kind of flavour. Electron neutrinos can interact also via charged current, so that the cross section for electron neutrinos is higher (of a factor of ~ 6) than that for muonic or tauonic neutrinos.
KamiokaNDE was previously dedicated to protons decay to test Grand Unification Theories in 80s, then was upgraded to be able to detect solar neutrinos. In its definitive version KamiokaNDE consisted of a tank of 15.6 m in diameter and 16.1 m in height, containing 3000 tons of pure water monitored by 848 20-inches PMTs. It measured ^8B neutrino flux of energy above an energy threshold of 7 MeV from 1987 to 1995. The total flux was of $2.80 \pm 0.19_{stat} \pm 0.33_{syst} \times 10^6$ cm^{-2}s^{-1} [25].
SuperKamiokande consists of a tank of 39.3 m in diameter and 41.4 m in height, filled with 50000 tons of water monitored by 11146 20-inches PMTs. Other 1885 8-inches PMTs are installed in the outer detector, acting as veto detector for incoming muons and as a water shield from neutrons and γ-rays coming from the surroundings rocks. The improved statistics respect to KamiokaNDE allows to discriminate the neutrino energy spectrum shape.
The experiment started in April 1996 and is currently operating. The ^8B neutrino flux of energy range $5 \div 20$ MeV, for data until August 2008, is $2.32 \pm 0.04_{stat} \pm 0.05_{syst} \times 10^6$ cm^{-2}s^{-1} [28].

1.3.4 SNO

Sudbury Neutrino Observatory (SNO) [29, 30, 31, 32, 33] is another water Cerenkov detector. It is located 6010 mwe underground at INCO, Ltd. Creighton Mine near Sudbury, Ontario, Canada. It consists of a 12 m in diameter acrylic vessel, filled with 1000 t of ultrapure heavy water. The structure is inside a 34 m high barrel-shaped cavity of 22 m maximum in diameter, filled with 6500 t of ultrapure water. A stainless steel structure of 17.8 m supports 9456 20-cm PMTs.
The experiment detects solar neutrinos through 3 processes:

$$\begin{aligned} \nu_e + d &\rightarrow p + p + e^- \qquad \text{(CC)} \\ \nu_x + e^- &\rightarrow \nu_x + e^- \qquad \text{(ES)} \\ \nu_x + d &\rightarrow p + n + \nu_x \qquad \text{(NC)} \end{aligned} \tag{1.24}$$

where in brackets is specified the kind of interaction, i.e. charged current (CC), elastic scattering (ES) and neutral current (NC). Neutrons produced in NC channel (E_{th} = 2.2 MeV) are detected by means of their interaction with deuterium through the reaction $n + d \rightarrow t + \gamma$, where are produced a nucleus of tritium and a photon of 6.25 MeV. Neutrino flux detected from NC reaction corresponds to the total flux of solar neutrinos produced mainly in the ^8B reaction.
The experiment started on November 2, 1999. In second phase, started on July 26, 2001, 2000 kg of $NaCl$ were added, allowing an improvement in the neutron detection efficiency and the ability to statistically separate the NC and CC signals. On November 27, 2004 started a third phase where 36 strings of ^3He proportional counters where deployed in the D_2O. With this addition, the rate of NC events from $^2H\,(n,\gamma)^3\,H$ reaction was significantly suppressed and the new measurements of the CC, ES and NC rates resulted in a reduced correlation between the fluxes. The results of the three phase are summirized in Tab. 1.2. The total rate of neutrinos, as measured through NC events, is in agreement with the expected flux, thus confirming a flavour change in their travel to the Earth.

1.3.5 Borexino

The Borexino detector [34, 15] is a scintillator liquid based detector. It is located at Laboratori Nazionali del Gran Sasso, in Italy. The target consists of 278 t of pseudocumene (1,2,4-trimethylbenzene), doped with 1.5 g/l of the fluor PPO (2,5-diphenyloxazole), contained in a spherical transparent 8.5 m in diameter nylon Inner Vessel (IV). It is shelded by two buffers with PC (323 and 567 t) doped with 5.0 g/l DMP (dimethylphtalate) which induce scintillaiton in PC. Both scintillator and buffers are contained in a stainless steel sphere of 13.7 m in diameter, where 2212 8" PMTs are supported, which monitor scintillation light coming from the central region. All the apparatus is situated in a tank of 18

TABLE 1.2: ^{8}B neutrino flux measured by SNO detector in the different phases of the experiment.

Phase	Measured Flux (10^6 cm^{-2} s^{-1})
D_2O [30]	$\Phi_{CC}^{SNO} = 1.76^{+0.06}_{-0.05}\,(stat)^{+0.09}_{-0.09}\,(syst)$
	$\Phi_{ES}^{SNO} = 2.39^{+0.24}_{-0.23}\,(stat)^{+0.12}_{-0.12}\,(syst)$
	$\Phi_{NC}^{SNO} = 5.09^{+0.44}_{-0.43}\,(stat)^{+0.46}_{-0.43}\,(syst)$
Salt [31]	$\Phi_{CC}^{SNO} = 1.59^{+0.08}_{-0.07}\,(stat)^{+0.06}_{-0.08}\,(syst)$
	$\Phi_{ES}^{SNO} = 2.21^{+0.31}_{-0.26}\,(stat) \pm 0.10\,(syst)$
	$\Phi_{NC}^{SNO} = 5.21 \pm 0.27\,(stat) \pm 0.38\,(syst)$
^{3}H [33]	$\Phi_{CC}^{SNO} = 1.67^{+0.05}_{-0.04}\,(stat)^{+0.07}_{-0.08}\,(syst)$
	$\Phi_{ES}^{SNO} = 1.77^{+0.24}_{-0.21}\,(stat)^{+0.09}_{-0.10}\,(syst)$
	$\Phi_{NC}^{SNO} = 5.54^{+0.33}_{-0.31}\,(stat)^{+0.36}_{-0.34}\,(syst)$

m in diameter and 16.9 m in height. The tank is instrumented with 208 PMTs that detect the Cherenkov light emission from cosmic ray muons. The experiment started in May 16, 2007. After 740.7 days, the flux of ^7Be neutrinos measured is $46.0 \pm 1.5(\text{stat})^{+1.5}_{-1.6}(\text{syst})$ cpd/100t [15].

1.4 Solar Neutrino Red-Shift

Neutrinos produced in *pp* and *CNO* cycles have a continuum spectrum, except for ^7Be and *pep* neutrinos, which are produced for electron capture, so that the energy of neutrino produced in these reactions is well defined. In particular ^7Be pass through nuclear transition from ^7Be ground state to ^7Li ground state (with a corresponding neutrino energy of $q = 861.8$ keV as measured in lab) or to ^7Li excited state ($q = 384.3$ keV). The former has an higher branching ratio (89.7%) than the latter (10.3%). The higher energy and branching ratio of neutrinos produced in the transition to ground state makes this process experimentally easier to study. According to Bahcall [35], we refer to g.s. neutrinos as the neutrinos produced in the ground-state to ground-state nuclear transition and to e.s. neutrinos as that produced in the ground-state to excited-state nuclear transition. The

energy of neutrinos produced in the *pep* termination is $q = 1442$ keV. The rate for the line-producing *pep* reaction is only two-tenths of a percent of the rate of *pp* reaction.
Neutrinos produced in ^7Be and *pep* reactions experience a Doppler effect due to the relative motion of the center of mass. This effect results in a broading of neutrino energy spectrum shape which can be used to measure the central temperature of the Sun, as it will shown in the next sections.

1.4.1 ^7Be Neutrino Energy Spectrum

In this subsection we will resume the results of Bahcall model for the ^7Be neutrino energy spectrum [35]. An analogous mathematical apparatus will be used to study the *pep* neutrino energy spectrum in the next subsection. The energy of ^7Be neutrinos depends whether the electron capture from ^7Be nuclei occurs in laboratory or in the Sun [35]. The difference lies in the different conditions in which the mechanism takes place. In laboratory conditions, atomic binding energies for ^7Be and ^7Li have to be taken into account in the evaluation of neutrino energies, while in the Sun, because of the high temperatures in the core, ^7Be atoms are highly ionized, so that the electrons are captured essentially from continuum orbits.
For both the environments in which electron capture occurs, energy conservation is expressed through the condition

$$E_f - E_i = \Delta M + K\left(^7Be\right) + K\left(e\right) - q - K\left(^7Li\right) + a\left(^7Be\right) - a\left(^7Li\right) = 0 \tag{1.25}$$

where $K\left(\cdot\right)$ denotes kinetic energy and $a\left(\cdot\right)$ the atomic binding energy.
For laboratory decays, kinetic energies of electron and ^7Be can be neglected, while the difference in atomic binding energies is

$$a_{lab}\left(^7Be\right) - a_{lab}\left(^7Li\right) = -0.195 \text{ keV} \tag{1.26}$$

Neutrino energies for ground and bound states are

$$q_{lab}\left(g.s.\right) \cong 861.84 \text{ keV} \tag{1.27}$$

and

$$q_{lab}\left(e.s.\right) \cong 384.28 \text{ keV} \tag{1.28}$$

For decays which occur in the Sun from continuum orbits, we have to remove the contribution from atomic binding energies, thus obtaining

$$q_{cont,star}\left(g.s.\right) = q_{lab} - \left[a_{lab}\left(^7Be\right) - a_{lab}\left(^7Li\right)\right] = 862.04 \text{ keV} \tag{1.29}$$

The value for (e.s.) is $q_{cont,star}\,(e.s.) = 384.43$ keV. For bounding orbit capture in the Sun, one has to add the contribution from atomic binding energies averaged over the Sun

$$q_{bound,star} = q_{count,star} + \left\langle a_{lab}\left({}^7Be\right) - a_{lab}\left({}^7Li\right)\right\rangle = 862.04 \text{ keV} \tag{1.30}$$

The result for (g.s.) and (e.s) are $q_{bound,star}\,(g.s.) = 861.98$ keV and $q_{bound,star}\,(e.s.) = 384.38$ keV, respectively.

Let us focus on the electron capture from continuum orbits, which is the dominant process in the Sun. The rate for continuum capture is proportional to the squared modulus of the element matrix for β-decay hamiltonian

$$H_\beta = \frac{G_F}{\sqrt{2}}\left[\bar{\psi}_\nu \gamma_\alpha\left(1+\gamma_5\right)\psi_e\right]\left[\bar{\psi}_n \gamma_\alpha\left(C_V - C_A\gamma\right)\psi_p\right] \tag{1.31}$$

Then the partial transition probability to undergo electron capture can be written as

$$\frac{1}{(2\pi)^2}\sum_i \bar{\sum_f} \left|\langle f|\, H_\beta\, |i\rangle\right|^2 \delta^{(4)}\left(p_f - p_i\right) d^3\mathbf{q} d^3\mathbf{p}_7 \tag{1.32}$$

where $\mathbf{q}$ and $\mathbf{p}_7$ denotes neutrino and ${}^7Li$ momenta, respectively. The initial state is taken as the eigenstate of the hamiltonian with Coulomb potential, that is the solution of the equation

$$\frac{1}{r}\frac{d^2}{dr^2}\left(r\,\psi\right) + \left(E - \frac{Z_1 Z_2 e^2}{r}\right)\psi = 0 \tag{1.33}$$

It is useful to normalize the solutions of Eq. (1.33) respect to the Coulomb factor

$$C = \frac{2\pi\eta}{\exp\left(2\pi\eta\right) - 1} \tag{1.34}$$

where $\eta = \alpha Z_1 Z_2 / v$, with v center-of-mass velocity. This normalization is usefull because the main contribution of the reduced mass energy is included in this factor. Al the terms included in the matrix element can be expressed as a product of C times a function of center of mass energy, which we denote with $S\left(E\right)$ and that coincides with the *astrophysical factor*. In this work, S can be considered as varying slowly respect to E, so that it can be considered constant, i.e. $S\left(E\right) \simeq S\left(0\right)$. The differential production rate becomes

$$d\Gamma = \frac{dV\, n\left({}^7Be\right) n\left(e\right)}{\left(2\pi\right)^2}\int d^3\mathbf{p}_{^7Be} d^3\mathbf{p}_e d^3\mathbf{q} d^3\mathbf{p}_{^7Li} \phi_{^7Be}\phi_e S\left(0\right) C\delta^{(4)}\left(p_f - p_i\right) \tag{1.35}$$

where ϕ_i represents the Boltzmann distribution of the i-th particle. After the integrations over ${}^7Li$ and neutrino momenta (assuming for the latter a spherical simmetry in momenta space), Eq. (1.35) semplifies as

$$d\Gamma = \frac{1}{2\pi} dV\, n\left({}^7Be\right) n\left(e\right) \int d^3\mathbf{p}_{^7Be} d^3\mathbf{p}_e dq \phi_{^7Be} \phi_e S\left(0\right) C q^2 \delta\left(E_f - E_i\right) \tag{1.36}$$

The energy spectrum from continuum orbits capture can be expressed as

$$\text{Spectrum}_{cont}\left(q_{obs}, T\right) = \frac{\frac{d\Gamma}{dq_{obs}}\left(q_{obs}, T\right)}{\int dq_{obs} \frac{d\Gamma}{dq_{obs}}} \tag{1.37}$$

By normalizing the spectrum respect to the neutrino energy, we can omit the constant terms in the integrals. Energy conservation assumes a simpler form in the center-of-momentum reference frame, where we have

$$\Delta M + K = \frac{q^2}{2M_{^7Li}} + q \tag{1.38}$$

where $\Delta M = 862.10$ keV is the difference of total mass of initial particles and mass of ^7Li, $K = p_\mu^2/2\mu$ is the energy of reduced mass μ of the system $\left(e^-, {}^7Be\right)$ and where we have assumed $p_{^7Li} = q$, with q denoting neutrino momentum.
Using the properties of the delta function, we obtain

$$\begin{aligned} \delta\left(E_f - E_i\right) &= \delta\left[\tfrac{q^2}{2M_{^7Li}} + q - \left(\Delta M + K\right)\right] \\ &= \frac{\delta\left[q - M_{^7Li}(-1+\sqrt{1+2\frac{\Delta M+K}{M_{^7Li}}})\right]}{1+\frac{q}{2M_{^7Li}}} \simeq \frac{\delta[q-(\Delta M+K)]}{1+\frac{\Delta M+K}{2M_{^7Li}}} \end{aligned} \tag{1.39}$$

The neutrinos that are observed in the laboratory experience a Doppler shift, because of the motion $\mathbf{V}$ of the center-of-momentum frame relative to the laboratory frame. Let the z axis be oriented along the direction between the terrestrial detector and the core of the Sun.
Then the energy of neutrino observed at laboratory is

$$q_{obs} = q_{cm}\left(p\right)\left(1 - V_{z,cm}\right) \tag{1.40}$$

Using the c.m. coordinate system, and taking into account that neutrino energy in the expression for prodution rate is evaluated in c.m. reference frame, Eq. (1.36) can be expressed in the following form

$$\begin{aligned} d\Gamma\left(q_{cm}, T\right) \propto \int dK dP_z dq_{cm} \exp\left(-\tfrac{K}{T}\right) \exp\left(-\tfrac{P_z^2}{2MT}\right) \cdot \\ \cdot \frac{1}{1-\exp\left(-\frac{8\pi\alpha m_e}{\sqrt{2m_\mu K}}\right)} \frac{q_{cm}^2}{1+\frac{\Delta M+K}{M_{^7Li}}} \delta\left(q_{cm} - \Delta M - K\right) \end{aligned} \tag{1.41}$$

with $M = 6536.73947$ MeV the total mass of $\left(e^-, {}^7Be\right)$ system. We are interested in differential rate respect q_{obs}. In order to change neutrino energy variable, we note that

$$\begin{aligned} dq_{cm}\delta\left(q_{cm} - \Delta M - K\right) = \left(1 + V_{z,cm}\right) dq_{obs}\delta\left[q_{obs}\left(1 + \tfrac{P_z}{M}\right) - \left(\Delta M + K\right)\right] = \\ = dq_{obs}\delta\left[q_{obs} - \left(\Delta M + K\right)\left(1 - \tfrac{P_z}{M}\right)\right] = \tfrac{dq_{obs}}{q_{cm}}\delta\left[\tfrac{P_z}{M} - \tfrac{q_{obs} - \left(\Delta M + K\right)}{\Delta M + K}\right] \end{aligned} \tag{1.42}$$

Finally we obtain

$$\begin{aligned} \tfrac{d\Gamma}{dq_{obs}}\left(q_{obs}, T\right) \propto \int_0^\infty dK \exp\left(-\tfrac{K}{T}\right) \exp\left[-\tfrac{M}{2\Delta M^2 T}\left(\tfrac{q_{obs} - \Delta M - K}{1 + \frac{K}{\Delta M}}\right)^2\right] \cdot \\ \cdot \tfrac{1}{1 - \exp\left(-\frac{8\pi\alpha m_e}{\sqrt{2m_\mu K}}\right)} \tfrac{\Delta M}{1 + \frac{\Delta M}{M_{^7Li}}\left(1 + \frac{K}{\Delta M}\right)} \left(1 + \tfrac{K}{\Delta M}\right) \end{aligned} \tag{1.43}$$

The temperature in the core of the Sun is of $\sim 15 \cdot 10^6$ K, so that the particles have thermal energies of $\sim few$ keV. To evaluate the integral numerically, we put a cut-off $K_{max} = 25$ keV. Expressing energies in keV and temperatures in units of 10^6 K, Eq. (9) can be rewritten in the form

$$\begin{aligned} \tfrac{d\Gamma}{dq_{obs}}\left(q_{obs}, T\right) \propto \int_0^{K_{max}=25} dK \exp\left(-11.60\tfrac{K}{T_6}\right) \exp\left[-\tfrac{51.026}{T_6}\left(\tfrac{q_{obs} - \Delta M - K}{1 + \frac{K}{\Delta M}}\right)^2\right] \cdot \\ \cdot \tfrac{1}{1 - \exp\left(-\frac{2.93}{\sqrt{K}}\right)} \tfrac{\Delta M}{1 + 1.32 \cdot 10^{-4}\left(1 + \frac{K}{\Delta M}\right)} \left(1 + \tfrac{K}{\Delta M}\right) \end{aligned} \tag{1.44}$$

The energy spectrum of ${}^7Be$ neutrino is given by the sum of electron capture from both continuum and bound orbits

$$\text{Spectrum}\left(q_{obs}, T\right) = \frac{\text{Spectrum}_{cont}\left(q_{obs}, T\right) + f_{bound}\left(T\right)\text{Spectrum}_{bound}\left(q_{obs}, T\right)}{1 + f_{bound}\left(T\right)} \tag{1.45}$$

where the normalized energy profile resulting from bound capture has the simple form

$$\text{Spectrum}_{bound}\left(q_{obs}, T\right) = q_{bound,star}^{-1}\left(\frac{M_{^7Be}}{2\pi T}\right)^{1/2} \exp\left[-\frac{M_{^7Be}}{2T}\left(\frac{q_{obs} - q_{bound,star}}{q_{bound,star}}\right)^2\right] \tag{1.46}$$

and the expression for $f_{bound}\left(T\right)$ is given by the expression

$$f_{bound}\left(T\right)=\frac{5.07}{T_6}S_R\exp\left(2.515\frac{\sigma_R}{T_6}\right) \tag{1.47}$$

where [36]

$$\sigma_R\cong-0.431+2.091r-1.481r^2+0.401r^3 \tag{1.48}$$

with $r=0.298\left[64T_6/\rho\left(3+X\right)\right]^{1/2}$ the Debye-Huckel screening length divided by the Bohr radius, ρ and X being, respectively, the local density (gcm^{-3}) and the hydrogen mass fraction. The expression for S_R is [37]

$$S_R=C_R^2D^{-1}\left[1+0.435L_R\exp\left(-0.735\sigma_R/T_6\right)\right] \tag{1.49}$$

with

$$D=\left[1+L_R+0.25L_R^2\exp\left(-0.735\sigma_R/T_6\right)\right] \tag{1.50}$$

$$L_R=0.246\left(\rho\mu_e^{-1}T_6^{-3/2}\right)\exp\left(2.515\sigma_R/T_6\right) \tag{1.51}$$

$$D=\left[1+L_R+0.25L_R^2\exp\left(-0.735\sigma_R/T_6\right)\right] \tag{1.52}$$

in Eq. (1.49) [36]

$$C_R^2\cong-0.6064+4.859r-5.283r^2+1.907r^3 \tag{1.53}$$

and in Eq. (1.51) $\mu_e\approx2/\left(1+X\right)$ is the electron mean molecular weight.
The neutrino spectrum for the entire Sun is obtained as weighted average of Spectrum (T,q_{obs}) respect to the flux of ^7Be neutrinos as a function of the temperature

$$\mathrm{Spectrum}_{sun}\left(q_{obs}\right)=\frac{\int d\phi_{^7Be}\left(T\right)\mathrm{Spectrum}\left(q_{obs},T\right)}{\int d\phi_{^7Be}\left(T\right)} \tag{1.54}$$

The importance to detect experimentally the red-shift experienced by ^7Be neutrinos besides in the possibility to estimate the temperature in the core of the Sun (averaged through the ^7Be neutrino flux), by means of the first order moment of neutrino energy spectrum. It is easy to demonstrate, in fact, that the first order moment is proportional to the temperature in the Sun, that is

$$\left\langle q_{obs}-q_{cont,\,sun}\right\rangle=\int_0^\infty dq_{obs}\left(q_{obs}-q_{cont,\,sun}\right)\ \mathrm{Spectrum}\left(q_{obs},\,T\right)\simeq T \tag{1.55}$$

In the next section it will be presented the results of the calculations that we have made on the neutrino red-shift for *pep* neutrino and how to relate the first order moment of neutrino energy with the temperature in the Sun.

1.4.2 *pep* Neutrino Energy Spectrum

The rate for the reaction $p+e^{-}+p \rightarrow D+\nu_e$ is calculated considering the electron capture from the *pp* system, so that it can be expressed in terms of the *pp* reaction as follows [36]

$$R_{pep} = \frac{K_{pp}}{\bar{f}_{pp}} R_{pp} \tag{1.56}$$

where R_{pp} is the rate of the *pp* reaction, $\bar{f}_{pp} = f(E_0)$ is the *pp* phase-space integral as function of the most probable center-of-mass energy ($E_0 \approx 3.9\, T_6$ keV) for the collisions that lead to *pp* reaction, and

$$K_{pp} \propto \int_0^{\infty} dK_e \exp(-K_e/T) \left[1 - \exp\left(-1.4657 K_e^{-1/2}\right)\right]^{-1}$$

is the generalized phase-space factor appropriate for electron capture [38]. Here K_e denotes the electron kinetic energy expressed in keV.
Taking into account this approximation, the spectrum of *pep* solar neutrino energy can be expressed in the following form

$$\begin{gathered} \Gamma(q_{obs}, T) \propto \int d^3p_e d^3p_1 d^3p_2 d^3p_D d^3p_\nu \phi_e \phi_1 \phi_2 \\ \cdot C(-2, v_e)\, C(1, v_{12})\, \delta^{(4)}(P_f - P_i) \end{gathered} \tag{1.57}$$

where $\phi_a = \exp\left[-p_a^2/(2M_aT)\right]$ is the Boltzmann distribution for the particle a, $C(Z_1Z_2, v_a)$ is the Coulomb factor

$$C(Z_1Z_2, v_a) = \frac{2\pi\alpha Z_1 Z_2 / v_a}{1 - \exp(-2\pi\alpha Z_1 Z_2 / v_a)} \tag{1.58}$$

with v_a the velocity of the particle and Z_1Z_2 the effective charge. In particular v_e is the velocity of the electron and v_{12} is the relative velocity of the two protons. Following the same procedure used for ^7Be neutrino energy spectrum, we obtain from Eq. (1.57)

$$\begin{gathered} \Gamma(q_{obs}, T) \propto \int d^3p_e d^3p_1 d^3p_2 d^3p_\nu \phi_e \phi_1 \phi_2 \\ \cdot C(-2, v_e)\, C(1, v_{12})\, \delta(E_f - E_i) \end{gathered} \tag{1.59}$$

and, by using the properties of delta function and changing *pp* momenta variables in that of the c.m. reference frame, we obtain

$$\Gamma\left(q_{cm},T\right)\propto-\int dK_e dK_{12} dP_z dq_{cm}\exp\left(-\frac{K}{T}\right)\exp\left(-\frac{P_z^2}{4M_pT}\right)$$
$$\cdot\frac{1}{1-\exp\left(-4\pi\alpha\sqrt{\frac{m_e}{2K_e}}\right)}\frac{1}{\exp\left(2\pi\alpha\sqrt{\frac{M_p}{4K_{12}}}\right)-1}\frac{q_{cm}^2}{1+\frac{\Delta M+K}{M_D}}\delta\left(q_{cm}-\Delta M-K\right) \tag{1.60}$$

where P_z is the component of c.m. momentum respect z-axis choosen along the direction between the terrestrial detector and the core of the Sun. Deriving Γ respect to q_{obs} variable and integrating over P_z, we obtain

$$\frac{d\Gamma}{dq_{obs}}\left(q_{obs},T\right)\propto\int_0^\infty dK_e\int_0^\infty dK_{12}\exp\left(-\frac{K}{T}\right)\exp\left[-\frac{M_p}{\Delta M^2T}\left(\frac{q_{obs}-\Delta M-K}{1+\frac{K}{\Delta M}}\right)^2\right]$$
$$\cdot\frac{1}{1-\exp\left(-4\pi\alpha\sqrt{\frac{m_e}{2K_e}}\right)}\frac{1}{\exp\left(2\pi\alpha\sqrt{\frac{M_p}{4K_{12}}}\right)-1}\frac{\Delta M}{1+\frac{\Delta M}{M_D}\left(1+\frac{K}{\Delta M}\right)}\left(1+\frac{K}{\Delta M}\right) \tag{1.61}$$

or, expliciting the numerical values of the constant in the integral

$$\frac{d\Gamma}{dq_{obs}}\left(q_{obs},T\right)\propto\int_0^{K_{max}=25}\int_0^{K_{max}=25}dK_e dK_{12}\exp\left(-11.60\frac{K}{T_6}\right)$$
$$\exp\left[-\frac{5.234}{T_6}\left(\frac{q_{obs}-\Delta M-K}{1+\frac{K}{\Delta M}}\right)^2\right]\frac{1}{1-\exp\left(-1.466K_e^{-1/2}\right)}\frac{1}{\exp\left(22.2K_{12}^{-1/2}\right)-1}\frac{\Delta M\left(1+\frac{K}{\Delta M}\right)}{1+7.686\cdot10^{-4}\left(1+\frac{K}{\Delta M}\right)} \tag{1.62}$$

where kinetic energy are expressed in keV and temperature in units of 10^6 K. For the numerical integration, we have assumed a cut-off in particles energy $K_{max}=25$ keV.
We give the results of evaluated spectrum as a function of $q_{obs}-q_0$, with $q_0=1442$ keV. The values of solar parameters are taken from interpolation of BS05(AGS,OP) Solar Standard Model [6] on a grid of 128 points from minimum to maximum value of solar radius parameter of SSM. All the integrals are evaluated using trapezoidal rule. Each integral on particle energy in Eq. (1.62) is integrated on a grid of 128 points, while q_{obs} grid is made of 128 points from $q_{min}=-1.0$ to $q_{max}=24.4$. The profiles of *pep* neutrino spectrum at different solar radius are shown in Fig. 1.4.
In Fig. 1.5 is shown the global spectrum weighted respect the fraction of *pep* solar neutrino flux is compared with the energy spectrum of ^7Be neutrino. The peak of the spectrum is located at $q_{obs}-q_0=6.6$ keV. The properties of the spectrum are summarized in Tab. 1.3.

1.4.3 First Order Moment of *pep* Solar Neutrino

The 1st moment of the solar energy spectrum is defined by the relation

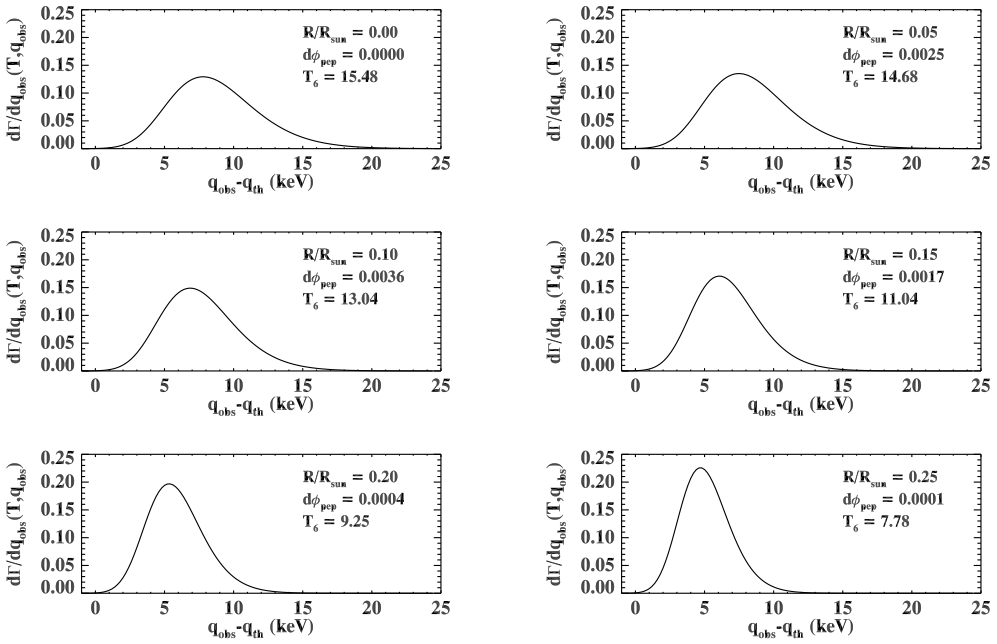

FIGURE 1.4: The energy profile for the 1.442 MeV *pep* solar neutrino line for six values of R/R_{sun} from 0.0 to 0.25. For each value of solar radius, the fraction of *pep* neutrino flux and temperature of solar interior (in units of 10^6K) are reported as predicted by BS05(AGS, OP) Solar Standard Model [6].

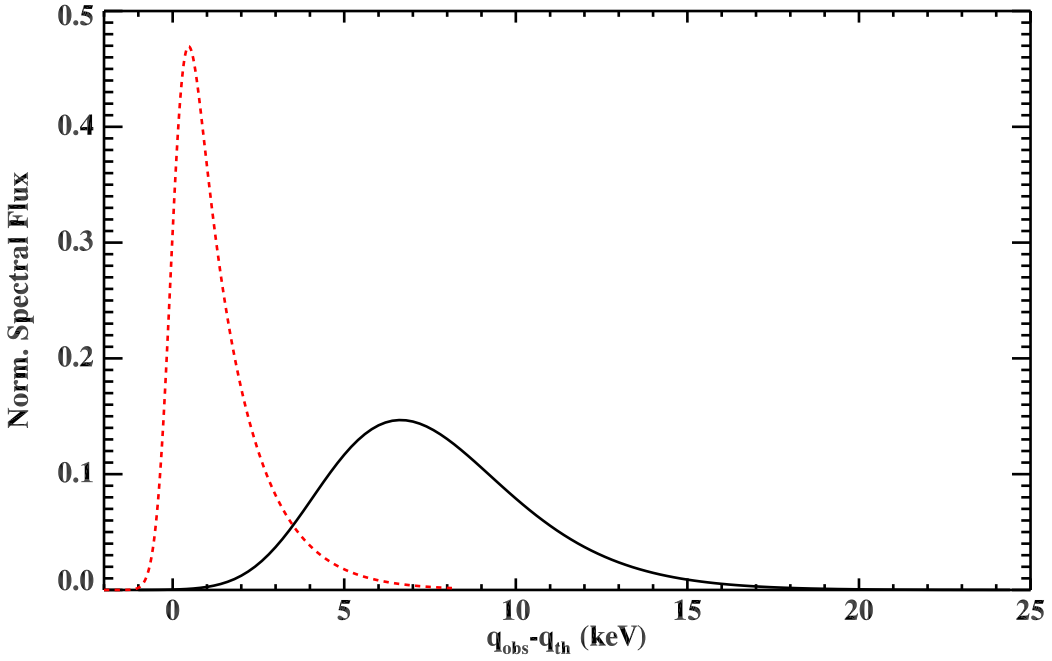

FIGURE 1.5: Solar neutrino spectrum for *pep* neutrino (black solid line) and for ^7Be neutrino (red dashed line).

TABLE 1.3: Characteristics of ^7Be and *pep* neutrino energy spectrum. For ^7Be neutrino spectrum are reported as a reference the results obtained by Bahcall [35]. The neutrino energy spectra have been evaluated using input values from BS05(AGS,OP) SSM [6], except for (Bahcall, 1994) ^7Be neutrino spectrum. For each model are shown the number of points used for numerical integration (i.e. for solar radius variable R, x variable defined as $x = q - q_{obs}$ and kinetic energy K), resolution in energy dx, energy value as observed in laboratory q_{obs}, difference between peak of the spectrum q_{peak} and q_{obs}, shift in average neutrino energy Δ, FWHM, half width on the low-energy side of the peak W^- and half width on the high-energy side W^+. For *pep* spectrum the array of integration points include both electron and reduced mass of *pp* sytem kinetic energies, i.e.$(N_R, N_x, N_{K_e}, N_{K_{12}})$. All the variables with energy dimension are expressed in keV.

	^7Be (Bahcall, 1994)	^7Be	*pep*
(N_R, N_x, N_K)	-	$(256, 512, 512)$	$(128, 128, 128, 128)$
dx	0.1	0.02	0.2
q_{lab}	861.84	861.84	1442
$q_{peak} - q_{lab}$	0.43	0.46	6.6
Δ	1.29	1.30	7.59
FWHM	1.63	1.72	6.29
W^-	0.56	0.59	2.71
W^+	1.07	1.13	3.58

$$\Delta \equiv \langle (q_{obs} - q_0) \rangle = \int_0^\infty dq_{obs}\,(q_{obs} - q_0)\,S\,(q_{obs}) \tag{1.63}$$

where q_0 and q_{obs} are the expected and the observed neutrino energy, respectively, and $S\,(q_{obs})$ is the neutrino energy spectrum which can be expressed in the form

$$S\,(q_{obs}) = \int d\phi_{pep} \frac{\frac{d\Gamma}{dq_{obs}}}{\int_0^\infty dq_{obs} \frac{d\Gamma}{dq_{obs}}} \tag{1.64}$$

where $d\Gamma/dq_{obs}$ is the differential rate of *pep* reaction and *pep* neutrino flux is normalized, so that $\int d\phi_{pep} = 1$. By inverting the order of integration, Eq. (1.63) can be rewritten as

$$\Delta = \int d\phi_{pep} \frac{\int_0^\infty dq_{obs}\,(q_{obs} - q_0)\,\frac{d\Gamma}{dq_{obs}}}{\int_0^\infty dq_{obs} \frac{d\Gamma}{dq_{obs}}} \tag{1.65}$$

The *pep* reaction can be described as an electron capture process from the proton-proton system and the differential rate is due to the rate of *pp* reaction times the electron capture probability [38, 36]. By changing proton-proton momenta variables in center-of-momentum coordinates and taking into account the Doppler shift experienced by neutrinos, due to the motion of center-of-momentum frame relative to the laboratory frame, the differential rate (differentiated respect neutrino energy) can be finally expressed through the relation

$$\frac{d\Gamma}{dq_{obs}}(q_{obs},T) \propto \int_0^\infty dK_e \int_0^\infty dK_{12} \exp\left(-\frac{K}{T}\right) \exp\left[-\frac{M_p}{\Delta M^2 T}\left(\frac{q_{obs}-\Delta M-K}{1+\frac{K}{\Delta M}}\right)^2\right] \cdot$$
$$\cdot \frac{1}{1-\exp\left(-4\pi\alpha\sqrt{\frac{m_e}{2K_e}}\right)} \frac{1}{\exp\left(2\pi\alpha\sqrt{\frac{M_p}{4K_{12}}}\right)-1} \frac{\Delta M\left(1+\frac{K}{\Delta M}\right)}{1+\frac{\Delta M}{M_D}\left(1+\frac{K}{\Delta M}\right)} \tag{1.66}$$

where the first exponential represents the Boltzmann distribution of initial particles energy ($K \equiv K_e + K_{12}$), the second exponential is the Boltzmann distribution for center-of-momentum energy, where the momentum has been replaced using the Doppler shift expression $q_{obs} = q_{cm}(1 - V_{z,cm})$. The last three terms represent, respectively, the Coulomb factors for the initial state of proton-proton interaction and for the interaction of electron with proton-proton system, and the correction factor due to the delta function expressing the energy conservation. The matrix elements that are constant have been dropped since they cancel out in Eq. (1.65). Terms of the order of $K/\Delta M \approx 10^{-3}$ can be omitted, and the Eq. (1.66) becomes

$$\frac{d\Gamma}{dq_{obs}}(q_{obs},T) \sim \int_0^\infty dK_e dK_{12} \frac{\exp\left(-\frac{K_e}{T}\right)}{1-\exp\left(-4\pi\alpha\sqrt{\frac{m_e}{2K_e}}\right)} \cdot$$
$$\cdot \exp\left(-\frac{K_{12}}{T}\right) \exp\left(-2\pi\alpha\sqrt{\frac{M_p}{4K_{12}}}\right) \exp\left[-\frac{M_p}{q_0^2 T}(q_{obs}-q_0-K)^2\right] \tag{1.67}$$

From Eq. (1.65), by changing the order of integration, we have the integrals respect the neutrino energy

$$\int_0^\infty dq_{obs} \exp\left[-\frac{M_p}{T q_0^2}(q_{obs}-q_0-K)^2\right] \underset{z \equiv \frac{q_{obs}-q_0-K}{q_0\sqrt{\frac{T}{2M_p}}}}{=} q_0\sqrt{\frac{\pi T}{M_p}} \tag{1.68}$$

and

$$\int_0^\infty dq_{obs}(q_{obs}-q_0) \exp\left[-\frac{M_p}{T q_0^2}(q_{obs}-q_0-K)^2\right] =$$
$$= q_0\sqrt{\frac{T}{2M_p}} \int_{-\infty}^{+\infty} dz \left(q_0\sqrt{\frac{T}{2M_p}}z + K\right) \exp\left(-\frac{z^2}{2}\right) = q_0\sqrt{\frac{\pi T}{M_p}}K \tag{1.69}$$

The normalization factor in Eq. (1.65) becomes

$$\int_0^\infty dq_{obs} \frac{d\Gamma}{dq_{obs}} = q_0\sqrt{\frac{\pi T}{M_p}} \int_0^\infty dK_e dK_{12} \frac{\exp\left(-\frac{K_e}{T}\right)}{1-\exp\left(-4\pi\alpha\sqrt{\frac{m_e}{2K_e}}\right)} \cdot$$
$$\cdot \exp\left(-\frac{K_{12}}{T}\right) \exp\left(-2\pi\alpha\sqrt{\frac{M_p}{4K_{12}}}\right) \tag{1.70}$$

while for the integral at numerator of Eq. (1.65) we obtain the following expression

$$\int_0^\infty dq_{obs}\,(q_{obs}-q_0)\,\frac{d\Gamma}{dq_{obs}} = q_0\sqrt{\frac{\pi T}{M_p}}\int_0^\infty dK_e dK_{12}\frac{\exp\left(-\frac{K_e}{T}\right)}{1-\exp\left(-4\pi\alpha\sqrt{\frac{m_e}{2K_e}}\right)}\cdot$$
$$\cdot\exp\left(-\frac{K_{12}}{T}\right)\exp\left(-2\pi\alpha\sqrt{\frac{M_p}{4K_{12}}}\right)K \tag{1.71}$$

Defining the new variables $(x,\,y)$ as

$$\begin{cases} x \equiv \frac{K_e}{T} \\ y \equiv \frac{K_{12}}{T} \end{cases} \tag{1.72}$$

We obtain

$$(1.70) \to q_0\sqrt{\frac{\pi T}{M_p}}T^2\int_0^\infty dxdy\frac{e^{-x}}{1-e^{-4\pi\alpha\sqrt{\frac{m_e}{2T}}\frac{1}{\sqrt{x}}}}e^{-y}e^{-\frac{\epsilon}{\sqrt{y}}}$$

$$(1.71) \to q_0\sqrt{\frac{\pi T}{M_p}}T^3\int_0^\infty dxdy\frac{e^{-x}}{1-e^{-4\pi\alpha\sqrt{\frac{m_e}{2T}}\frac{1}{\sqrt{x}}}}e^{-y}e^{-\frac{\epsilon}{\sqrt{y}}}(x+y)$$

where

$$\epsilon \equiv 2\pi\alpha\sqrt{\frac{M_p}{4T}} \simeq \frac{75.63}{\sqrt{T_6}} \gg 1 \tag{1.73}$$

Finally, defining the moments of the particle energies through the expressions

$$\begin{cases} I^e_\mu \equiv \int_0^\infty dx x^\mu \frac{e^{-x}}{1-e^{-4\pi\alpha\sqrt{\frac{m_e}{2T}}\frac{1}{\sqrt{x}}}} = \int_0^\infty dx x^\mu \frac{e^{-x}}{1-e^{-\frac{5}{\sqrt{T_6}}\frac{1}{\sqrt{x}}}} \\ \\ I^p_\nu \equiv \int_0^\infty dy y^\nu e^{-y}e^{-\frac{\epsilon}{\sqrt{y}}} \end{cases} \tag{1.74}$$

we obtain for Δ the equation

$$\Delta = \int d\phi_{pep}\frac{\int_0^\infty dq_{obs}(q_{obs}-q_0)\frac{d\Gamma}{dq_{obs}}}{\int_0^\infty dq_{obs}\frac{d\Gamma}{dq_{obs}}} = \int d\phi_{pep}\left(T\frac{I^e_1 I^p_0 + I^e_0 I^p_1}{I^e_0 I^p_0}\right) =$$
$$= \langle r_e T\rangle_{pep} + \langle r_p T\rangle_{pep} \tag{1.75}$$

where $r_a \equiv I^a_1/I^a_0$.

1.4.4 Discussion on Electron Moments Approximation

In Tab. 1.4 are reported the values of the 0th and 1st electron moments and their ratio r_e for 6 values of T_6 from 10 to 16.

TABLE 1.4: Numerical values of 0th and 1st electron moments and r_e for different values of T_6.

T_6	$I_0^e(T_6)$	$I_1^e(T_6)$	$r_e(T_6)$
10	1.23388	1.451	1.17596
11	1.25529	1.48737	1.18489
12	1.2761	1.52247	1.19307
13	1.29636	1.55641	1.2006
14	1.31612	1.5893	1.20757
15	1.3354	1.62124	1.21405
16	1.35424	1.6523	1.2201

Even if the ratio growths as the temperature increases, we can assume that in the range of temperatures of interest r_e increases slowly, so that as a first approximation r_e can be considered constant. For the inner regions of the Sun, T_6 has values of the order of 10. In Tab. 1.5 we report the relative variation of r_e respect its value at $T_6 = 10$.

TABLE 1.5: Relative variation of $r_e(T_6)$ respect to $r_e(10)$.

T_6	$\delta_e(10) \equiv \left\lvert \frac{r_e(T_6)-r_e(10)}{r_e(T_6)} \right\rvert$ %
11	0.753174
12	1.43344
13	2.05191
14	2.61743
15	3.13718
16	3.61704

We observe that the variation lies in the range of $\sim$ $few\%$. We can obtain a better approximation taking the value of T_6 for which r_e is equal to the mean value evaluated in the range of temperatures from 10 to 16. In particular we have[5]

$$\overline{r_e} = 1.19946 \rightarrow T_6^* = 12.8439$$

In Tab. 1.6 are shown the relative variation of r_e respect $\overline{r_e}$ in the range of temperature of interest. We can observe that now the variations are of the order of 1%.

[5]In the next subsection we will find a value for the temperature of the Sun averaged over the *pep* neutrino flux which value is close to that find here. In any case one has to be carefull to not consider $T_6^\star$ as the effective averaged temperature, since $T_6^\star$ is only used as a reference temperature to evaluate numerically $\bar{r_e}$, which value can be, on the other hand evaluated also from an arithmetical average over a set of r_e values obtained for different temperatures. Furthermore we will see that the averaged temperature is model dependent, i.e. its value depends on the SSM considered, while the value of $\bar{r_e}$is model indipenent.

TABLE 1.6: Relative variation of $r_e(T_6)$ respect to $\overline{r_e}$.

T_6	$\delta_e\left(\overline{T_6}\right) \equiv \left\lvert \frac{r_e(T_6)-\overline{r_e}}{r_e(T_6)} \right\rvert$ %
10	1.9982
11	1.22998
12	0.536116
13	0.0947076
14	0.671529
15	1.20167
16	1.69111

Using $\overline{r_e}$ as an estimation of electron moment ratio, Eq. (1.75) can be rewritten as

$$\langle (q_{obs} - q_0) \rangle = \overline{r_e} \langle T \rangle_{pep} + \langle r_p T \rangle_{pep} \tag{1.76}$$

1.4.5 Analytical Estimation of Proton Moments

The integration of the 0th and 1st proton moments can be performed using the method of "steepest descents", according to which, an integral of the form

$$I(z) = \int_a^b e^{-Mf(x)} dz$$

can be approximated thorugh the expression

$$I(z) = \int_a^b e^{-Mf(x)} dz \underset{M\to\infty}{\approx} \sqrt{\frac{2\pi}{|Mf''(z_0)|}} e^{Mf(z_0)} \tag{1.77}$$

assuming that $f(z)$ has a global maximum at z_0.
For the 0th proton moment we obtain

$$I_0^p \simeq \sqrt{\frac{4\pi}{3}} \left(\frac{\epsilon}{2}\right)^{\frac{1}{3}} e^{-3\left(\frac{\epsilon}{2}\right)^{\frac{2}{3}}} \tag{1.78}$$

For the higher order proton moments we have to solve the following equation

$$I_\nu^p = \int_0^\infty dy y^\nu e^{-y} e^{-\frac{\epsilon}{\sqrt{y}}} = \int_0^\infty dy e^{-g(y)} \simeq \sqrt{\frac{2\pi}{|g''(y_*)|}} e^{-g(y_*)} \tag{1.79}$$

where

$$\begin{cases} g(y) = y + 2\frac{\epsilon}{2} y^{-\frac{1}{2}} - \nu \ln y \\ g'(y) = 1 - \frac{\epsilon}{2} y^{-\frac{3}{2}} - \nu y^{-1} \\ g''(y) = \frac{3}{2}\frac{\epsilon}{2} y^{-\frac{5}{2}} + \nu y^{-2} \end{cases}$$

In order to apply the method we have to find the roots of $g'(y_*) = 0$, i.e.

$$1 - \frac{\epsilon}{2} y_*^{-\frac{3}{2}} - \nu y_*^{-1} = 0 \tag{1.80}$$

or, equivalently

$$\frac{y - \frac{\epsilon}{2} y^{-\frac{1}{2}} - \nu}{y} = 0 \rightarrow \left(\frac{y}{\nu}\right)^{\frac{1}{2}} \left(\frac{y}{\nu} - 1\right) = \frac{\epsilon}{2} \nu^{-\frac{3}{2}}$$

By defining θ through the expression

$$\left(\frac{y}{\nu}\right)^{\frac{1}{2}} = \frac{2}{\sqrt{3}} \cosh(\theta) \tag{1.81}$$

the root of eq. (1.80) can be written as

$$y_* = \tfrac{4}{3}\nu \cosh^2(\theta_*) \qquad \theta_* = \tfrac{1}{3} \operatorname{arccos\,h}\left(\tfrac{\sqrt{27}}{2} \tfrac{\epsilon}{2} \nu^{-\frac{3}{2}}\right) \tag{1.82}$$

we can expand the $\operatorname{arccosh}\left(\frac{\sqrt{27}}{2}\frac{\epsilon}{2}\nu^{-\frac{3}{2}}\right)$ function respect the variable $(\epsilon/2)^{-1}$ obtaining

$$\operatorname{arccos\,h}\left(\tfrac{\sqrt{27}}{2} \tfrac{\epsilon}{2} \nu^{-\frac{3}{2}}\right) = \ln\left[\tfrac{\sqrt{27}}{2} \tfrac{\epsilon}{2} \nu^{-\frac{3}{2}} \left(1 + \sqrt{1 - \tfrac{4}{27}\nu^3 \left(\tfrac{\epsilon}{2}\right)^{-2}}\right)\right] \simeq$$

$$\simeq \ln\left(\sqrt{27} \tfrac{\epsilon}{2} \nu^{-\frac{3}{2}}\right) - \tfrac{1}{27}\nu^3 \left(\tfrac{\epsilon}{2}\right)^{-2}$$

and y_* can be approximated through the expression

$$\begin{aligned} y_* &= \tfrac{4}{3}\nu \cosh^2\left[\ln\left(\sqrt{\tfrac{3}{\nu}} \left(\tfrac{\epsilon}{2}\right)^{\frac{1}{3}}\right) - \tfrac{1}{81}\nu^3 \left(\tfrac{\epsilon}{2}\right)^{-2}\right] = \\ &= \left(\tfrac{\epsilon}{2}\right)^{\frac{2}{3}} \left[1 - \tfrac{2}{81}\nu^3 \left(\tfrac{\epsilon}{2}\right)^{-2}\right] \left[1 + \tfrac{\nu}{3} \left(\tfrac{\epsilon}{2}\right)^{-\frac{2}{3}}\right]^2 + O\left[\left(\tfrac{\epsilon}{2}\right)^{-2}\right] \end{aligned} \tag{1.83}$$

Using this approximation to estimate $g(y_*)$ and $g'(y_*)$ we obtain

$$\begin{cases} g(y_*) = y_* + 2\frac{\epsilon}{2} y_*^{-\frac{1}{2}} - \nu \ln y_* = 3\left(\frac{\epsilon}{2}\right)^{\frac{2}{3}} - \frac{1}{3}\nu^2 \left(\frac{\epsilon}{2}\right)^{-\frac{2}{3}} + \frac{1}{27}\nu^3 \left(\frac{\epsilon}{2}\right)^{-\frac{4}{3}} - \nu \ln\left(\frac{\epsilon}{2}\right)^{\frac{2}{3}} + O\left[\left(\frac{\epsilon}{2}\right)^{-2}\right] \\ g''(y_*) = \frac{3}{2}\frac{\epsilon}{2} y^{-\frac{5}{2}} + \nu y^{-2} = \frac{3}{2}\left(\frac{\epsilon}{2}\right)^{-\frac{2}{3}} \left[1 - \nu\left(\frac{\epsilon}{2}\right)^{-\frac{2}{3}}\right] + O\left[\left(\frac{\epsilon}{2}\right)^{-2}\right] \end{cases}$$

and the approximated expression for the proton moment assumes the form

$$\begin{aligned} I_\nu^p &\simeq \sqrt{\tfrac{4\pi}{3}} \left(\tfrac{\epsilon}{2}\right)^{\frac{1}{3}} \left[1 - \nu\left(\tfrac{\epsilon}{2}\right)^{-\frac{2}{3}}\right]^{-\frac{1}{2}} \left(\tfrac{\epsilon}{2}\right)^{\frac{2}{3}\nu} e^{-3\left(\frac{\epsilon}{2}\right)^{\frac{2}{3}}} e^{+\frac{1}{3}\nu^2\left(\frac{\epsilon}{2}\right)^{-\frac{2}{3}} - \frac{1}{27}\nu^3\left(\frac{\epsilon}{2}\right)^{-\frac{4}{3}}} = \\ &= I_0^p \left(\tfrac{\epsilon}{2}\right)^{\frac{2}{3}\nu} \left[1 - \nu\left(\tfrac{\epsilon}{2}\right)^{-\frac{2}{3}}\right]^{-\frac{1}{2}} e^{+\frac{1}{3}\nu^2\left(\frac{\epsilon}{2}\right)^{-\frac{2}{3}} - \frac{1}{27}\nu^3\left(\frac{\epsilon}{2}\right)^{-\frac{4}{3}}} \end{aligned} \tag{1.84}$$

Finally we obtain for r_p

$$r_p \equiv \frac{I_1^p}{I_0^p} = \left(\tfrac{\epsilon}{2}\right)^{\frac{2}{3}} \left[1 - \left(\tfrac{\epsilon}{2}\right)^{-\frac{2}{3}}\right]^{-\frac{1}{2}} e^{+\frac{1}{3}\left(\frac{\epsilon}{2}\right)^{-\frac{2}{3}} - \frac{1}{27}\left(\frac{\epsilon}{2}\right)^{-\frac{4}{3}}} \simeq$$
$$\simeq \left(\tfrac{\epsilon}{2}\right)^{\frac{2}{3}} + \tfrac{5}{6} + \tfrac{121}{216}\left(\tfrac{\epsilon}{2}\right)^{-\frac{2}{3}} + \tfrac{571}{1296}\left(\tfrac{\epsilon}{2}\right)^{-\frac{4}{3}} + O\left[\left(\tfrac{\epsilon}{2}\right)^{-2}\right] \tag{1.85}$$

The term of the order $(\epsilon/2)^{-4/3}$ can be neglected, in fact

$$\frac{\epsilon}{2} = \pi\alpha\sqrt{\frac{M_p}{4T}} \simeq \frac{37.82}{\sqrt{10}} = 11.96 \rightarrow \frac{571}{1296}\left(\frac{\epsilon}{2}\right)^{-\frac{4}{3}} \simeq 0.016 \tag{1.86}$$

The expression for the 1st moment of neutrino energy becomes

$$\langle (q_{obs} - q_0) \rangle = \overline{r_e}\, \langle T \rangle_{pep} + \tfrac{5}{6}\, \langle T \rangle_{pep} +$$
$$+ \left(\pi\alpha\sqrt{\tfrac{M_p}{4}}\right)^{\frac{2}{3}} \left\langle T^{\frac{2}{3}} \right\rangle_{pep} + \tfrac{121}{216}\left(\pi\alpha\sqrt{\tfrac{M_p}{4}}\right)^{-\frac{2}{3}} \left\langle T^{\frac{4}{3}} \right\rangle_{pep} \tag{1.87}$$

or equivalently

$$\langle (q_{obs} - q_0)_{keV} \rangle = 0.175\, \langle T_6 \rangle_{pep} + 0.971 \left\langle T_6^{\frac{2}{3}} \right\rangle_{pep} + 4.29 \cdot 10^{-3} \left\langle T_6^{\frac{4}{3}} \right\rangle_{pep} \tag{1.88}$$

From eq. (1.88) we observe that the contribution of the last term to the evaluation of Δ, assuming $T_6 \sim 10$ and $\langle T_6^{\mu} \rangle \sim \langle T_6 \rangle^{\mu}$, is of $\sim 1\%$ so that we can neglect the last factor and eq. (1.88) can be finally written as

$$\langle (q_{obs} - q_0)_{keV} \rangle = 0.175\, \langle T_6 \rangle_{pep} + 0.971 \left\langle T_6^{\frac{2}{3}} \right\rangle_{pep} \tag{1.89}$$

1.4.6 Discussions

In order to explicit the dependence of the internal temperature of the Sun from Δ we assume that

$$\left\langle T_6^{\frac{2}{3}} \right\rangle_{pep} \approx \langle T_6 \rangle_{pep}^{\frac{2}{3}} \tag{1.90}$$

We have tested this assumption for two Standard Solar Model, i.e. BS2005(AGS,OP) and BP2000 [39].
For the first model we find

$$\begin{cases} \left\langle T_6^{\frac{2}{3}} \right\rangle_{BS2005(AGS,OP)} = 5.481 \\ \langle T_6 \rangle^{\frac{2}{3}}_{BS2005(AGS,OP)} = 5.491 \\ \delta_{BS2005(AGS,OP)} \equiv \dfrac{\left\langle T_6^{\frac{2}{3}} \right\rangle_{BS2005(AGS,OP)} - \langle T_6 \rangle^{\frac{2}{3}}_{BS2005(AGS,OP)}}{\left\langle T_6^{\frac{2}{3}} \right\rangle_{BS2005(AGS,OP)}} = 0.186\% \end{cases}$$

while for BP2000 model we obtain

$$\begin{cases} \left\langle T_6^{\frac{2}{3}} \right\rangle_{BP2000} = 5.374 \\ \langle T_6 \rangle^{\frac{2}{3}}_{BP2000} = 5.388 \\ \delta_{BP2000} \equiv \left| \dfrac{\left\langle T_6^{\frac{2}{3}} \right\rangle_{BP2000} - \langle T_6 \rangle^{\frac{2}{3}}_{BP2000}}{\left\langle T_6^{\frac{2}{3}} \right\rangle_{BP2000}} \right| = 0.264\% \end{cases}$$

From the SSMs used we observe that the approximation is good within an accuracy of $\sim few \cdot 10^{-1}$ %. Using the approximation expressed in (1.90) we obtain an algebraic equation of the form

$$a \langle T_6 \rangle_{pep} + b \langle T_6 \rangle^{\frac{2}{3}}_{pep} = \Delta \tag{1.91}$$

where $a = 0.175$, $b = 0.971$ and $\Delta = \langle (q_{obs} - q_0)_{keV} \rangle$. By introducing the variable $z \equiv \langle T_6 \rangle^{1/3}$, Eq. (1.91) can be written

$$az^3 + bz^2 = \Delta$$

The solution of this equation can be expressed in the form

$$z = \frac{b}{3a} \left[2 \cosh \left(\frac{1}{3} \operatorname{arccos\,h} (\alpha) \right) - 1 \right] \qquad \alpha \equiv \frac{27a^3}{b^3} \frac{\Delta}{2a} - 1 \tag{1.92}$$

And for $\langle T_6 \rangle_{pep}$ we obtain

$$\langle T_6 \rangle_{pep} = \frac{b^3}{27a^3} \left[2 \cosh \left(\frac{1}{3} \operatorname{arccos\,h} \left(\frac{27a^3}{b^3} \frac{\Delta}{2a} - 1 \right) \right) - 1 \right]^3 \tag{1.93}$$

We can make an estimation of the error for $\langle T_6 \rangle_{pep}$ knowing the accuracy at which can be measured Δ. In particular we have

$$\frac{d \langle T_6 \rangle_{pep}}{\langle T_6 \rangle_{pep}} = \frac{2}{3} \frac{b}{a} \frac{\sinh \left[\frac{1}{3} \operatorname{arccos\,h} \left(\frac{27a^3}{b^3} \frac{\Delta}{2a} - 1 \right) \right]}{\sqrt{1 - \frac{b^3}{27a^3} \frac{4a}{\Delta}}} \langle T_6 \rangle^{-\frac{1}{3}}_{pep} \frac{d\Delta}{\Delta} \tag{1.94}$$

Using the value of Δ evaluated solving numerically Eqs. (1.65) and (1.66) for BS2005(AGS, OP) SSM we obtain

$$\Delta_{BS2005(AGS,OP)} = 7.59 \rightarrow \langle T_6 \rangle_{pep} = 12.88 \left(1 \pm 1.31 \frac{d\Delta}{\Delta}\right) \tag{1.95}$$

The value obtained for $\langle T_6 \rangle_{pep}$ using Eq. (1.93) is in good agreement with that obtained averaging the internal temperature of the Sun over *pep* neutrino flux, i.e. $\langle T_6 \rangle_{pep,\ BS05(AGS,OP)} = 12.87$.

Finally we have tested the results using BP2000 SSM, obtaining

$$\Delta_{BP2000} = 7.42 \rightarrow \langle T_6 \rangle_{pep} = 12.51 \tag{1.96}$$

which is in agreement with the mean value obtained averaging the temperature over the *pep* neutrino flux estimated from the SSM $\langle T_6 \rangle_{pep,\ BP2000} = 12.51$.

1.5 Quasi-biennial Oscillations

Time variability of solar neutrino flux has been studied since the appearance of the first results of Homestake experiment [16]. In an early attempt to interpret the discrepancy between theoretical and observed flux, Sheldon [40] suggested a dependence of neutrino flux with solar activity, due to a time variable production rate of the neutrinos in the core of the Sun. The most famous evidence of the solar cycle is the time variation of sunspots number, with a characteristic period of about 11 years, extensively investigated in the past (see e.g., Ref. [41]). The occurrence of the solar cycle is related to the dynamo effect that generates the magnetic field of the Sun through the $\alpha - \omega$ process (the usual α-effect coupled with the differential rotation) [42]. The spatial behaviour of the solar cycle is related to the latitudinal migration of magnetic structures toward the solar equator as the 11-year cycle goes on, thus generating the characteristic "butterfly diagram" in both space and time domain. Superimposed on these large-scale effects, the presence of small-scale apparently stochastic fluctuations is observed [43]. However, through the analysis of Homestake data Sakurai [44] showed the existence of a quasi-biennial periodicity both in the solar neutrino flux and in the sunspot number. In order to make a connection between the periodicity observed both in solar neutrino and sunspot data, Sakurai claimed that fluctuations of the core temperature which is responsible of the pp chain efficiency, should be at the origin of this quasi-biennial modulation [44]. However the analysis by Lanzerotti [45] carried on a set of data which cover a longer time period, exclude any connection between events in the core with the ones which occur in the photosphere. The results of analysis of Kamiokande data over the Cycle 22 of the 11-yr solar cycle [25] showed that there is no correlation of the solar neutrino flux with sunspot numbers on 11-yr time scale. Apart from the 11-year cycle, intra-cycle periodicities have been discovered in many solar activity proxies. The most prominently recognized periods are in

the so called quasi-biennial oscillations (QBOs) range on time scales from 1.5 to 3.5 years [46, 47, 48, 49]. This periodicity is better detected in correspondence of main cycle maxima and it suffers, as the 11-year cycle, of period length modulation [50]. Quite interestingly, corresponding QBOs have been found also in other contexts related to solar variability, as in solar wind fluctuations, interplanetary magnetic field intensity, galactic cosmic ray (CR) flux [51, 52, 53, 54] energetic proton fluxes recorded in the interplanetary space [55] and in the solar rotation rate [56]. In they early work, Sakurai [44] invoked the presence of the quasi-biennial modulation for solar neutrino flux, in an attempt to solve the puzzle of missing neutrinos [57]. To date the puzzle has been solved in favour of neutrino flavour transformation [58], also implying a rest mass for neutrinos. Nevertheless, the origin of the biennial modulation of the solar neutrino flux and its interaction with the solar magnetic field are still debated [59, 60, 61, 62, 63, 64, 49]. These modulations should be induced by direct coupling of neutrino flux with solar magnetic field through neutrino magnetic moment. However, based on KamLAND data analysis constraint [65], assuming an upper bound for neutrino magnetic moment

$$\mu_\nu \leq 10^{-12}\mu_B \tag{1.97}$$

a neutrino oscillation length $\lambda_{osc} \approx 100 - 200$ km and magnetic field fluctuation with amplitude $\delta_B \approx 50 - 100$ kG, the deviation from the mean rate for SFP mechanism results to be of the order of $2.8 \cdot 10^{-2}$ % [65]. This means that the coupling of neutrino's magnetic moment and magnetic field gives negligible effects. On these basis, the most reliable mechanism seems to be the modulation of the production rate of the nuclear reactions or the variation of physical parameters, mainly the density, at the solar core. In order to affect appreciably the neutrino flux, the density fluctuations have to satisfy both the following requests at the position of the MSW oscillation [66, 67]:

(i) The correlation length of these fluctuations have to be of the same order of neutrino oscillation length;

(ii) The fluctuations amplitude have to be at least of $\sim 1\%$.

The most plausible mechanism, which in principle could originate fluctuations in matter density with the required properties, is the Alfvén/g-modes resonance [67]. The presence of density gradients along g-modes, can excite Alfvén waves resonantly, the resulting waveforms show sharp spikes in the density profile at radii comparable with the neutrino's resonant oscillation length. Hence, the study of short-term periodicities of the solar cycle should lead to improve knowledge of the global properties of the Sun, with particular regard to solar neutrinos and energetic particle emission. In particular, the possible coupling neutrino-solar activity can help to understand the physical processes occurring in the solar

deeper layers not accessible to helioseismic probing. In the present work we resume the study of the quasi-biennial solar cycle (see [49, 68, 69]) by investigating the time evolution of two different datasets, through the empirical mode decomposition (EMD), with particular attention to the statistical significance of the analysis. We claim that the modulation can be the manifestation of the interaction of solar neutrino flux with Alfvén/g-mode resonance modulated by an oscillating magnetic field deep within the solar radiative region.

1.5.1 The Neutrino Datasets

In order to investigate the relationship between solar neutrinos and magnetic activity, we report the results of EMD analysis carried out solar neutrino flux data recorded from the Homestake experiment (dataset ν_H) (a total of 108 records from 1970 to 1994 [70]) and from the SAGE experiment (dataset ν_S) (a total of 168 records from 1990 to 2008 [18]). The data from these two experiments cover a time window of $\sim$ 20 yr, passing through the maxima of two solar cycles (Cycles 21 and 22 for Homestake data and Cycles 22 and 23 for SAGE data). The EMD results for the two solar neutrino datasets have been compared with that obtained from the data of several solar cycle indicators: sunspot number (SN) and area (SA), flux of interplanetary protons in the energy range 0.50÷0.96 MeV/nucleon measured by the charged particles measurements experiment (channel P2) aboard the IMP8 spacecraft (P2) and cosmic ray intensity measured by the Rome neutron monitor with cutoff rigidity of 6 GV (NM).[6]

1.5.2 Results and Discussion

The EMD represents a powerful tool to study the solar QBOs and highly nonstationary signal. For more details on this technique, see Appendix A. Since these oscillations are high during the activity maxima [46, 48, 50] and their frequency is not constant from a cycle to another [50] the EMD is more suitable than the classical Fourier and wavelet analysis, to properly identify the QBOs. In fact it is well known that, in presence of nonstationary signals, the Fourier power spectrum, as well as the time integrated Wavelet spectrum, detect broader and lowered peaks. Since the Fourier transform looks for a global frequency and does not take into account possible period modulations, an underestimation of the contribution of the QBOs could occur. For each dataset, the QBO contribution to the original signal has been isolated through partial sum of IMFs oscillating with time scales in the range 1.4 yr $\leq \tau_i \leq$ 4 yr, where τ_i denotes a typical average period for the i-th IMF. The QBO contribution from the Homestake is shown in Fig. 1.6 toghether with the quasi-biennial signals of P2 and NM, while in Fig. 1.7 the QBO signal extracted from

[6] SN and SA data at: http://solarscience.msfc.nasa.gov/SunspotCycle.shtml; P2 data at: http://sdwww.jhuapl.edu/IMP/imp_cpme_data.html; CR data at: http://www.fis.uniroma3.it/svirco/.

SAGE data is shown toghether with the QBOs of sunspot data. As a reference, the time history of the sunspot area for the period of reference is reported in the lower panel.
After properly identifying the QBO components through the EMD from the different indicators, we compare them by evaluating Pearson's correlation coefficient. For each correlation coefficient, a confidence level of 95% is derived both through Fisher's transformation (Δr_F) and bootstrap methods (Δr_{boot}). Finally an estimation of the p-value (i.e. the probability to obtain by chance a correlation coefficient greater then that observed) is given by random phases method (P_{RP}) [71]. Results demonstrate that the correlation is stronger around the solar cycle maxima where the QBO amplitudes are higher. In particular, the QBOs isolated from Homestake data are in phase with particles data around the maxima of cycle 21 and 22, while QBOs isolated from SAGE data seem to be correlated with those of sunspot data near the maxima of cycle 22 and 23. This correlation is significant even extending the time window to 11 yr starting from mid-1991. In Tables 1.7, 1.8 and 1.9 are shown the results of the correlative analysis.

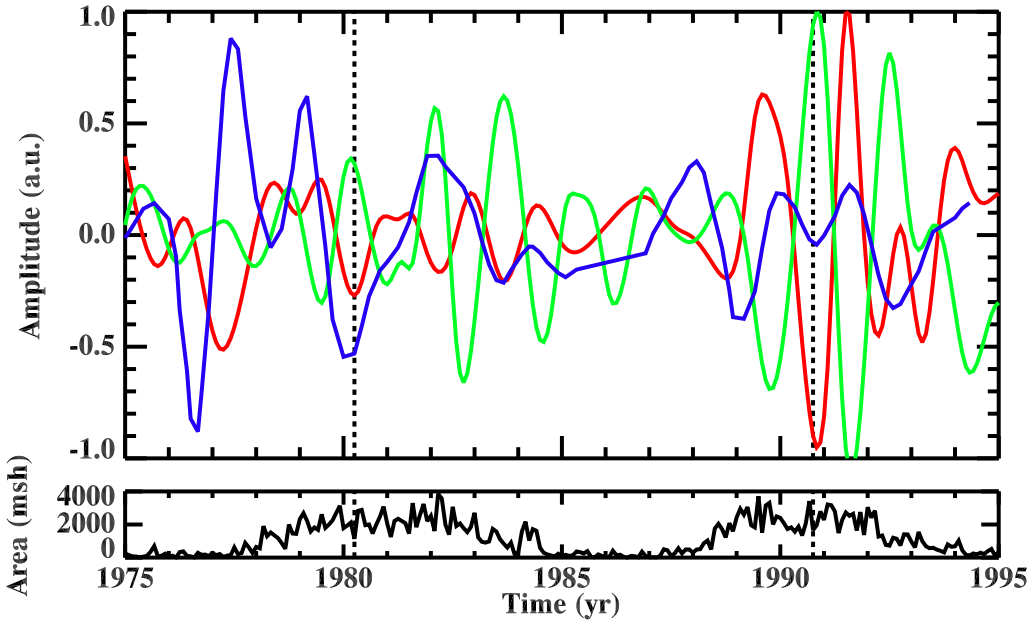

FIGURE 1.6: Upper panel: QBO isolated from Homestake data (blue line), P2 proton flux (red line) and galactic CRs (green line). Lower panel: Time history of the sunspot areas for the period of reference (in unit of millionths of a solar hemisphere). Dashed vertical lines correspond to maxima of solar cycles.

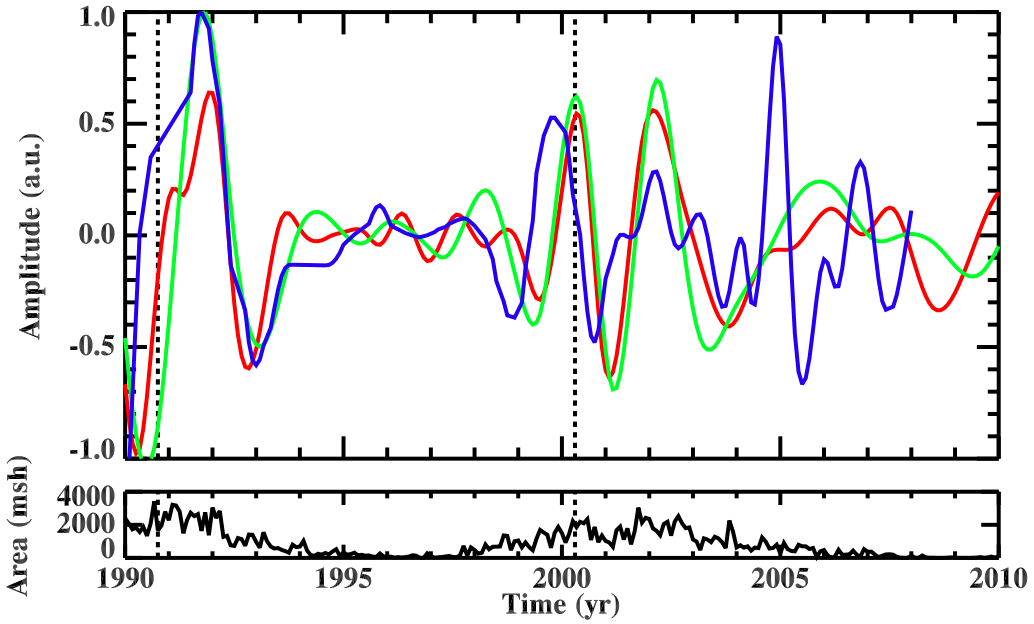

FIGURE 1.7: Upper panel: QBO isolated from SAGE data (blue line), sunspot area (red line) and sunspot number (green line). Lower panel: Time history of the sunspot areas for the period of reference (in unit of millionths of a solar hemisphere). Dashed vertical lines correspond to maxima of solar cycles.

TABLE 1.7: Results of correlative analysis for Homestake, energic proton and cosmic ray QBOs for 3 yr around maxima of cycle 21 (1980.25).

$X-Y$	r	Δr_F	Δr_{boot}	P_{RP}
$\nu_H - P2$	0.96	[0.90, 0.98]	[0.91, 0.98]	0.01
$\nu_H - NM$	−0.90	[−0.96, −0.75]	[−0.95, −0.78]	0.06
$P2 - NM$	−0.98	[−0.99, −0.95]	[−0.99, −0.97]	0.01

TABLE 1.8: Results of correlative analysis for Homestake, energic proton and cosmic ray QBOs for 3 yr around maxima of cycle 22 (1990.75).

$X-Y$	r	Δr_F	Δr_{boot}	P_{RP}
$\nu_H - P2$	0.93	[0.82, 0.97]	[0.82, 0.97]	0.03
$\nu_H - NM$	−0.99	[−0.99, −0.97]	[−0.99, −0.98]	0.01
$P2 - NM$	−0.92	[−0.97, −0.80]	[−0.96, −0.85]	0.03

TABLE 1.9: Results of correlative analysis for SAGE, sunspot number and area QBOs for 11 yr starting from mid-1990.

$X-Y$	r	Δr_F	Δr_{boot}	P_{RP}
$\nu_S - SA$	0.58	[0.46, 0.69]	[0.45, 0.69]	< 0.01
$\nu_S - SN$	0.67	[0.56, 0.75]	[0.53, 0.78]	< 0.01
$SA - SN$	0.89	[0.85, 0.92]	[0.86, 0.92]	< 0.01

1.5.3 The Magneto-Gravity Modes

The observed correlation between solar quasi-biennial cycle and solar neutrino flux fluctuations on quasi-biennial time scales could represent a direct observation of instabilities induced by quasi-biennial dynamo effects in the deeper regions of solar radiative zone. The theory of coupling between large scale magnetic fields and solar matter has been investigated by Burgess *et al.* [67]. In particular, in the presence of backgroud magnetic fields of reasonable intensity, density gradients allows g-modes to excite Alfvén waves resonantly, causing mode energy to be funnelled along magnetic field lines away from the solar equatorial plane. Magneto-gravity waves are described by the usual compressible, ideal magnetohydrodynamic equations, namely the continuity equation for mass density

$$\frac{\partial \rho}{\partial t} + \nabla \cdot (\rho \mathbf{v}) = 0 \tag{1.98}$$

the momentum equation with the gravity term

$$\rho \left[\frac{\partial \mathbf{v}}{\partial t} + (\mathbf{v} \cdot \nabla) \mathbf{v} \right] = -\nabla P + \rho \mathbf{g} + \frac{1}{4\pi} \left[(\nabla \times \mathbf{B}) \times \mathbf{B} \right] \tag{1.99}$$

and the magnetic field induction equation

$$\frac{\partial \mathbf{B}}{\partial t} = \nabla \times (\mathbf{v} \times \mathbf{B}) \tag{1.100}$$

The system of equations can be closed by relating the pressure P to the mass density through an energy equation

$$\frac{dP}{dt} - \gamma \frac{P}{\rho} \left(\frac{d\rho}{dt} \right) = -(\gamma - 1) Q \tag{1.101}$$

where d/dt is the total time derivative, γ is the ratio of heat capacities, and Q is the sum of all energy density sources and losses, such as heat conductivity, viscosity and ohmic dissipation. Assuming an equilibrium situation where the velocity field and current density are both zero, equations 1.98-1.101 are linearized by using low-frequency approximation, in order to filter out the pressure p-modes, and an exponential density profile. A plane geometry with a local gravity directed along the z-axis and the background magnetic field along the x-axis is used. Background quantities depend on z, and a standard mass-density profile coming from solar models $\rho_0 = \rho_c \exp(-z/H)$ is assumed (here the density at the solar centre ρ_c and the density height-scale H are constant) [66]. All fluctuating quantities depends on space and time through

$$A(x, y, z, t) = A(z) \exp[i(k_x x + k_y y - \omega t)] \tag{1.102}$$

If we consider a slowly varying background magnetic field, we expect that the system, which varies on times of the order of the helioseismic characteristic periods, has enough time to adapt the configuration corresponding to the instantaneous amplitude of the background magnetic field (adiabatic hypothesis). Under this assumption, by using a background magnetic field which varies in time according to $\mathbf{B}_0 = B_0 f(\omega_0 t)\, \mathbf{e}_x$, where $\omega_0 \ll \omega$, we obtain two equations for the Fourier coefficients of magnetic field fluctuations $\mathbf{b} = \mathbf{B}/[B_0 f(\omega_0 t)]$ and the velocity fluctuations $\mathbf{v}$

$$\begin{cases} -i\omega \mathbf{b} = & ik_x \mathbf{v} - (\nabla \cdot \mathbf{v})\, \mathbf{e}_x \\ -i\omega \mathbf{v} = & -\frac{\nabla P'}{\rho_0} + \frac{\rho' \mathbf{g}}{\rho_0} + v_A^2(t) \left[-\left(\frac{\partial b_x}{\partial z} - ik_x b_z \right) \right] \mathbf{e}_x \end{cases} \tag{1.103}$$

("primed" quantities are fluctuations). The above set of equations is formally identical to that founded by Burgess *et al.* [67], apart for the fact that in our case

$$v_A^2(t) = \frac{B_0^2}{4\pi\rho} f^2(\omega_0 t) \tag{1.104}$$

is a time-dependent Alfvén speed. After some algebraic calculations we finally obtain an equation for the fluctuating magnetic field, whose solution determines all other fluctuating quantities

$$\left[1-\frac{k_x^2 v_A^2(t)}{\omega^2}\right]\frac{db_z}{dz^2}-\frac{N^2(z)}{g}\frac{db_z}{dz}+k_\perp^2\left[\frac{k_x^2 v_A^2(t)}{\omega^2}1+\frac{N^2(z)}{\omega^2}\right]b_z=0 \tag{1.105}$$

where the perpendicular wave-vector is

$$k_\perp^2=k_x^2+k_y^2 \tag{1.106}$$

and we defined the Brunt-Väsälä frequency

$$N^2(z)=g(z)\left[\frac{1}{\gamma P_0}\frac{dP_0}{dz}-\frac{1}{\rho_0}\frac{d\rho_0}{dz}\right] \tag{1.107}$$

which represents the characteristic frequency of the system. Equation (1.105) describes magneto-gravity waves. In the limit $B_0 \to 0$ it leads to the standard helioseismic g-modes. In absence of gravity and $B_0 = const$. Equation (1.105) describes Alfvén waves with frequency $\omega = \Omega_A = k_x v_A$. By retaining both gravitation and magnetic field a new singular point occurs when the coefficient of the second derivative term in Equation (1.105) vanishes. Since this happens at $\omega = \Omega_A$, it can be viewed as being due to resonance between g-modes and Alfvén waves [67]. Let us come back to the Sun. Since Ω_A varies with the distance from the centre of the Sun, while, according to usual helioseismology the g-modes frequency is independent on position, the resonance occurs at a particular radius inside the Sun, namely when Ω_A crosses the frequency of one of the g-modes. The occurrence of the resonance depends on the value of B_0. This means that, in our case, the existence of the resonance is modulated in time by the term $f(\omega_0 t)$, that is the resonance is time-dependent. Solutions of Equations (1.103) gives the eigenvalue spectrum as roots of the trascendental equation [67]

$$\chi = A(n,\, t)\cosh(\chi) \tag{1.108}$$

where

$$\omega = k_x C_0(t)\cosh(\chi) \tag{1.109}$$

where $C_0(t)$ represents the time-dependent Alfvén velocity at the solar centre, and

$$A(n,\, t)=\frac{k_x C_0(t)}{4Nk_\perp H}\left[2\pi n - i\ln\left|\tan\frac{\pi}{\gamma}\right| \pm \pi\left(\frac{1-\gamma}{\gamma}\right)\right] \tag{1.110}$$

Accordingly, the instantaneous resonant position is given by

$$z_r(n,\, t) = 2H\,\ln\{\Re[\cosh\chi(n,\, t)]\} \tag{1.111}$$

The time dependence of solution of Equation (1.108) results in a modulation of the distance between neighboring resonant layers with the same period of the background magnetic field. This is shown in Figure 1.8, where we report the time evolution of the distance as a function of the position of the resonance

$$dz_r\left(n,\, t\right) = z_r\left(n+1,\, t\right) - z_r\left(n,\, t\right) \tag{1.112}$$

The background magnetic field is assumed to have a sinusoidal variation, with a profile defined by

$$f\left(\omega_0 t\right) = \cos^2\left(\frac{\omega_0 t}{2}\right) + \epsilon \sin^2\left(\frac{\omega_0 t}{2}\right) \tag{1.113}$$

where $\omega_0 = \pi\ \mathrm{yr}^{-1}$ and the function f is defined in the interval $[\epsilon,\, 1]$ (we used $\epsilon = 10^{-3}$). As noted by Burgess *et al.* [67], for reasonably values of the background magnetic field intensity, the distance between resonant layers, at the neutrino's resonant region, are of the order of the neutrino's oscillation length. In particular the spikes which occur in density profiles, as a consequence of the resonance, could increase the probability of interactions between neutrino flux and solar matter [66].
In Figure 1.9 we report the time evolution of the lagrangian density perturbation

$$\frac{\delta\rho}{\rho} \approx C - \left\{\exp\left[-\left(z - z_r\left(n,\, t\right)\right)/H\right]\left(1 + i2d\left(n,\, t\right)\right) - 1\right\}^{\frac{1-\gamma}{\gamma}} \tag{1.114}$$

where $d\left(n,\, t\right)$ denotes the growing factor of the eigenfrequency $\omega = \omega_1\left(1 + id\right)$, and C is defined as follows

$$C = \frac{\Gamma\left(\gamma^{-1}\right)}{\Gamma\left(-\gamma^{-1}\right)}\left[\frac{\gamma v_\phi\left(n,\, t\right)}{c_s i\sqrt{\gamma - 1}}\right]^{2/\gamma}\left(\frac{\gamma - 1}{4\gamma} + \frac{\gamma^2 k_\perp^2 H^2}{\gamma - 1}\right) \tag{1.115}$$

where $v_\phi\left(n,\, t\right) = \omega_1\left(n,\, t\right)/k_x$. As it is evident, the resonance oscillates in time with a frequency ω_0.

1.5.4 Quasi-biennial Dynamo as Source for Magnetic Fluctuations

Recent analysis carried on BiSON and GOLF data [72] show that quasi-biennial signal has the same amplitude for p-modes at all frequencies. On the other hand the 11-yr modulation affects predominantly high frequency p-modes occuring on shallow regions close to the solar surface. This suggests that the dynamo mechanism responsible of the mean cycle has its origin at shallow regions of the solar interior (resonably located near the bottom of the shear layer extending 5% below the surface), while another separated quasi-biennial dynamo mechanism could be originated in deeper layers. In this scenario, the quasi-biennial dynamo located in the inner layers of the Sun, are more likely to induce a

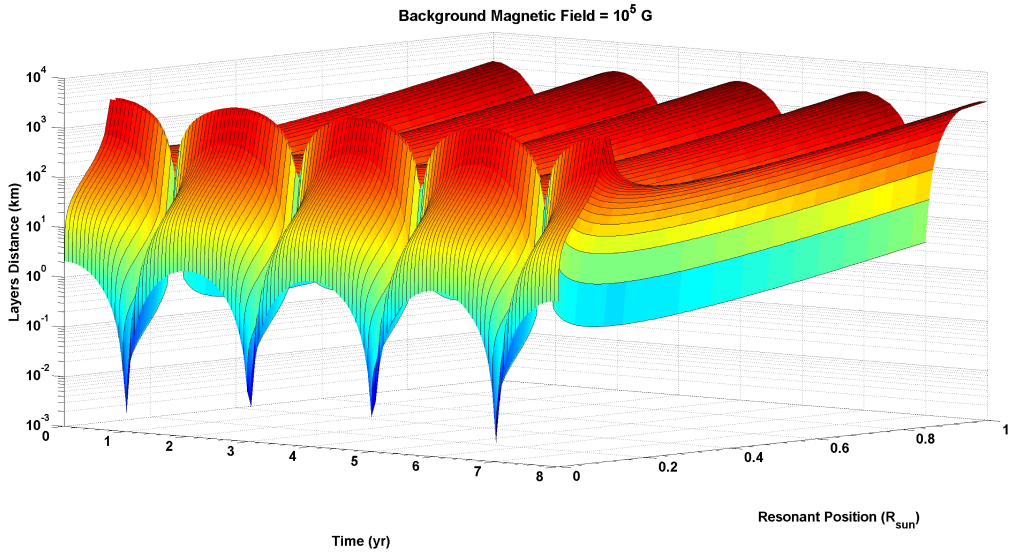

FIGURE 1.8: Time evolution of the distance between resonant Alfvén layers. In the $y-z$ plane are reproduced respectively the position of the resonances (in solar radius units) and the distance between the resonant layers (in km). The x axis represents the time (in yr).

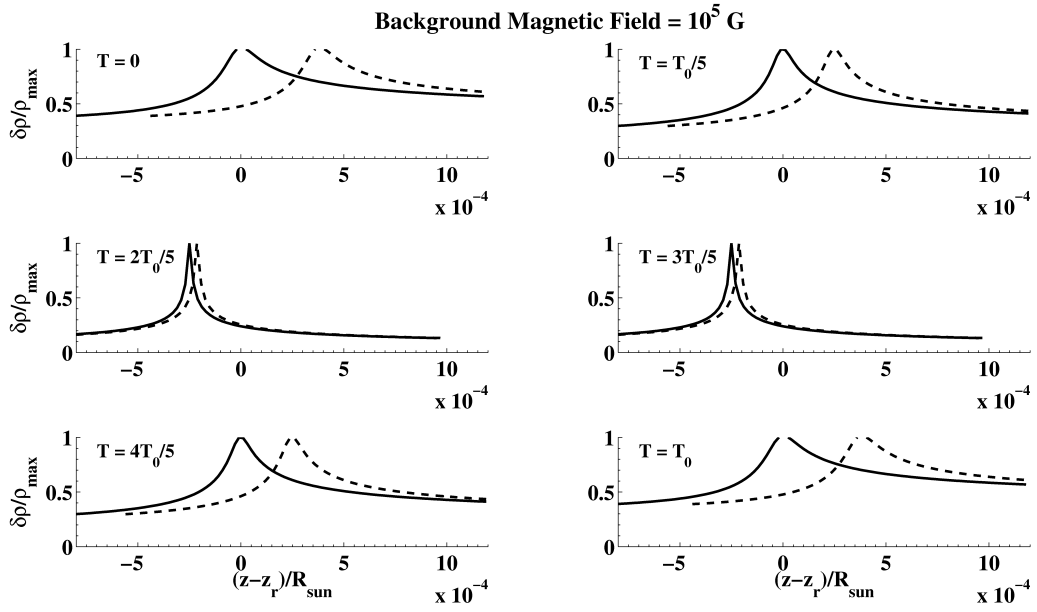

FIGURE 1.9: Time evolution of neighbouring density profiles in the region $z_r \sim 0.3\, R_{sun}$.

fluctuating background magnetic field. The latter is the key ingredient of the model since allows that correlation length between density spikes variates in time. This mechanism could thus produce the observed variations, at the quasi-biennial scale, of the solar neutrino flux. The modulation of solar neutrinos and the coupling with magneto-gravity modes is of great interest for solar physics. This coupling could represent a new way to investigate the physical properties in the very inner layers of the Sun thus playing the role of a "telescope" for the solar interior.

Chapter 2

Galactic Cosmic Rays

2.1 Cosmic Rays

With the expression "Cosmic Ray" are intended stable particles and nuclei which have galactic or extragalactic origin. They are grouped in two main categories, namely "primary" and "secondary" cosmic rays. Primary cosmic rays are electrons, protons and nuclei syntetized in stars, while secondary cosmic rays are the nuclei which are not abundant in stellar nucleosynthesis, so that they are more likely produced in the interaction of primaries with interstellar medium [73].
Cosmic Ray particles have energies from $few \cdot 100$ MeV up to 3 EeV (1 EeV = 10^{20} eV). Their spectrum is reported in Fig. 2.1 [73]. It is characterized by two principal features: a steepening between 10^{15} and 10^{16} eV, called *knee* and an *ankle* around $10^{18.5}$ eV.
It is not clear how they are originated and how they propagate in the interstellar medium, such as the mechanisms which allow the particles to enhance their energies. The modelization of their propagation is in fact not trivial. Cosmic rays propagate essentially through diffusion and convection (advection). The former can be carried through collisions (diffusion in real space) or reacceleration (diffusion in momentum space).
From the interaction of primary cosmic rays with athmospheric nuclei mesons are produced: charged mesons decay in muons and neutrinos, while by neutral meson decays electrons and photons are produced.
The measurements of cosmic rays are made at atmospheric, surface and underground level. At the surface level muons are mainly observed as well as electrons, positrons and photons from cascades initiated by the meson decay. At the underground level are detected muons and neutrinos.

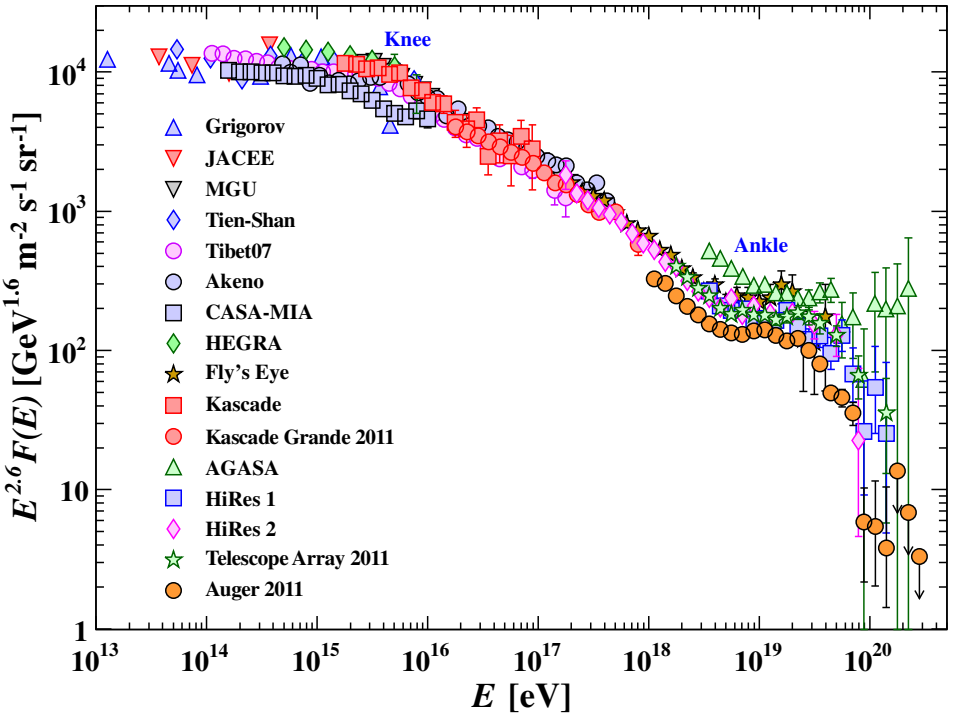

FIGURE 2.1: CRs differential intensity as a function of the energy from Fig. 26.8 of [73]. For more details see [73] and references therein.

2.2 Galactic Cosmic Rays

Particles with energies of order of TeV, basically of galactic origin, are a useful tool to investigate galactic structures. Since Galactic Cosmic Rays (GCRs) travel in a magnetized medium, the main parameter which characterize their motion is the gyro-radius that can be expressed in the form

$$\rho = 223 \frac{E\,(TeV)}{B\,(10^{-10}T)}\ \text{AU} = \frac{E\,(TeV)}{B\,(10^{-10}T)} 10^{-3}\ \text{pc} \tag{2.1}$$

thus assuming galactic magnetic field intensity of order $O\left(10^{-10}T\right)$, the values of gyro-radius is smaller than the size of the Milky Way (which is 30 kpc in diameter and 300 pc in thickness).

2.2.1 Cosmic Ray Anisotropy

The distribution of GCRs depends on time reference frame respect to which are binned the event counts. In particular counting the event rate in the solar year time frame,

where the duration of a year is measured in a reference frame where the Sun is at center (365 days/yr), gives information on solar system scales, while event rate measured in the sidereal year time frame, where the duration of a year is measured respect to the fixed stars reference frame (366 days/yr), gives information on the interaction of CRs with structures on galactic scales.

In the solar time frame, an anisotropy is observed in the daily flux of Cosmic Rays. This is due to the revolution of the Earth around the Sun respect to the reference frame of CRs which can be considered at rest on solar system scales. Thi effect is known as Compton-Getting effect [74], in particular the intensity of the flux varies according to the expression:

$$\frac{\Delta I}{\bar{I}} = (\gamma + 2)\,\frac{v}{c}\cos\theta \tag{2.2}$$

where γ is the spectral index, which in the energy range of interest is equal to 2.7. Assuming for the Earth a velocity of 30 km/s, the amplitude of the anisotropy is of $\sim 0.05\%$, with the maximum at 6:00 h Local Solar Time.

When event counts are histogrammed in sidereal hourly bins, solar daily effects cancel out on several years of data taking and, a part from atmospheric effects which may induce spourius sidereal signals, a CG effect is expected due to the motion of Solar System around galactic center, assuming that CRs are at rest. The analysis of data collected from Air Shower arrays and underground cosmic muon detectors over several years show the evidence of a sidereal anisotropy with an excess in the so called "tail in" region, at $\sim 80°$ RA, and a deficit in the "loss-cone" region, at $\sim 200°$RA (e.g. [75, 76, 77]). The CG scenario used to interpret this anisotropy seems not to adequately describe the observed profile, thus indicating that CR flux corotates with Galactic Magnetic Field (GMF) [76]. A possible source for this anisotropy can be the diffusion due to shock of supernova remnants (SNR) and stellar wind. However since CRs travel for millions of years, their interaction with irregular GMF components is expected to randomize particle orbits. The characteristic of Cosmic Ray Sidereal Anisotropy are summarized in Tab 2.2 at the end of Sec. 2.3. Recent results of data analysis from IceCube and IceTop experiments show that the profile of CRs anisotropy depends on their energy [78, 79].

2.2.2 Interaction of Galactic Cosmic Rays and Interplanetary Magnetic Field

It is known that solar magnetic field influence the flux of Cosmic Rays with rigidity up to $\sim$ 10 GV since the expanding magnetized plasma partially screening the incoming particles. At the energy range of Galactic Cosmic Rays no effects are expected from solar cycle. Neverthless the analysis of diurnal anisotropy in Tibet ASγ experiment show a disagreement with CG effect at energies < 6 TeV [82], while data taken from Matsushiro

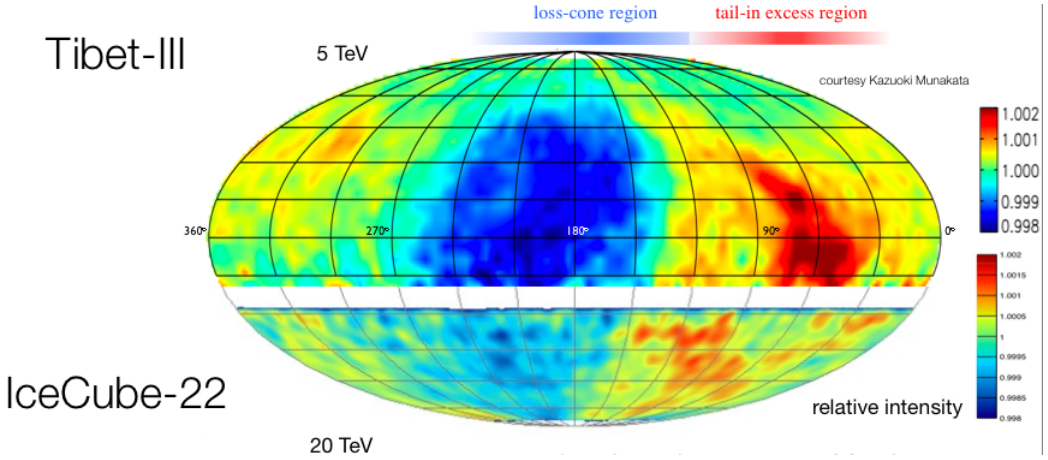

FIGURE 2.2: Cosmic Ray anisotropy as function of celestial coordinates reconstructed with the results of Tibet ASγ (upper region [76]) and IceCube (lower region [80]). [81]

experiment from 1987 to 2008 show the presence of an extra anisotropy overlapped to the CG [83]. This anisotropy of $O\left(10^{-2}\%\right)$ is correlated with 11-yr solar cyle, with the maximum of the correlation coefficient at a lag of 26 months (see Fig. 2.3).

2.3 Galactic Cosmic Ray Detectors

In this section we resume the principal properties of some Cosmic Ray Detectors. Four of them are Cosmic Muons Detectors (MACRO, LVD and Borexino, MINOS and Matsushiro experiments), while the other two are Air Shower Arrays (Tibet ASγ and Milagro experiments).[1] The characteristics of the detectors referred to the study of cosmic rays are summarized in table 2.1.

2.3.1 MACRO

MACRO (Monopole Astrophysics and Cosmic Ray Observatory) was an underground detector designed to detect supermassive magnetic monopoles predicted by Grand Unified Theories of electroweak and strong interactions [84, 85, 86]. It was able to operate also as Neutrino and Cosmic Ray Detector. In particular several works were dedicated to both high and low energy atmospheric neutrino physics, high energy neutrino astronomy, search for WIMPs and cosmic ray astrophysics through the monitoring of high energy underground muons. It was organized in a modular structure, with two supermodules, each of dimensions 12.6 m×12 m×4.8 m. Each supermodule was divided in two modules, each of them consisting of 10 horizontal planes of streamer tubes, 12 m×6 m. The lowest and highest planes are separated by a 25 cm of liquid scintillator, while the innermost planes are separated by a 60 g/cm^2 absorber of low activity Gran Sasso Rock. The lateral walls

[1] For the details on Borexino and SuperKamiokande detectors see Sec. 1.3.5 and 1.3.3, respectively.

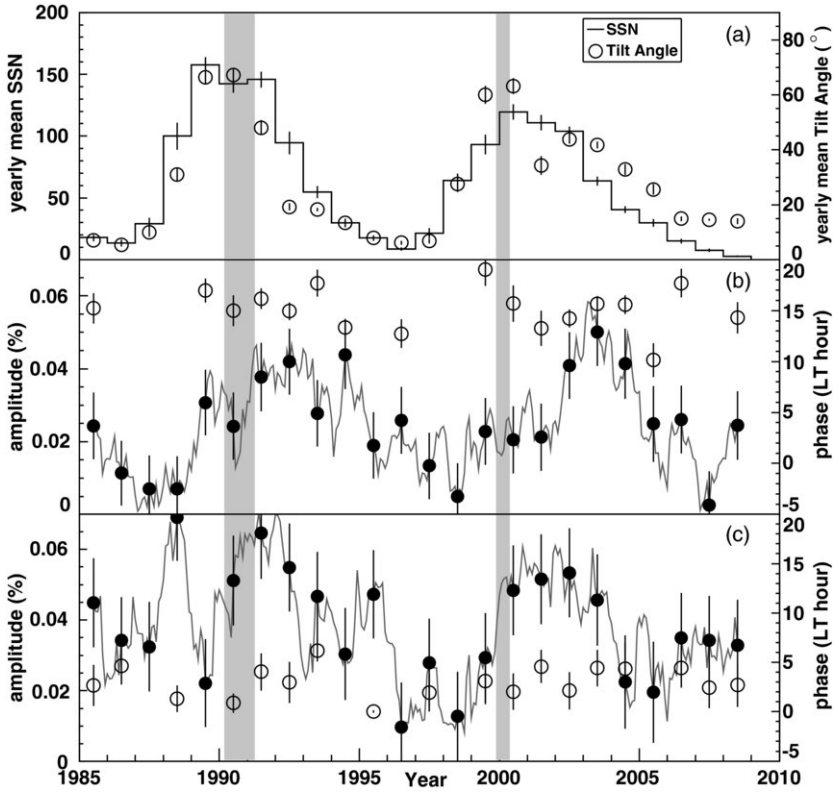

FIGURE 2.3: Long-term variation of the diurnal anisotropy observed by Matsushiro in 1985-2008 [83].

consist of stacked tanks of liquid scintillator, 25 cm thick, sandwiched between six verical streamer tubes planes. The structure of the detector allows a stereoscopic reconstruction. For more details of muon track reconstruction and event cuts, see Ref. [84].

2.3.2 LVD

The Large Volume Detector (LVD) is a 1 kt liquid scintillator detector designed to study neutrino bursts from gravitational stellar collapses [87]. The detector is structured in three towers, each of them divided in 35 "portatanks" (5 columns $\times$7 levels). Each portatank is made of 8 scintillation counters (1.5 m^2). Totally the detector is made by 840 counters, with an active volume of 13 m$\times$23 m$\times$10 m active volume.

2.3.3 MINOS

The MINOS experiment is dedicated to the study of neutrino oscillations [88]. It consists of a neutrino source and a near detector at Fermi National Accelerator Laboratory in Batavia IL, and a far detector at the Soudan Underground Mine State Park in northern Minnesota. This last is a scintillator and steel tracking calorimeter located at 2100 mwe and can be used also for the monitoring of cosmic muons of energy of energy $E_{th} > 0.73$ TeV.

2.3.4 Matsushiro

The Matshushiro underground muon detector [83](sometimes reffered to as Zohzan, according to the name of the hill under which it is located), consists of two horizontal layers vertically separated by 1.5 m. Each layer is divided in a 5×5 square array. Each elements is made of a 1 m×1 m×0.1 m plastic scintillator viewed by two PMTs of 12.7 cm diameter. An event is registered when for each detector, two PMTs simultaneously detect pulses each shaped with a width of 300 ns. For the analysis carried in [83], hourly muon rates have been considered detected in a pad of 17 detectors allowing a measure both of eastern and western rates (East-Western method).

2.3.5 Tibet ASγ

The Tibet ASγ is an air shower detector located at Yangbajing, in Tibet, China [76]. In its definitive phase (Tibet III) is composed of 497 fast timing (FT) and 36 density (D) detectors, covering a surface area of 22050 m^2. Each FT detector contains a plastic scintillator plate and a 2 inch PMT. A 0.5 cm thick lead plate is placed on top of each counter in order to increase the sensitivity by converting a γ ray into an electron-positron pairs. A CR event is considered when any fourfold coincidence occurs in the FT counters.

2.3.6 Milagro

The Milagro observatory is a water Cherenkov located in New Mexico, at 2630 m above sea level [77]. The detector is composed of 80 m×60 m×8 m pond filled with $\sim$ 23 million liters of purified water and protected by a light-tight cover. The central pond is instrumented with two layers of PMTs: the upper layer (450 PMTs under 1.4 m of water) detects air shower electrons and gamma rays, while the lower layer (273 PMTs 6 m under the surface) detects gamma-hadron separation. The direction of an air shower is reconstructed using the relative timing of the PMTs hit in the top layer of the pond. The pond is surrounded by a 200 m×200 m array of cylindrical, polyethilene "outrigger" tanks of 2.4 m diameter and 1 m height. Each tank is filled with $\sim$ 4000 l of water and is monitored by a single PMT located at the top. Cosmic ray anisotropy is studied by comparing the rates measured from couple of "telescopes" located in the same forward and backward angle respect to the 0° hour angle (Forward-Backward method).

2.3.7 IceCube and IceTop

IceCube is a neutrino observatory located at the geographic South Pole [78]. Ice Top is an air shower array located above Ice Cube at 2835 m altitude respect the ice sheet [79]. IceCube was completed in December 2010. It consists of 84 strings, each equipped with 60 optical sensors between 1450 and 2450 m below the surface. IceTop consists of 81 stations

organized in a triangular grid at 125 m of distance each other, and covering an hexagonal area of 1 km^2. Each station consists of two tanks of frozen clean water separated by about 10 m. Each tank contains two optical sensors which detect Cherenkov light emitted by leptons present in cosmic ray air shower. IceCube is able to detect cosmic muons with energies corresponding to primary cosmic ray median energy from 20 TeV up to 400 TeV, while IceTop is dedicated to the observation of cosmic ray of PeV energies.

TABLE 2.1: Table of Air Shower and Muons Detector Properties. For each experiment are reported the category (MD for muons detector, AS for Air Shower detector), time window covered (according to the reference cited), depth (in meters water equivalent), particles energy and acceptance angle of the detector. In the energy column: E_{th} is the energy threshold, while E_m is the median energy recorded in the channel considered. For Matsushiro detector E and W denotes East and West channels respectively, while, for Milagro experiment are reported the zenith angle dependence of the median energy.

Detector	Class	Time Window (mm/yy)	Depth (mwe)	Energy (TeV)	Accept. $[\cos(\theta)]$
MACRO [84]	MD	1991 ÷ 2000	3800	$E_{th} = 1.3$	> 0.3
LVD [87]	MD	01/01 ÷ 12/08	3800	$E_{th} = 1.3$	> 0.5
Borexino [89]	MD	05/07 ÷ 05/11	3800	$E_{th} = 1.833$ (for T_{eff}computation: $E_{th} = 1.3$)	any
MINOS [88]	MD	08/03 ÷ 08/08	2100	$E_{th} = 0.73$ (at surf)	$[0.05 - 0.92]$
IceCube [78]	MD	04/07 ÷ 04/11	2000	$E_m = 20$ (CR)	any
Matsushiro [83]	MD	1985 ÷ 2008	220	$E_m^E = 0.660$ $E_m^W = 0.549$	-
Tibet ASγ [76]	AS	1990÷2008	-	$E = 4 \div 300$	-
Milagro [77]	AS	07/00 ÷ 07/07	2630 m above sea level	$E_m = 4(5° \div 10°)$ $E_m = 7(35° \div 40°)$	-

TABLE 2.2: Table of Air Shower and Muons Detector results for CR Sidereal Anisotropy.

Detector	Class	E_m (TeV)	Anisotropy Direction (RA, dec)	$\delta I = \frac{\Delta N}{\langle N \rangle}(10^{-3})$
SuperKamiokande 06/96÷05/01 [90]	MD	10	E: $(75^\circ \pm 7^\circ,\ -5^\circ \pm 9^\circ)$ D: $(205^\circ \pm 7^\circ,\ 5^\circ \pm 10^\circ)$	E: (1.04 ± 0.20) D: $-(0.94 \pm 0.14)$
Tibet ASγ 02/97÷11/05 [76]	AS	10	E 1: $(\sim 80^\circ$, -) D: $(\sim 200^\circ$, -) E 2: $(\sim 309^\circ, \sim 38^\circ)$	E 1: ~ 1 D: ~ -1 E 2: ~ 0.5
Milagro 07/00÷07/07 [77]	AS	6	D: $(189^\circ, -)$	D:$(-2.49 \pm 0.02_{stat} \pm 0.09_{sys})$
IceCube 05/09÷05/10 [78]	MD	20	E: $(80.8^\circ,\ -49.7^\circ)$ D: $(219.7^\circ,\ -52.0^\circ)$	E: ~ 0.9 D: ~ -1.1
		400	E: $(256.6^\circ,\ -25.9^\circ)$ D: $(73.1^\circ,\ -25.3^\circ)$	- D: ~ -0.7
IceTop 2009÷2012 [79]	AS	400	E: $(182^\circ,\ -55.9^\circ)$ D: $(83.7^\circ,\ -35.7^\circ)$	- D: $(-1.58 \pm 0.46_{stat} \pm 0.52_{sys})$
		$2 \cdot 10^3$	D: $(79.4^\circ,\ -37.2^\circ)$	D: $(-3.11 \pm 0.38_{stat} \pm 0.96_{sys})$

2.4 Interaction with Solar Cycle as Observed in Gran Sasso Cosmic Muon Data

Combined toghether, cosmic muon flux data recorded in the experiments of MACRO, LVD and Borexino span a period of 21 yr complessively. This represents a usefull probe to investigate long-term variations in cosmic muon flux. In fact, a part from the seasonal variation due to atmospheric variations (see next section), the likelihood and Lomb-Scargle analysis of the Gran Sasso dataset show a strong evidence of an 11yr component of an amplitude of 0.4% and the first maximum in March 1996 [91] . This is an interesting result, since no solar cycle influence is expected for Cosmic Rays with rigidity >10 GV.
Neverthless the analysis carried out in Ref. [91] cannot permit to recostruct the muon 11-yr mode, since for the likelihood analysis it is necessary to choose *a priori* a function. If the muon 11-yr oscillations depend on solar cycle, then it is a no-trivial task decide which function can adequately describe oscillations which are expected to be in this case non-stationary.
For this reason we have reanalized Gran Sasso muon flux data through the EMD method, which allows to obtain in adaptive way the principal oscillations embedded in the data. The same method applied to sunspot number and atmospheric temperature allows a direct comparison of the cosmic muon 11-yr mode with the long term variations in the atmospheric temperature, such as with the main solar cycle, thus providing a powerful tool to investigate more accurately the nature of the signal.

2.4.1 Cosmic Muons Flux and Correlation with Atmospheric Temperature

Cosmic muons detected in the underground experiments are originated by the decay of charged mesons, which are produced in the interaction of primary cosmic rays with atmospheric molecules (see Sec 2.1). The production rate of muons is strictly dependent on the variation of the stratospheric temperatures. In fact, when the temperature increases, the density of the air decreases, thus resulting in an enhancement of the probability that a meson decay before interacting.
The correlation between cosmic muon rate and atmospheric temperature is usually expressed through the relation

$$\frac{\Delta R_\mu}{\bar{R}_\mu} = \alpha_T \frac{\Delta T_{eff}}{\bar{T}_{eff}} \tag{2.3}$$

where $\bar{R}_\mu$ is the mean cosmic muon rate, $\Delta R_\mu = R_\mu - \bar{R}_\mu$, $\bar{T}_{eff}$ is the average effective temperature, $\Delta T_{eff} = T_{eff} - \bar{T}_{eff}$ and α_T is the atmospheric depth-weighted temperature coefficient.

The effective temperature is evaluated as an averaged temperature weighted with atmospheric depth, that is

$$T_{eff} = \frac{\sum_i \left[T\left(X_i\right)/X_i\right]\left[\exp\left(-X_i/\Lambda_\pi\right) - \exp\left(-X_i/\Lambda_N\right)\right]}{\sum_i \left(1/X_i\right)\left[\exp\left(-X_i/\Lambda_\pi\right) - \exp\left(-X_i/\Lambda_N\right)\right]} \tag{2.4}$$

where X_i is the atmospheric depth at the i-th pressure level, $\Lambda_\pi = 160$ g/cm^2 and $\Lambda_N = 120$ g/cm^2 are the atmospheric attenuation length for pions and nucleons, respectively. The relation between pressure and atmospheric depth considered is $X = P/g$, with g the acceleration of gravity.

For this work we have computed the effective temperature from atmospheric parameters measured at Pratica di Mare station and available on the Integrated Global Radiosonde Archive (IGRA) web site.

The Integrated Global Radiosonde Archive (IGRA) is a dataset from the National Climatic Data Center (NCDC), collecting radiosonde and pilot balloon observations at more than 1500 globally distributed stations. Radiosondes are launched at different periods of day and transmit their measurements to ground receiving stations, where they are processed into: pressure, temperature, dewpoint depression, geopotential height, wind speed and direction. At the present, NCDC database provides data recorded from each station during its period of activity and monthly data from all stations at two periods of day, i.e. at 00 and at 12 UTC. Monthly data are given at several pressure levels and mean values are given only if at least 10 values for a particular station, month, nominal time and level are available. For more details see Ref. [92].

2.4.2 Results of EMD Analysis of Cosmic Muon Flux Recorded at Gran Sasso

The dataset obtained by combining data from MACRO, LVD and Borexino detectors, consists of 223 monthly differential rate, from January 1991 to May 2011 [91]. The energy threshold of the muons detected at Gran Sasso is 1.3 TeV.

In Fig. 2.4 are superposed the Gran Sasso muon flux data and the relative variation of effective temperature calculated from atmospheric data.

The Lomb-Scargle periodogram of monthly muon data indicate a long-term component with a period of $\sim$ 10 yr. As we can see in Fig. 2.5, where the periodogram of the whole dataset is compared with that obtained from the individual experiments, the main contribution to the significance comes from LVD dataset.

Cosmic muon flux, effective temperature and sunspot number data have been decomposed into IMFs using an SD parameter value of 0.01. In Fig 2.6 is shown the significance of the IMFs extracted through the sifting method, according to the Wu-Huang test . From the figure we can see the presence of an 11-yr component for muons with a significance higher

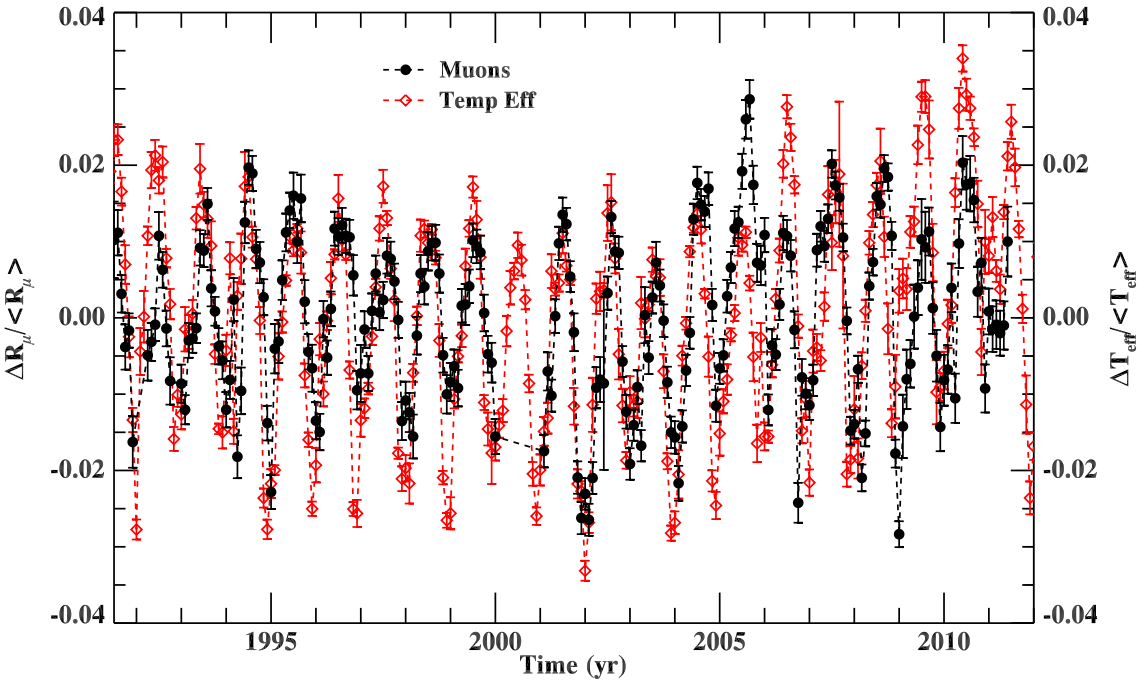

FIGURE 2.4: Superposition of relative variation of Cosmic Muon flux as recorded from Gran Sasso experiments (black dotted points) and effective temperature calculated from atmospheric parameters recorded at Pratica di Mare station (red rhombic points).

than 99%. The results of EMD analysis of muon, temperature and sunspot number are summarized in Figs. 2.7÷2.9 . We can see the anticorrelation between cosmic muon and sunspot number 11-yr modes, represented for both by the 5th IMF. An IMF oscillating with characteristic period of $\sim$ 10 yr is also present for the effective temperature (5th IMF) which, on the other hand , seems no correlated with 11-yr mode detected in cosmic muon dataset.

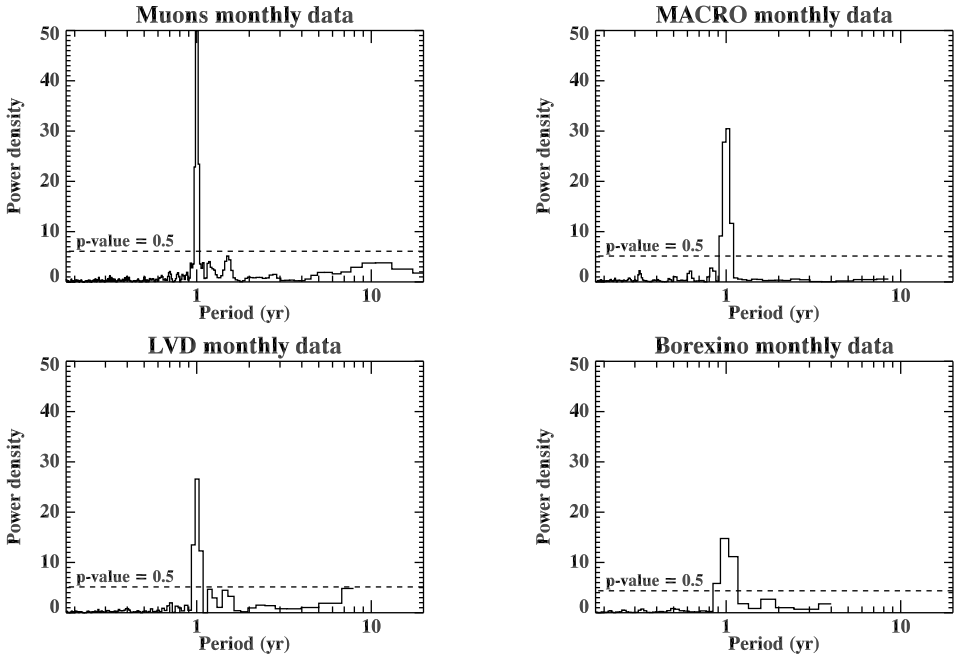

FIGURE 2.5: Lomb-Scargle periodograms of monthly averaged muon data from the whole dataset and from the individual experiments.

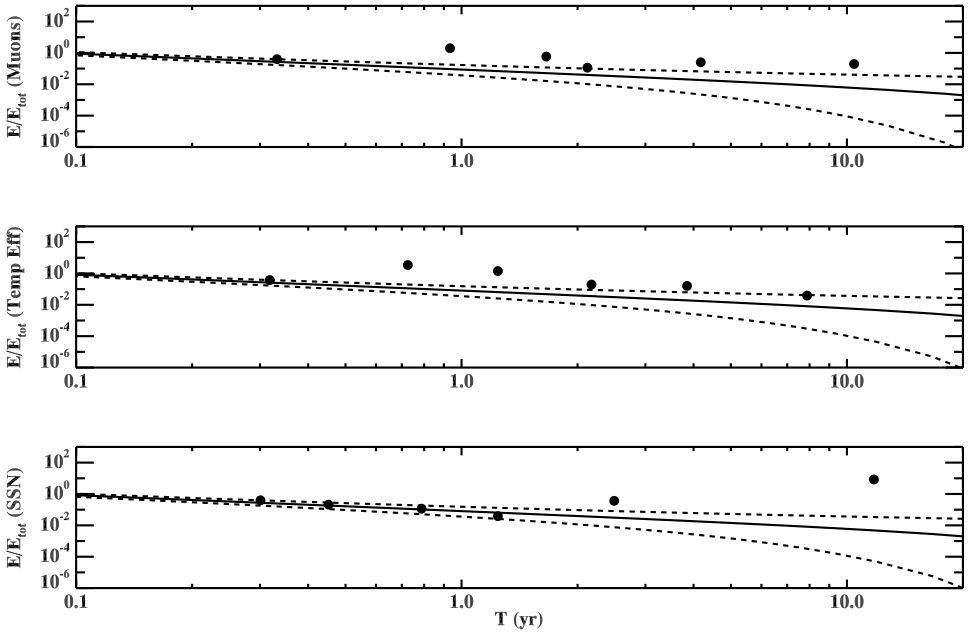

FIGURE 2.6: Wu-Huang singnificance test for cosmic muon (upper panel), effective temperature (middle panel) and sunspot number (lower panel) IMFs. The dashed lines represent the 1th and 99th percentile of the expected distribution expected for white noise signal. For each dataset, the energy content of each IMF is normalized to the 0th IMF energy, since the 0th order IMF is supposed to be predominantly noise fluctuations.

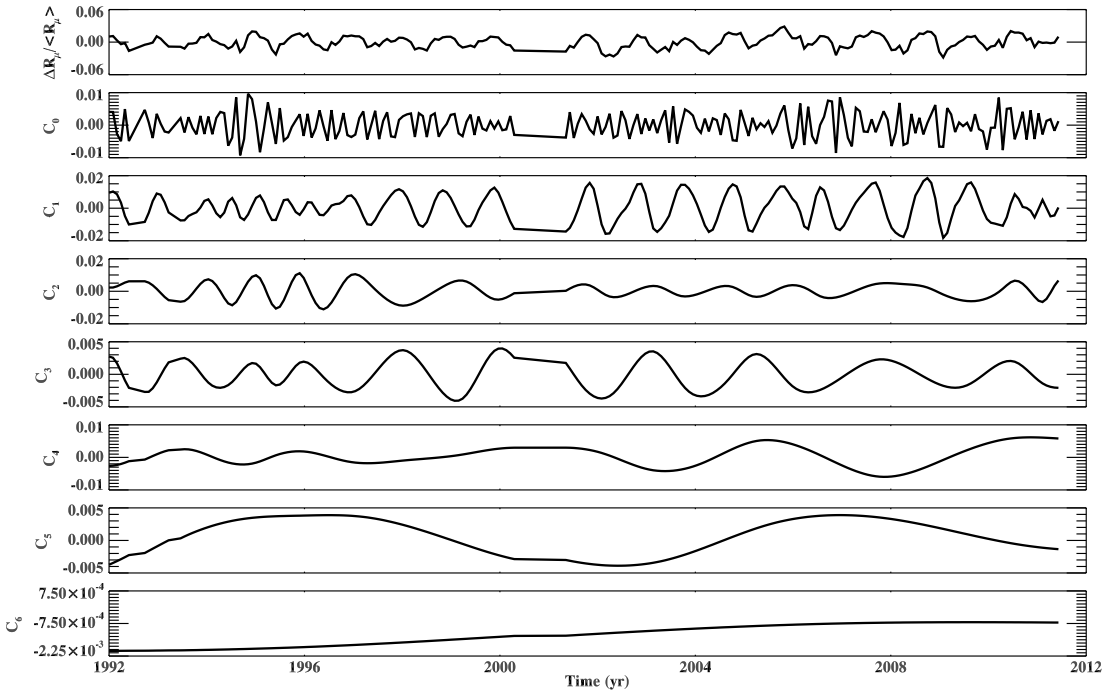

FIGURE 2.7: IMFs obtained from cosmic muon data. The original dataset is shown in the upper panel.

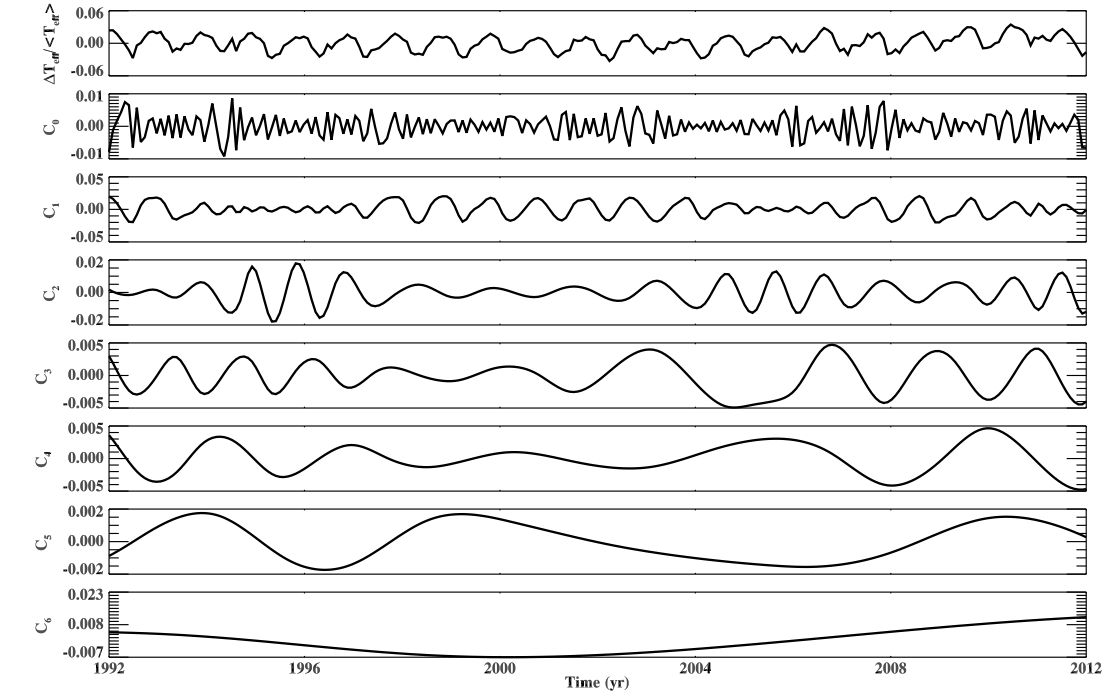

FIGURE 2.8: IMFs obtained from effective temperature data. The original dataset is shown in the upper panel.

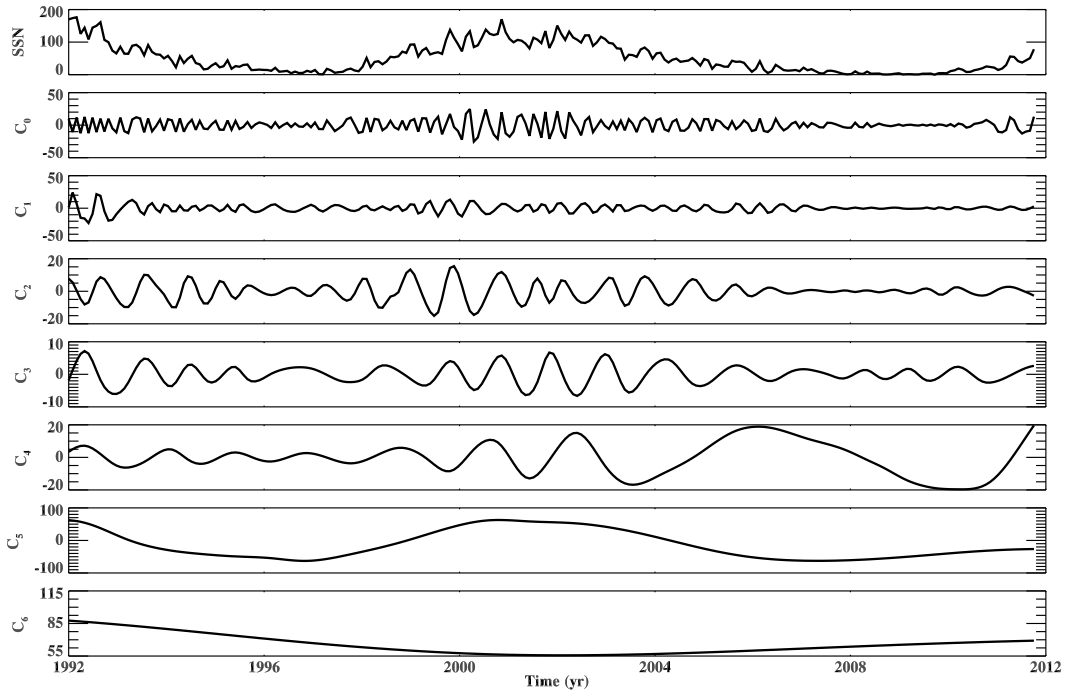

FIGURE 2.9: IMFs obtained from sunspot number data. The original dataset is shown in the upper panel.

The 11-yr signal both for cosmic muons and for sunspot number has been reconstructed with the correnspondent 68% CL through Monte Carlo method, where 250 realizations of the original dataset have been produced using random number normally distributed with mean value the center of the individual data point and with standard deviation equal to the data error. Each realization is then decomposed into IMFs. Finally the resulting signal with the corresponding 68% CL are computed by the mean signal and the standard deviation of the IMFs with characteristic period in the range 8÷16 yr. In Fig. 2.10 are reported the 11-yr mode extracted from muon and sunspot data with the corresponding 68% CL, while in Fig. 2.11 is shown the histogram of correlation coefficient obtained by comparing 10000 realizations of couples of muon and SSN 11-yr signals, where each new dataset has been obtained from the original by the generation of a random number normally distributed with mean value and standard deviation respectively equals to the center value and error of the individual data point.

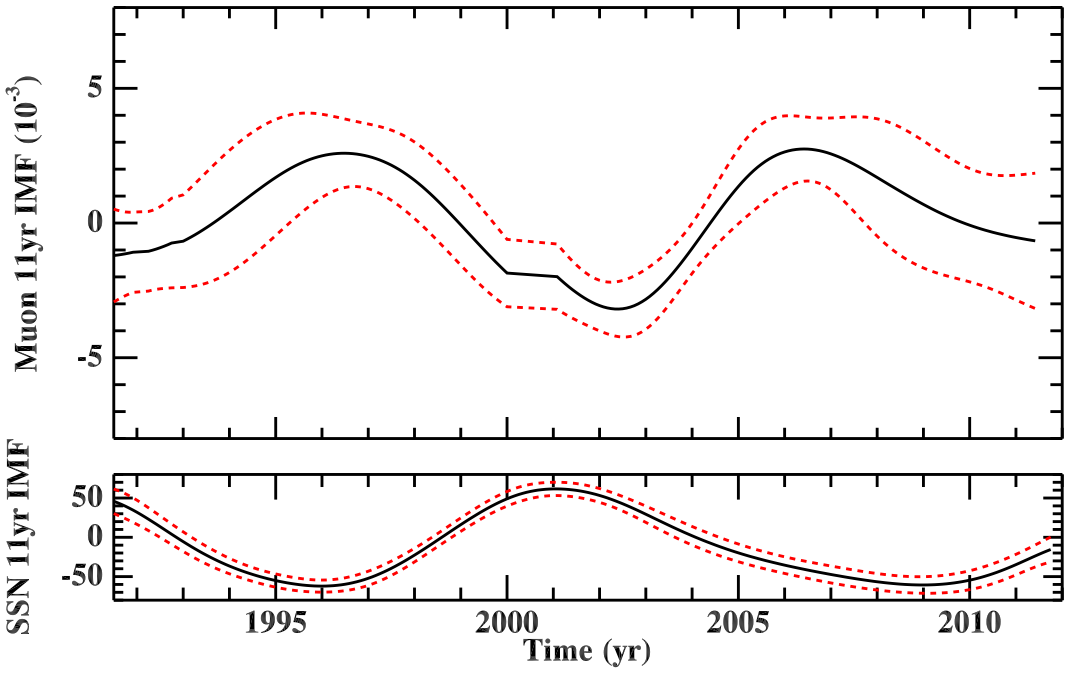

FIGURE 2.10: In the upper panel is shown the 11 yr mode reconstructed for cosmic muon data with the corresponding 68% CL, while in the lower panel the 11-yr mode and the corresponding 68% CL are shown for sunspot number.

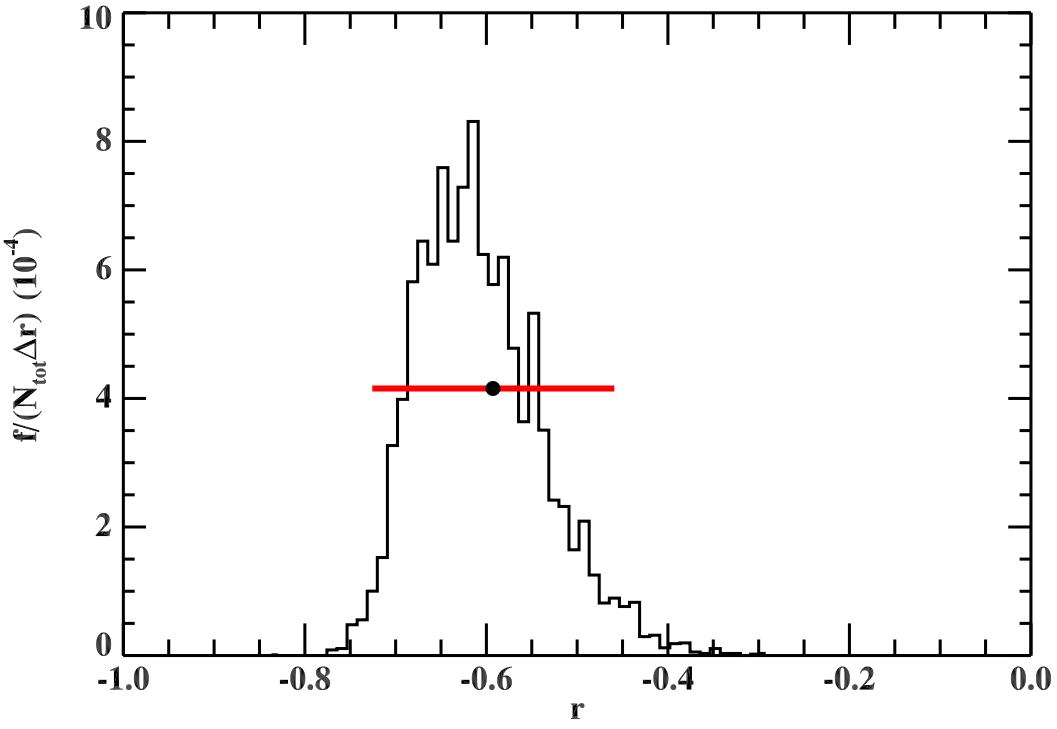

FIGURE 2.11: Histogram for correlation coefficient obtained by 10000 realizations of muon and sunspot 11-yr signals. The filled dot represents the mean value of the correlation coefficient, while the red bar show the 95% CL. The mean value of r is -0.59, and the 95% CL is $[-0.73, -0.46]$.

2.4.3 Discussions

The EMD analysis carried on cosmic muon flux recorded at MACRO, LVD and Borexino detectors have confirmed the presence of an 11-yr mode in the cosmic muon signal as claimed in [91], with the principal contribution to the significance coming from LVD dataset. Furthermore the anticorrelation found with the sunspot 11-yr cycle can represent a confirmation of the 11-yr modulation in cosmic muon anisotropy observed from [83]. As suggested in the paper of Matshushiro collaboration, at the origin of this anticorrelation for TeV cosmic rays there be an energy exchange of cosmic rays with current sheet in the far regions of heliosphere. If confirmed, further analysis on modulation in solar time frame of galactic cosmic ray flux can provide important informations on the structure of magnetic field at heliospheric scales and on the mechanisms of interaction of cosmic rays with their magnetic fields.

Chapter 3

Time Variability of the Fine-Structure Constant

3.1 Fundamental Constants

In physics fundamental constants describe properties of Nature which are the same in any point and in every instant of time. They are different from mathemathical constants since those are pure numbers which can be evaluated with arbitrary precision (for example through a series), while physical constants require a measurement in order to determine their value. Furthermore their numerical value depends on the unit system adopted. In certain cases it is possible to derive dimensionless constants. Even if this possibility avoids the ambiguity on their numerical value, their origin, as well as that of the other dimensional constants, still represents a theoretical challenge.

Although the experiences based on experimental observations indicates that this constants have the same value despite of the point in space and in time the experiment is performed, we can ask ourself if their value has been the same even on cosmological scales, that is if their value have been the same throughout the evolution of the Universe. The hypotesis of a time evolution of constant values on cosmological time was suggested from Dirac [93, 94] who, by observing the extremely low ratio between gravitational and electromagnetic interaction for elementary charged particles (which for a system composed of a proton and an electron is of the order $O\left(10^{-39}\right)$), as well as the ratio between live time of the Universe and atomic time unit, argued that fundamental constants such as G may vary in time as the inverse of the time evolution of the Universe ($G \sim t^{-1}$). This hypotesis, known as Large Number Hypotesis, has been recently reformulated in modern unification theories of fundamental interactions in the so called "Hierarchy Problem" [95], which is focused instead on the extremely low ratio between the mass of elementary particles and the Planck mass unit defined as

$$M_P = \sqrt{\frac{\hbar c}{G}} = 1.22 \cdot 10^{19} \text{ GeV} \tag{3.1}$$

Even if it seems unlikely that the value of G may scale as t^{-1} as suggested from Dirac, time evolution of fundamental constants are in principle not forbidden, but particular attention has to be paid when functional forms for constants such as $G = G(t)$ are introduced in the equations where they appear, as pointed out by Barrow [96], who noted that, while in newtonian mechanics it is possible to replace G with $G(t)$, the same substitution applied to the Einstein field equations lead to a contraddition when we impose the conservation of momentum-energy tensor. The Brans-Dike [97] theory offers an example of a varying coupling constant, since in the equations which describe the gravitational field G is replaced by the inverse of a scalar field Φ^{-1}. At the same time Einstein equations of gravity are modified in order to take in account of the vanishing covariant divergence of energy-momentum tensor. Other theories have been developed taking into account of varying speed of light or electron charge, the description of which is out of the aim of our work. Here we remark one of the fundamental consequences of such time (and possibly also spatial) dependence of fundamental constants, that is the violation of the Einstein's Equivalence Principle. This principle consists of three main statements [98]:

- The **Weak Equivalence Principle (WEP)** which states that the trajectory of a freely falling neutral body is independent of its structure and composition;
- The **Local Lorentz Invariance (LLI)** states that the result of a non-gravitational experiment in a freely falling laboratory is independent of the velocity of the frame;
- The **Local Position Invariance (LPI)** states that the result of a measure in a non-gravitational experiment is independent of where and when it is performed.

The **Strong Equivalence Principle (SEP)** extend the above principles also to gravitational experiments [99].

3.2 Spatio-Temporal Pattern for the Fine-Structure Constant from QSO Absorption Spectra

The most stringent evidence of a variation in space and time of a fundamental constant comes from the analysis of Quasi-Stellar Objects (QSO) absorption spectra recorded at Keck and VLT telescopes [100, 101], which shows evidence of spatio-temporal variations for the fine-structure constant defined as

$$\alpha = \frac{e^2}{\hbar c} = 7.2973525698\,(24) \times 10^{-3} \tag{3.2}$$

where e is the electron charge, $\hbar$ is the reduced Planck constant and c the speed of light.

3.2.1 The W. M. Keck Observatory and HIRES Spectrometer

The W. M. Keck Observatory [102] consists of two astronomical telescopes with 10 m diameter primary mirror located at Mauna Kea, Hawaii (USA), at an elevation of 4.145 meters and at $\sim 20^\circ$ N latitude.
The light of quasars used for the QSO analysis are collected from HIRES (High Resolution Echelle Spectrometer) facility. It consists of a grating cross-dispersed, echelle spectrograph which operates from 300 up to 1000 nm [103].
The Keck data used in the QSO analysis were acquired whilst HIRES had only one CCD chip, so that several exposure are needed to yeld full wavelength coverage [101].

3.2.2 The Very Large Telescope and the UVES Spectrometer

The Very Large Telescope [104] is located in the Atacama Desert (Chile) at 2635 m altitude and $\sim 25^\circ$ S latitude. It consists of four telescopes of 8.2 m diameter primary mirror. The structure is complemented by four Auxiliary Telescopes of 1.8 m aperture.
The QSO spectra are recorded from the UVES (Ultraviolet and Visual Echelle Spectrograph) facility, which spectral range cover from 300 up to 1100 nm. Respect Keck/HIRES spectra, for that recorded from UVES one observation is needed to cover almost the entire spectral range [101].

3.2.3 Absorption Lines in Astronomical Spectroscopy

The stellar electromagnetic spectrum is characterized by absorption and emission lines due to the interaction of electromagnetic radiation and the matter through which it travels.
An absorption profile reflects the different processes involved. The intensity reduction is essentially due to a continuum absorption through the scattering between photons and unbounded electrons, which is known as Thomson scattering and which cross section is proportional to $\alpha^2\, r_e^2$, with $r_e = h/m_e c$ the classical radius of electron , and to the transitions of electron states as consequence of the absorption of photon. In this case the probability of absorbing photon has a lorentzian distribution which is broadened by the effect of the relative motion of the atoms to the center of mass reference frame (Doppler effect) and other effects which take place at smaller scales respect to the photon mean free path and generally denoted in literature as “turbulent” (or “microturbulent”) broadening. The convolution of the lorentzian distribution and the Doppler effect gives a Voigt distribution for the cross section, which functional form will be discussed later.
The intensity as a function of the frequency can be expressed through the expression

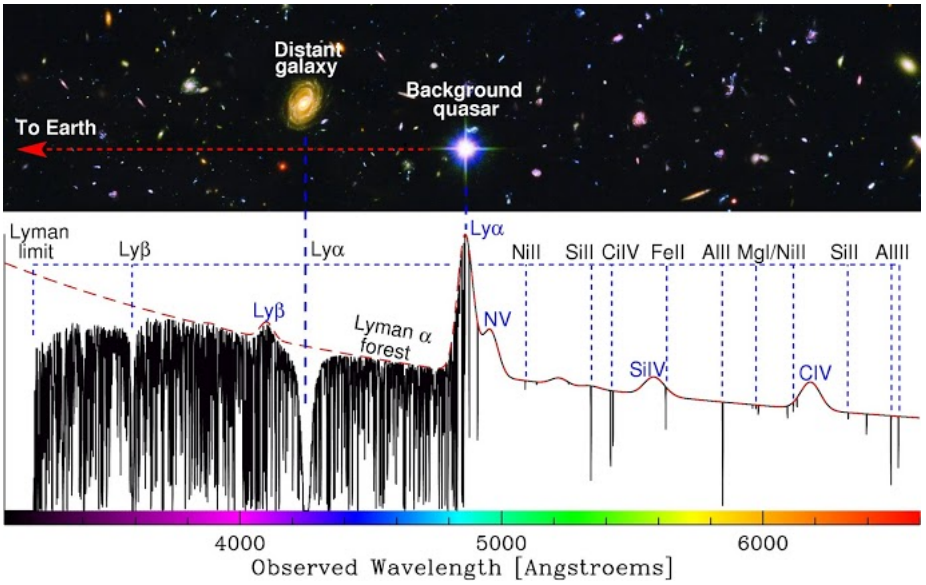

FIGURE 3.1: Quasar Spectrum as observed at Earth. Image from[106].

$$I_\nu = I_\nu^C \exp\left(-\tau_\nu\right) \tag{3.3}$$

where τ_ν is the optical depth of the absorbing medium and that is proportional to the column density (that is the number of particles per unit area along a given sightline) and the absorbing coefficient. For the absorption due to a transition of frequency ν_0 in the rest frame of the cloud, the absorbing coefficient is proportional to

$$\kappa_\nu \propto \frac{H\left(v,\, a\right)}{\Delta\nu_b} \tag{3.4}$$

where $\Delta\nu_b$ is the broadening due to Doppler effect and turbulent term and $H\left(v,\, a\right)$ is the Voigt profile

$$H\left(v,\, a\right) = \frac{a}{\pi}\int_{-\infty}^{+\infty} dy \frac{e^{-y^2}}{\left(v-y\right)^2 + a^2}$$

where $v = \left(\nu - \nu_0\right)/\Delta\nu_b$ while $a = \Gamma/\left(4\pi\Delta\nu_b\right)$ is the transition damping constant normalized with respect to the broadening width. At the spectrograph the spectrum results in a convolution of the intensity profile with the instrumental response or IP (Instrumental Profile) [105].

Typical QSO spectum is characterized by a series of absorption lines in the ultraviolet region. These absorption lines are due to electron transitions in the intervening hydrogen atoms (see [105] and references therein). The absorptions from lower H I column densities come essentially from interstellar medium in which galaxies are embedded, while larger H I column densities are originated from dark halo of galaxies disks. In the visible region of

the spectrum, there are several absorption lines due to ionized metals[1] probably associated to galactic halos or disks.

3.2.4 Spatio-Temporal Variations of Fine-Structure Constant from the Many Multiplet Method for Analysis of QSO Absorption Spectra

The absorption lines of heavy elements (far from Ly-α forest region of the spectrum) can give informations on fine-structure constant at the redshift where the absorption clouds are located. In particular the analysis of multiplet transitions instead of the alkali doublet systems results in an increased sensitivity and statistics for the determination of difference of fine-structure constant value at the redshift of the absorption system respect to that measured at laboratory [105] This is possible if the relativistic corrections to the energy interval for transition to multiplet states are taken into account [107, 108]. The new expression for the frequency after the introduction of correction factors, can be written in the form

$$\omega_z = \omega_0 + q_1 x + q_2 y \tag{3.5}$$

where $x = (\alpha_z/\alpha_0)^2 - 1$ and $y = (\alpha_z/\alpha_0)^4 - 1$, with α_z and α_0 denoting the fine-structure constant value at redshift z and in the laboratory, respectively. By retaining only the terms of order $O(\Delta\alpha/\alpha_0)$, where $\Delta\alpha/\alpha = (\alpha_z - \alpha_0)/\alpha_0$, Eq. 3.5 can be rearranged in the form

$$\omega_z = \omega_0 + qx \tag{3.6}$$

with $q = q_1 + 2q_2$. The value of $\Delta\alpha/\alpha$ is obtained by minimization of $\chi^2$of a multiple Voigt profile fit with $\Delta\alpha/\alpha$ as an additional free parameter [109].

The results of analysis carried on 128 absorber systems from QSO spectra recorded at Keck/HIRES give $\Delta\alpha/\alpha = (-0.574 \pm 0.102) \times 10^{-5}$, resulting in a smaller value of the fine-structure constant in the past [100].

The recent analysis of Keck/HIRES QSO absorption spectra integrated with that from VLT/UVES (141 and 154 absorber systems respectively) indicate how a weighted mean model seems not adequately to capture all the informations in the data [101]. Infact the weighted mean of $\Delta\alpha/\alpha$ from the VLT/UVES data is $\Delta\alpha/\alpha = (0.208 \pm 0.124) \times 10^{-5}$, which seem in contraddiction with the previous results obtained by Murphy *et al.* . The different locations of the two observatory suggests a spatial pattern for the values of $\Delta\alpha/\alpha$ as the solution of this apparent paradox. The dipole model applied to the combined data is preferred at 4.1σ respect the monopole-only model, with an angular distribution pointing in the direction RA=(17.3 ± 1.0) hr and dec=(-61 ± 10) deg and amplitude $0.97^{+0.22}_{-0.20} \times 10^{-5}$ [101]. Aside from the dipolar structure, a significant monopole at low-z has been detected,

[1] Here intended as elements heavier than helium.

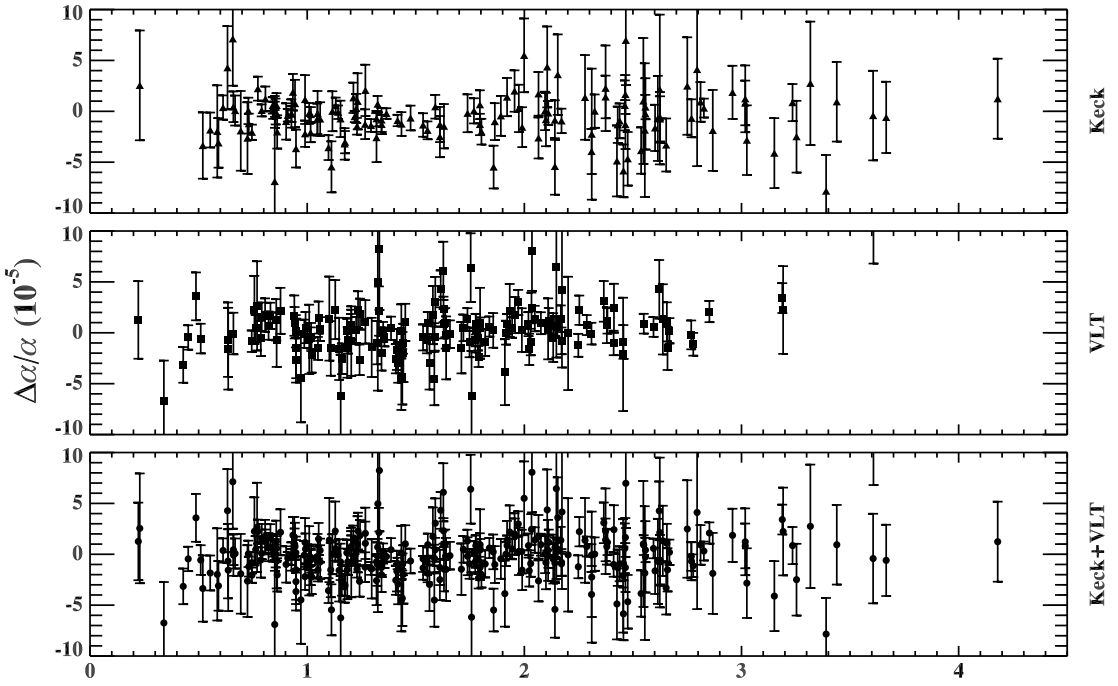

FIGURE 3.2: Distribution along redshift coordinate of the $\Delta\alpha/\alpha$ for Keck/HIRES (upper panel), VLT/UVES (middle panel) and data obtained from combinig both samples (lower panel).

at which significance the Mg isotopic abundances at the low redshift respect to terrestrial values may contribute, since the isotopic spacing scales as $\Delta\omega_i \propto \omega_0/m_i^2$, where m_i is the mass of the i-th specie [100, 101].

3.3 EMD Analysis of $\Delta\alpha/\alpha$ from Keck and VLT Data

In this section we show the results of the EMD analysis applied to Keck/HIRES and VLT/UVES QSO absorption spectra[110] in order to investigate the possible existence of temporal structures in the $\Delta\alpha/\alpha$ values. The distribution respect to the redshift coordinate of the dataset from each observatory and the sample obtained by combining the two datasets are shown inf Fig. 3.2. We will refer to the latter sample as the "combined sample". For the analysis we have considered 293 of the global sample of 295 absorber systems, since we have excluded the two outliers individuated through the Least Square Trimmed analysis, that is the two samples for which the absolute value of the standardized residual respect the weighted mean $\Delta\alpha/\alpha$ value exceeds 3. All the data have been considered combining statistical errors with random errors as indicated in Ref. [101].
The EMD analysis have been carried over Keck and VLT datasets and that obtained combining both datasets. In particular the three datasets have been rearranged in a regular grid of 100 bins in redshift coordinate, from the minimum and the maximum of z of each

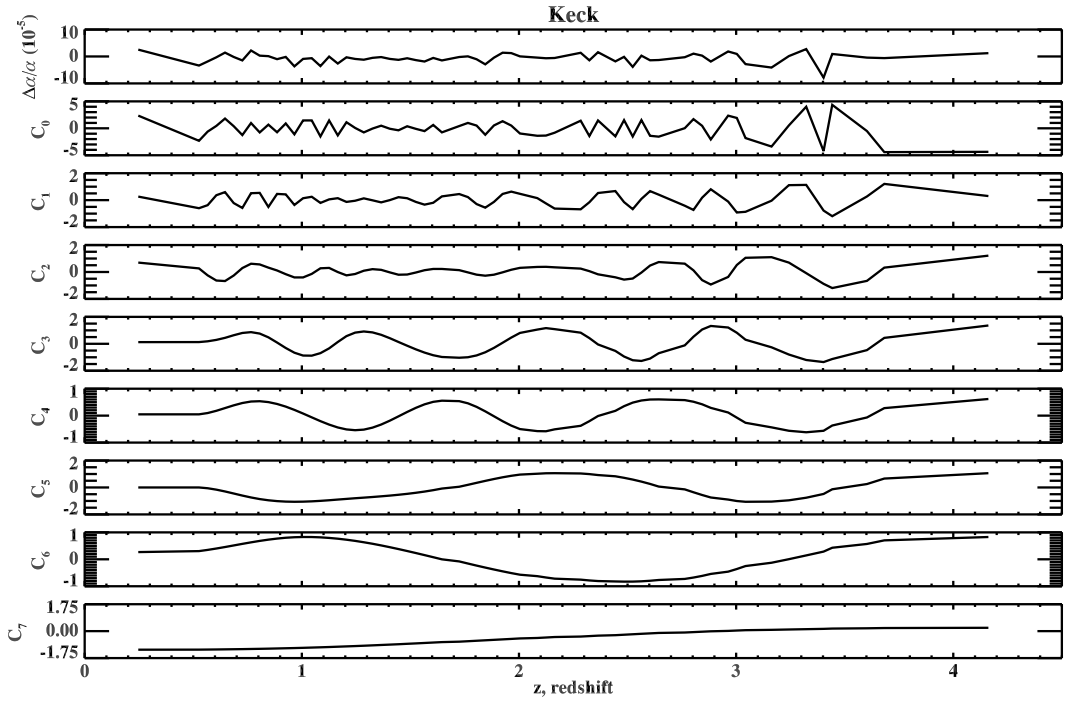

FIGURE 3.3: IMFs obtained from Keck/HIRES dataset.

sample. Each empty bin has been removed and the new datasets consist of 65 $\Delta\alpha/\alpha$ values (obtained as weighted mean of the values which lie in the same bin) for Keck telescope, 59 for VLT and 74 for the combined sample. The results of EMD analysis (with SD parameter equal to 0.01) are shown in Figs. 3.3÷3.5 where are reported the IMFs extracted from Keck, VLT and combined samples respectively. We note that the Keck IMFs $C_5 \div C_7$ are similar to the same order VLT IMFs. These modes looks distorted in the combined sample. Probably this distortion may be a reflection of the spatial anisotropy of the $\Delta\alpha/\alpha$ values.

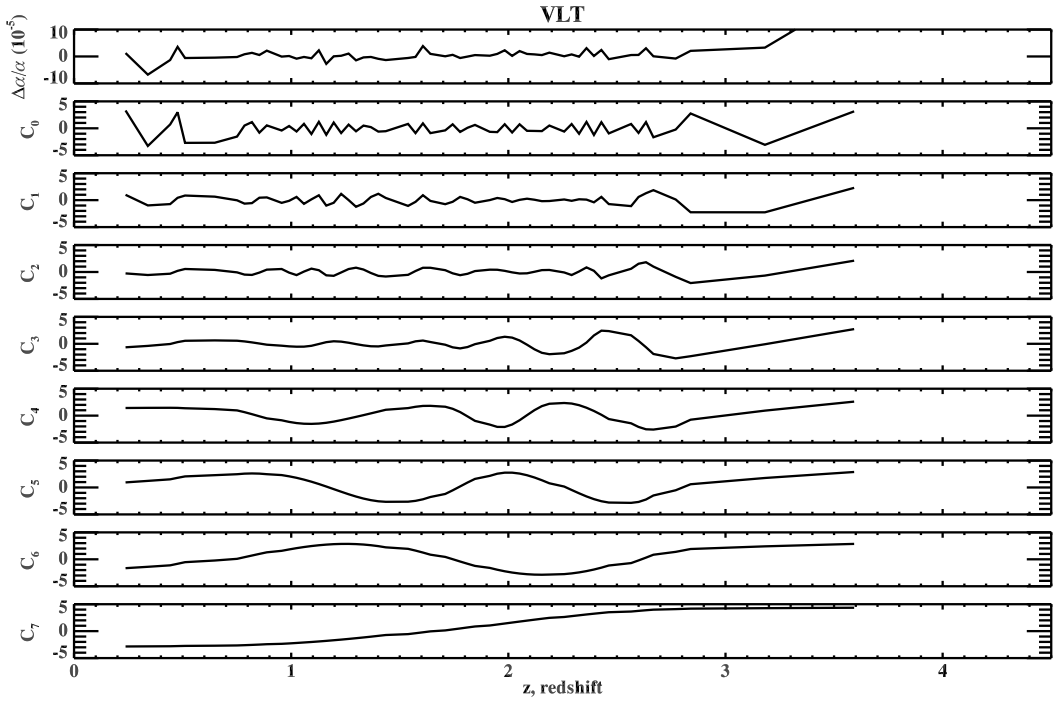

FIGURE 3.4: IMFs obtained from VLT/UVES dataset.

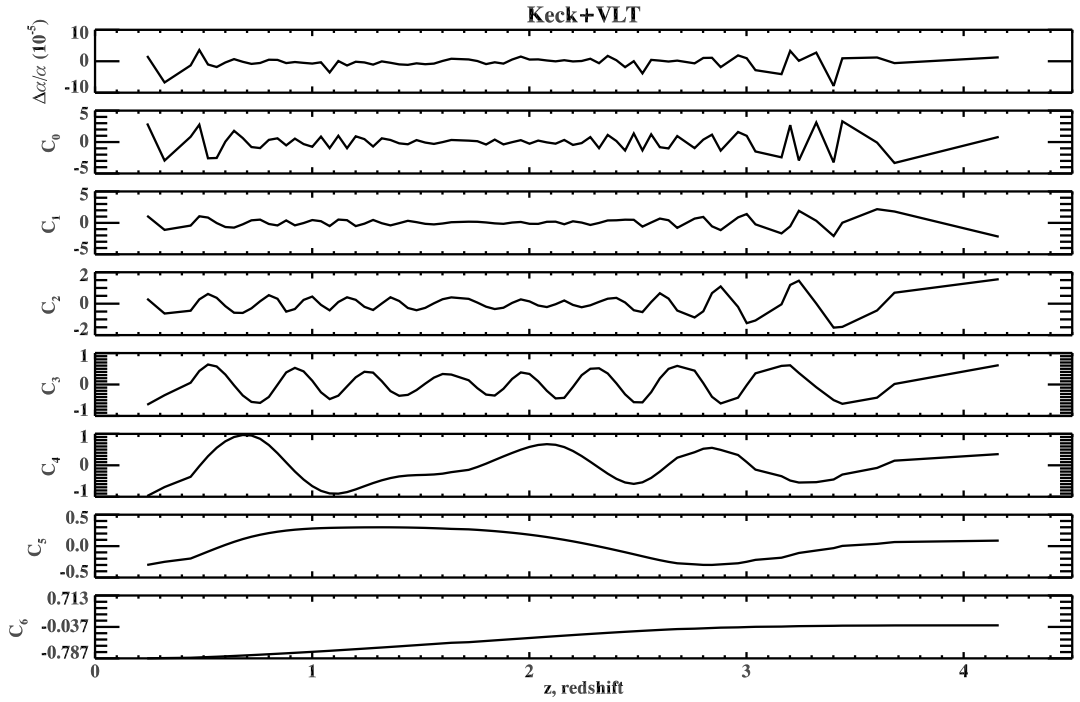

FIGURE 3.5: IMFs obtained from sample of combined Keck and VLT data.

The significance of the IMFs has been evaluated through the Wu-Huang test [111] (see Fig. 3.6). The result of the test give for the two Keck IMFs C_5 and C_6 a significance at 90% CL, while the significance for the C_5 and C_6 VLT modes is higher resulting in a 99% CL

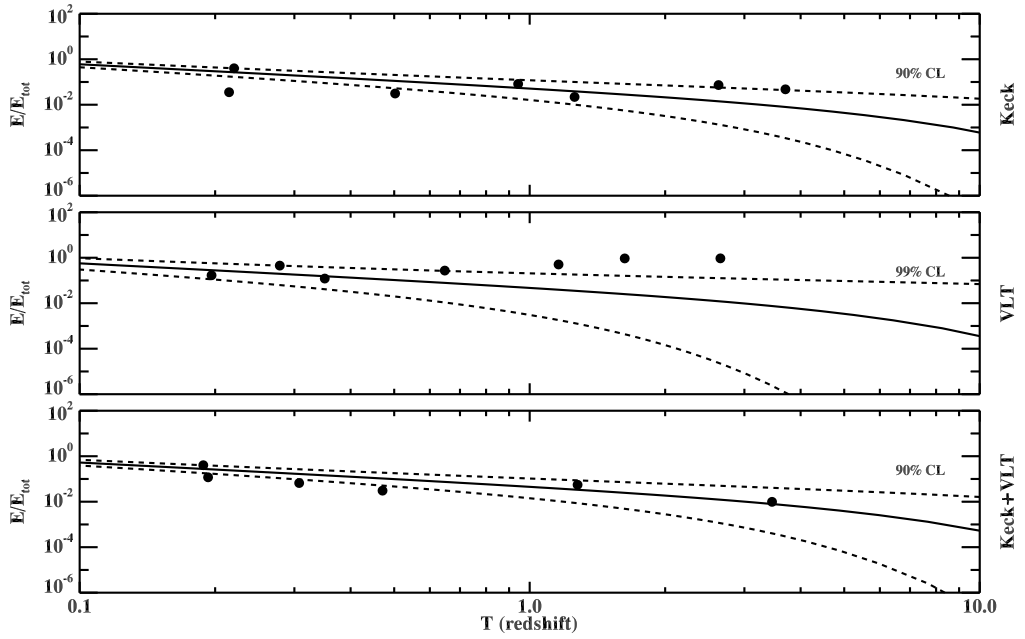

FIGURE 3.6: Wu-Huang significance test for IMFs extracted from $\Delta\alpha/\alpha$ datasets.

of significance. This results suggest a more complicated spatio-temporal pattern for the $\Delta\alpha/\alpha$ respect to the dipolar distribution observed by King *et al.*.

From the MonteCarlo EMD analysis carried on each sample and producing for each of them a set of 1000 realizations, we have obtained from VLT that 1432 IMFs have a characteristic period between 1.5 and 3.5 (in units of redshift). Of these 1432 IMFs, 473 have a period in the range [1.5, 1.8] in units of redshifts, while 959 IMFs have a period in the range [1.8, 3.5]. This significance is reduced in the analysis of Keck and combined samples, although for the combined sample a structure in the above mentioned range is still visible. The IMFs with periods included in the above mentioned range have been used, toghether with the trends, to reconstruct the time variations of alpha and its 68% Confidence Interval, and to compare the signals obtained from the different datasets. In fig. 3.8 the signals are shown as a function of fractional lookback time. The ΛCDM parameters used are: $H_0 = 70.5$ km s^{-1}, $\Omega_M = 0.2736$ and $\Omega_\Lambda = 0.726$ [112, 101] . The new signals obtained for both Keck and VLT show significant structures, in particular at higher redshifts. For the combined sample the oscillations are reduced in amplitude and the global signal show a general trend.

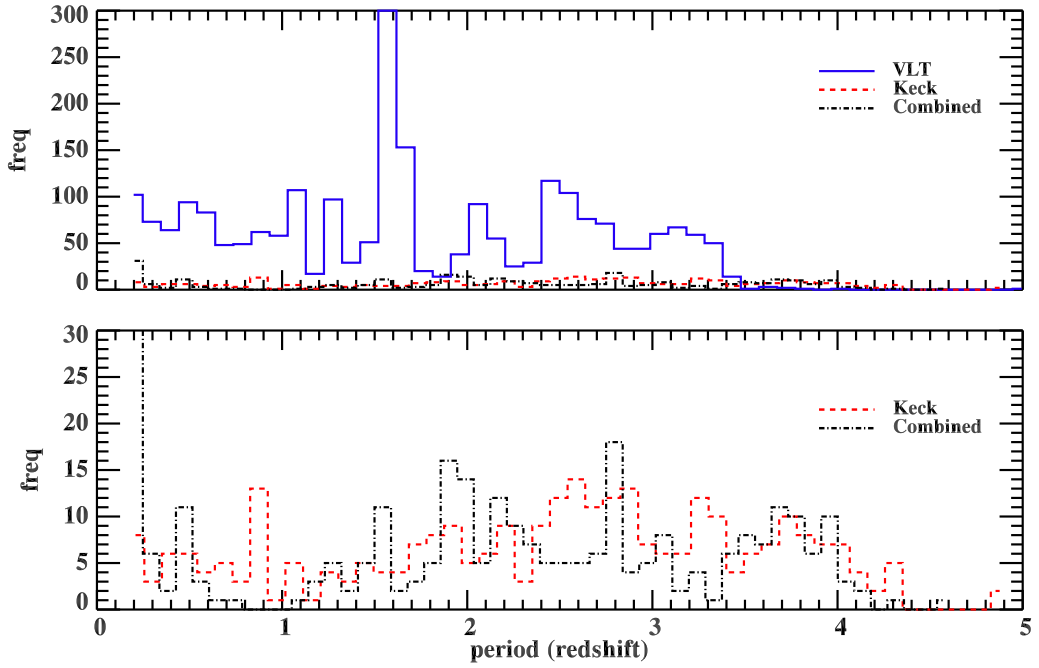

FIGURE 3.7: Histogram of VLT (blue solid line) Keck (red dashed line) and VLT+Keck IMF characteristic periods.

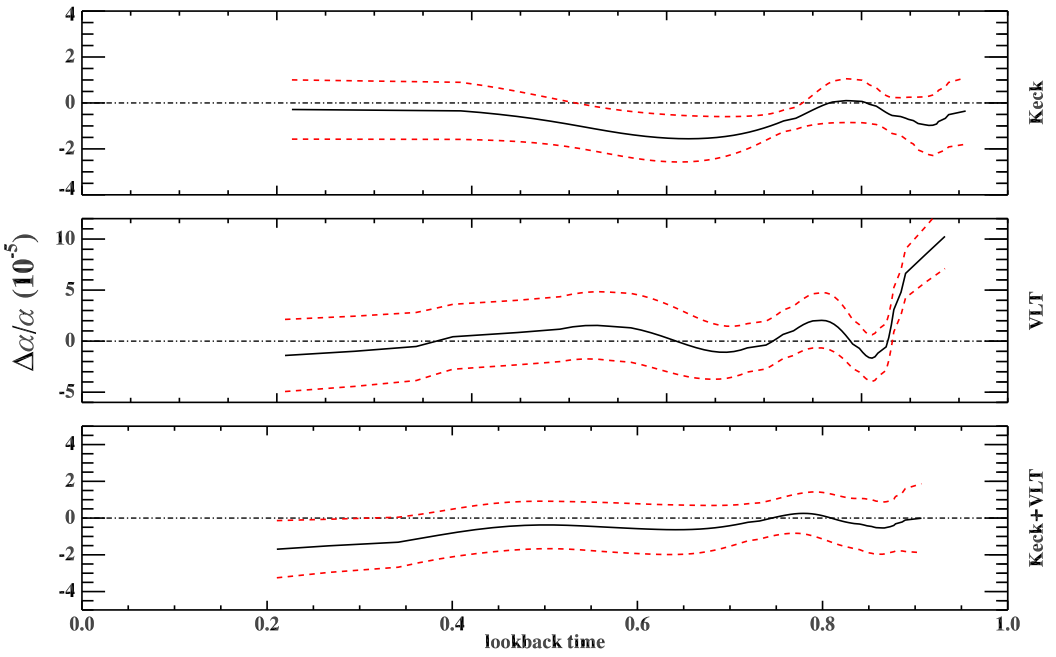

FIGURE 3.8: Time evolution of $\Delta\alpha/\alpha$ as seen from Keck, VLT and combining both datasets.

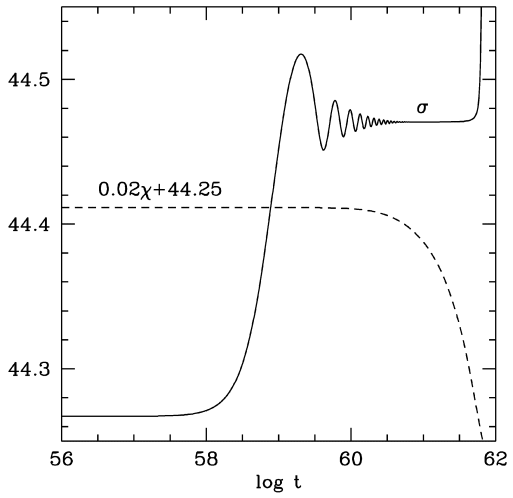

FIGURE 3.9: Time evolution of dilaton scalar field from [114].

3.3.1 Time Variations of $\Delta\alpha/\alpha$ as a Signature of a Dynamical Scalar Field?

The remarkable property of the oscillations as seen from the temporal variations reconstructed for Keck and VLT, is that the oscillations, particularly clear at higher z, seem to change their frequency in time. The feature may support the idea proposed by Fujii to describe the time variations of the fine-structure constant through the variations of the dilaton scalar field σ [113]. He noted that the Friedman solution with $k = 0$ of the cosmological equations in the two-scalar fields scenario for the dilaton field σ (which toghether with another scalar field χ describes the dark energy content in a scenario of the simplest scalar-tensor theory) shows regions of plateau, where the values of σ and χ are constant, with subsequent small transitions, acting as "mini-inflations", during which σ exhibits damped oscillations in the regions close to the actual age of the universe (the evolution described in time coordinate choosen as $\log(t/\tau_P)$, with τ_P the Planck time unit). We note that these oscilations results in a time-varying frequency in the redshift. Subsequentely he proposed to fit the Keck data by means of a phenomenological model of a damped oscillator, thus obtaining that, even if the resulting χ^2 variable was comparable with the weighted mean fit, his model has the characteristic to take into account of the zero value for $\Delta\alpha/\alpha$ in the present epoch.

Our results seem to mark a further step in this direction, since the signals we have obtained are obtained from the data, thus without supposing any *a priori* model. In Fig. 3.10 we report the signals shown in Fig 3.8 with the time scale converted to the$\log(t/\tau_P)$ coordinate.

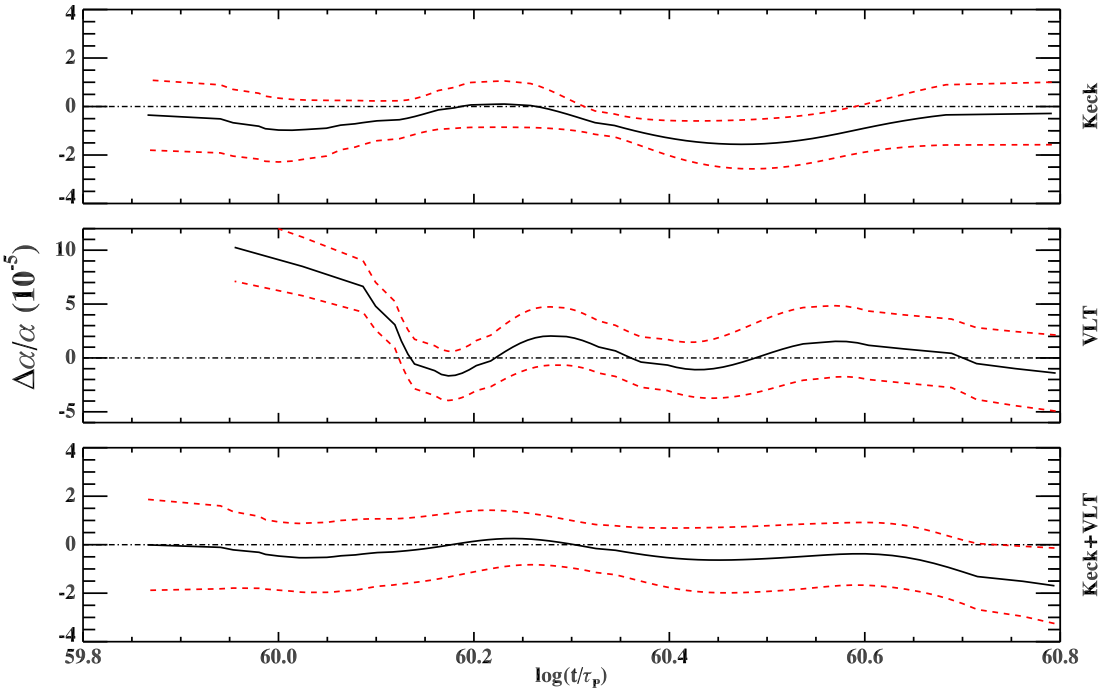

FIGURE 3.10: Same as in Fig. 3.8 but as function of age of universe normalized to Plack time unit.

In this new coordinate the oscillations of VLT and Keck look more "regular", thus confirming in a certain sense that the model fit proposed by Fujii may represent a usefull way to investigate the temporal evolution (and possibly also the spatially distribution) of the fine-structure constant.

Appendix A

Error Propagation Study in the EMD Analysis and its application to OPERA Data Analysis

In Sec. 2.4 we have shown the results of EMD analysis carried on cosmic muon data. By means of a Monte Carlo simulation, a 68% confidence interval has been obtained both for cosmic muon flux and sunspot number 11-yr signals. The regions of confidence for the signals were used then to estimate the Pearson's correlation coefficient and the corresponding 95% CL. In this section we will describe in details the improvements on the EMD method which allow the study of error propagation in the IMFs extracted from a time series. In the next section we will apply the new analysis tool to the study of proton and neutrino waveforms used in the recent analysis for the neutrino velocity measurement in the OPERA experiment [115].

A.1 The Empirical Mode Decomposition

The Empirical Mode Decomposition (EMD) method is a technique developed to process nonstationary data [116] and successfully applied in different contexts, e.g. [117, 118]. It is able to isolate from a given signal the periodicities and their relative amplitudes in an adaptive way, i.e. no basis of functions, respect to which the signal has to be decomposed, have to been established *a priori*. In the EMD framework, a time series $X(t)$ is decomposed into a finite number of oscillating Intrinsic Mode Functions (IMF) as

$$X(t) = \sum_{j=0}^{m-1} C_j(t) + r_m(t) \tag{A.1}$$

The IMFs $C_j(t)$ represent a set of basis functions obtained from the dataset under analysis by following the "sifting" procedure described by Huang *et al.* [116]. This procedure starts by identifying local minima and local maxima of the raw signal X(t). The envelopes of maxima and minima are then obtained through cubic splines and the mean between them, namely $m_1(t)$, is calculated. The differences between the raw time series and the mean series $h_1(t) = X(t) - m_1(t)$, represents an IMF only if it satisfies two criteria: 1) the number of extremes and zero crossings does not differ by more than one; 2) at any point, the mean value of the envelopes defined by the local maxima and the local minima is zero. Although h_1 seems to satisfie the required properties, in the sifting properties some new extrema can be generated as well as old ones can be exaggerated. In order to obtain a more symmetric signal, the sifting process has to be repeated. The two commonly used parameters used to stop the sifting algorithm are the Cauchy type criterion, according to which the sifting process is stopped when the parameter

$$SD = \sum_{t=0}^{T} \left[\frac{\left| h_{1(k-1)}(t) - h_{1k}(t) \right|}{h^2_{1(k-1)}(t)} \right]$$

is smaller than a fixed value (typically between 0.2 and 0.3) [116], and the s number defined as the number of consecutive times the two criteria for an IMF have to been satisfied. Typical values for the SD parameters are $0.2 - 0.3$, while for s number are racommanded values between 4 and 8 [119].[1]

The significance of the IMFs extracted can be tested by means of the Wu-Huang test [111], where the energy content of the mode $E_j \propto \sum_i C_j^2(t_i)$ with characteristic period $\bar{T}_j$ is compared with that expected in the case of IMF extracted from a white noise signal. In this case, for the j-th IMF, the energy is a variable which follows a χ-squared like distribution, with mean $\bar{E}_j \propto 1/\bar{T}_j$ and degrees of freedom (dof) $N\bar{E}_j$, where N is the total number of data points.

A.2 Monte Carlo Simulation in the EMD Analysis

In this section we will describe a Monte Carlo based alghoritm developed during our doctoral work, through which the IMFs and their corresponding 1σ confidence interval are built, starting from an ensemble of simulated different realizations of the original signal. The different steps of the alghoritm can be summirized as follows:

1. Starting from a given time series, an ensemble of N realizations of the signal is produced by taking, for each data point, N random numbers normally distributed, with mean value and standard deviation equals to the central value and the error

[1] Throughout our work we have adopted SD parameter as sifting stopping criterion. The SD_{max} value used is 0.2, unless otherwise specified.

associated to the data point, respectively. In principle the error associated to the point can be asymmetric.

2. Each realization is decomposed into its IMFs and only the IMFs which have a significance according to the Wu-Huang test higher than an *a priori* fixed value, e.g. 99% CL, are retained. The trends extracted from the N realizations are used instead to build the averaged trend of the signal and the corresponding standard deviation.

3. For each significant IMF the mean period, defined as $\bar{T} = 2\pi/\bar{\omega}$, with $\bar{\omega}$ the average of instantaneous frequency taken over the whole time window, is calculated and an histogram of the mean periods is derived.

4. All the IMFs with mean period included in a range $[T_{min}, T_{max}]$ are used to build the averaged IMF on the time scale of interest, toghether with its corresponding standard deviation.

We have tested for the first time the new algorithm for the study of proton and neutrino distribution used at OPERA experiment for the measurement of neutrino velocity [120]. After a brief summary of the experiment, in the next section will be presented the results of the EMD analysis that we have carried on proton and neutrino distributions.

A.3 EMD Analysis of Proton and Neutrino Distributions from the OPERA Experiment for the Neutrino Velocity Measurement

The OPERA neutrino detector is located at the underground Gran Sasso Laboratory (LNGS). It is dedicated to observation of $\nu_\mu \to \nu_\tau$ oscillations through the detection of τ^- lepton produced for charged current (CC) (see [120] and references therein). Furthermore through the detector it is possible to determine the neutrino velocity by measuring the time of flight (TOF_ν) of neutrinos produced in dedicated beams at CERN (CNGS beams) with a precision at level of ns. Here we breafly resume the characteristic of the experiment to measure neutrino velocity as described in [120].
The first measurement of neutrino velocity was performed using data taken during 2009, 2010 and 2011. In the first phase of the experiment a beam of protons accelerated at 400 GeV/c with the CERN Super Proton Synchrotron (SPS) is focused on a graphite target. The exposition to the proton beam lasts 10.5 μs. For each year are considered two proton extractions separated by an interval of 50 ms. Charged mesons produced in the collision are directed to a 1 km long tunnel where they decay in muons and neutrinos. Neutrinos produced in the decay have mean energy of 17 GeV. After travelling for 730 km (i.e. the distance between CERN and LNGS) the neutrinos are revealed in the OPERA

detector. The distribution of CERN to Gran Sasso (CNGS) neutrino beam is reconstructed at OPERA detector and is compared with the proton beam waveform. The distance between the proton beam extraction point and the origin of the OPERA reference frame is $d_{CERN-OPERA} = (731278.0 \pm 0.2)$ m.

In order to measure the TOF$_\nu$ it is important to create a permanent time link between CERN and OPERA. This is obtained with two identical systems installed at CERN and at LNGS and composed by a Septentrio PolaRx2e GPS receiver operating in "common view" with the receiver installed in the other facility and a Cs4000 clock which provide the reference frequency for the PolaRx2e.

Three delays for the CERN timing chain have to be taken in account:

1. The delay from the PolaRx2e 1 Pulse Per Second (1 PPS) to the Control Timing Receiver (CTRI) module used to tag the time-stamp the kicker magnet trigger-signal $\Delta t_{UTC} = (10085 \pm 2)$ ns;

2. The delay to produce the replica of the signal from the CTRI to the digitisation of the Wave Form Digitizer $\Delta t_{trigger} = (30 \pm 1)$ ns;

3. The delay for the signal tagging the proton arrive to the BCT, to the WFD $\Delta t_{BCT} = (580 \pm 5)$ ns.

TOF$_\nu$ is measured with respect to the BCT waveform which is tagged w.r.t. the UTC.

At OPERA detector the UTC time source is provided by a GPS system ESAT 2000 which 1PPS output is logged with a CTRI with respect to the PolaRx2e installed at LNGS providing the time link with CERN.

The delay of the transmission of the ESAT 1 PPS signal to the OPERA Master Clock is measured through a 8.3 km optical fibre through the two way method, which consist to compare the delay for a signal to travel along a path A with the time required for a signal to travel along another fibre B. The same signal is then sent from the origin and come back travelling along both the fibres. By the comparison of the difference between the delays $(t_B - t_A)$ and the total interval used to travel along both the fibres $(t_A + t_B)$ is then derived t_A. The delay measured in 2006 gives the value (40996 ± 1)ns.

Other two delays have to been considered due to the sum of the delays from the moment the photons produced in the detector reach the photocatode to the time-stamp of the signal and the internal delay of the Field Programmable Gate array which send the Master Clock signal to the frontend cards (FPGA latency) which are equals to 59.6 ns and 24.5 ns respectively.

Finally a maximum likelihood procedure is carried to measure the time lag between the proton waveform and the neutrino distribution.

The previous results of 2011 given a difference of TOF$_c$-TOF$_\nu$$\sim$61 ns which induced to the conclusion of superluminal neutrinos [115]. Further checks allowed to relate this difference

to a not properly connected cable for the measure of the GPS 1 PPS output transmission to the Master Clock, which induced a slower response of the optical/electrical converter of the Master Clock [120]. This delay was equals to 73.2 ns.
A second method to measure neutrino velocity consisted to use short bunches wide-spaced proton beams [121, 122]. This method results in a less statistics accumulated in the neutrino distribution reconstruction but, at the same time, it allows to associate unambiguously neutrino event to the corresponding proton bunch. The results obtained by using CNGS bunched beams lasted from October 22 to November 6, 2011 with four bunches of about 3 ns long (FWHM) separated by 524 ns where consistent with the hypotesis of subluminal neutrinos.
The measure repeated using runs between the 10th and 24th of May in 2012 with extractions composed of 4 batches of 16 proton bunches (100 ns distance between two consecutive bunches and 300 ns distance between 2 consecutive batches) and after some improvements in the timing system, the final 90% CI for neutrino velocity has been estimated:

$$-1.8 \cdot 10^{-6} < \frac{v_\nu - c}{c} < 2.3 \cdot 10^{-6}$$

An estimation for antineutrino velocity has been estimated too with the 90% CI corresponding to

$$-1.6 \cdot 10^{-6} < \frac{v_{\bar{\nu}} - c}{c} < 3.0 \cdot 10^{-6}$$

again consistent with subluminal neutrino hypotesis and according to other measurements carried in other detectors on LNGS beam [123, 124, 125].
In the next section we will analyse proton and neutrino distribution for both extraction used in the 2009÷2011 data analysis, in order to study how the proton waveform time variations are observed in the final neutrino distribution.

A.3.1 EMD Analysis of Proton and Neutrino Waveforms

The data corresponding to the proton and neutrino distributions for the first and second extractions are taken from the images of Fig. 16 of [120], which are reproduced here in Fig. A.1.
The error for each data point due to the extraction of the data from the images are of 33 ns and of 0.4 Event/bin for the time and count variables respectively. The EMD analysis has been carried following the steps of the alghoritm described in Sec A.2 with $N = 1000$ simulated realizations for each proton and neutrino distribution. For each extraction, the periodogram derived from the mean periods of the IMFs extracted from neutrino data which have significance of 99% CL, according to Wu-Huang test, is compared with that corresponding to IMFs extracted from proton data, the latter binned with 150 ns of bin

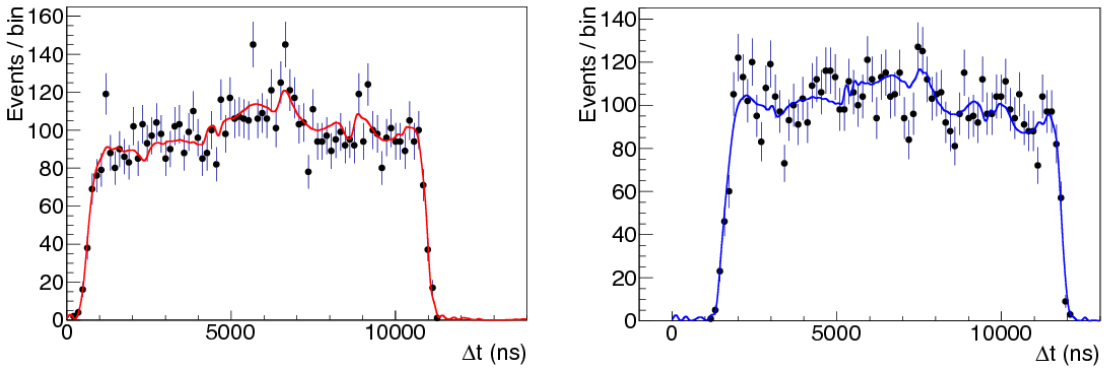

FIGURE A.1: Proton beam distribution from first (left panel, red line) and second (right panel, blue line) extraction are compared with the corresponding neutrino distributions as detected at the OPERA detector. Images taken from [120] (Fig. 16).

width in order to make comparable the time scales of neutrino and proton distributions. The periodograms are shown in Fig. A.2. We can see that the IMFs extracted from neutrino data have periods comparable with that extracted from the protons, except for the largest period distribution which for neutrino data have a maximum at 6000 ns, while for protons have a maximum at 7000 ns. From the periods distributions we have built the new IMFs both for neutrino and for proton data. In particular, for each dataset we have built three IMFs, denoted C_{low}, C_{hi} and C_n: C_{low} has been derived from the lowest modes, with periods in the range $\bar{T} \in [5.5, 7.5] \cdot 10^3$ ns, C_{hi} has been derived from the highest frequency modes and which periods lie in the range $\bar{T} \in [3.5, 4.5] \cdot 10^3$ ns. The modes with periods lower than 3000 ns have been grouped in a single mode denoted C_n, since those are expected to be significantly affected by noise and no relevant structures are expected. The resulting IMFs and the mean trend extracted from neutrino and proton data are compared in Fig. A.3. For neutrino signals the 1σ confidence region is colored in cyan, while for the proton signals, the 1σ confidence region bound are marked with dashed line. The trend and IMFs of neutrinos have been compared with the corresponding obtained from proton data through a correlation test. In this test 10000 realizations of couples of neutrino and proton signals have been obtained through a Monte Carlo simulation analogous to that used to extract the ensemble of IMFs and for each couple, the Pearson's correlation coefficient r have been calculated. In Fig. A.4 are shown the histograms of r variable.

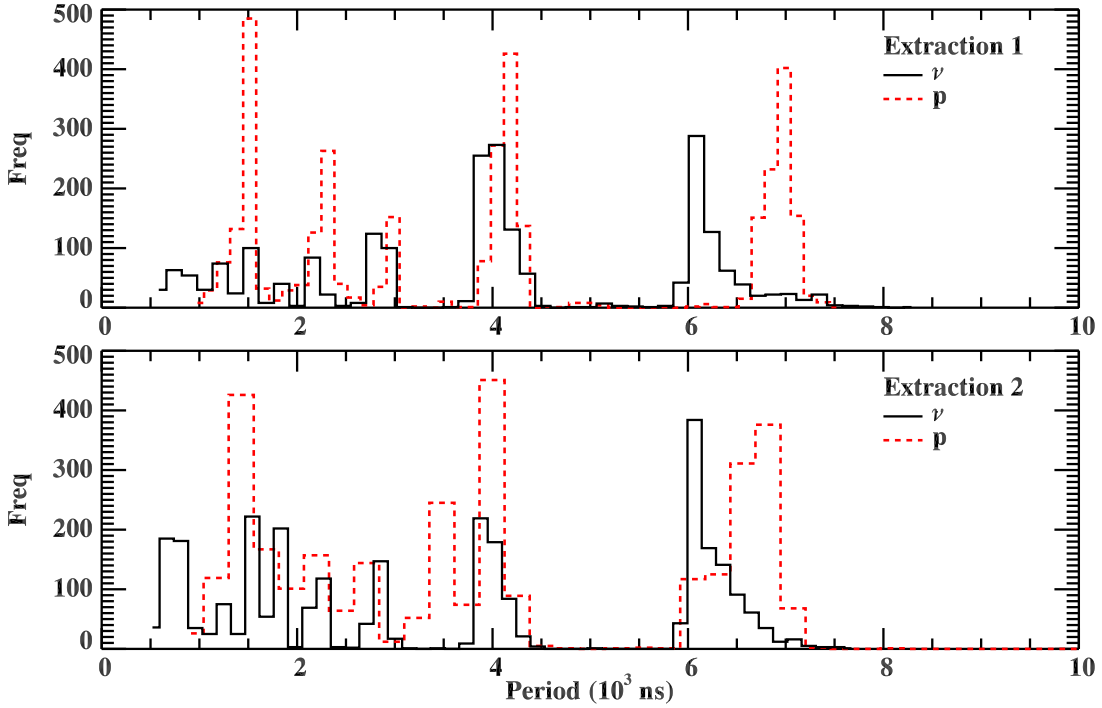

FIGURE A.2: For each extraction are reported the periodogram of characteristic IMF periods for both neutrino (black) and proton (red) data. Proton data have been binned with 150 ns bin width.

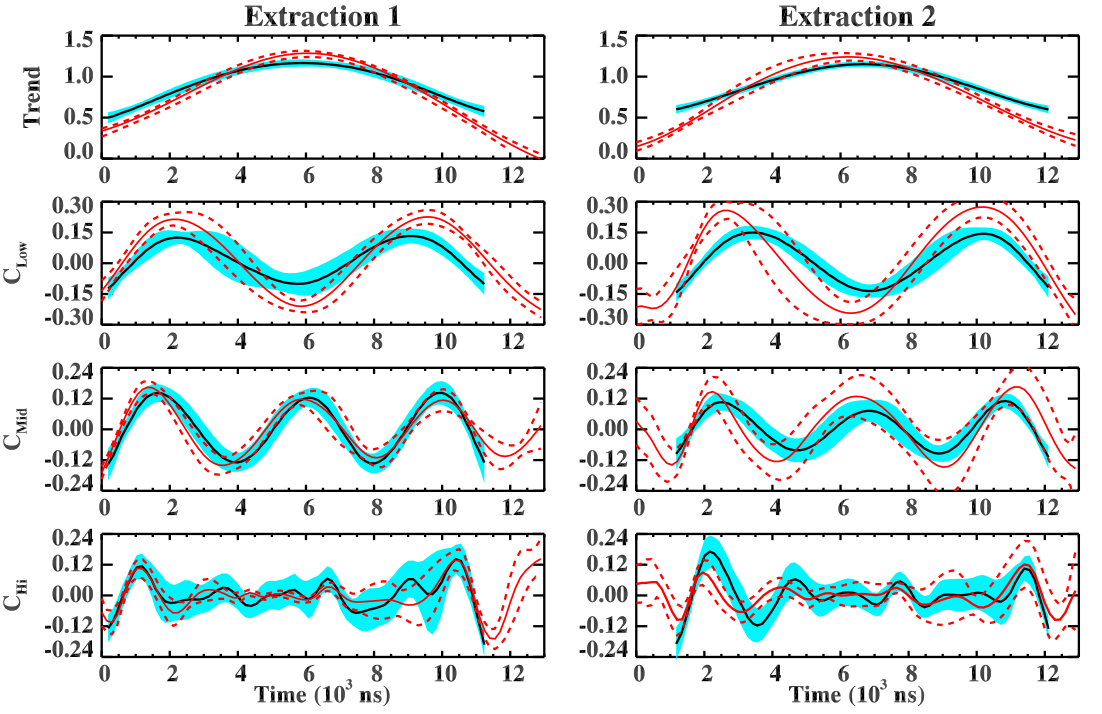

FIGURE A.3: For each extraction are shown, from to to bottom, the trend and the C_{low}, C_{hi} and C_n IMFs, with the corresponding 1σ CI, extracted both for neutrino and for proton distribution data.

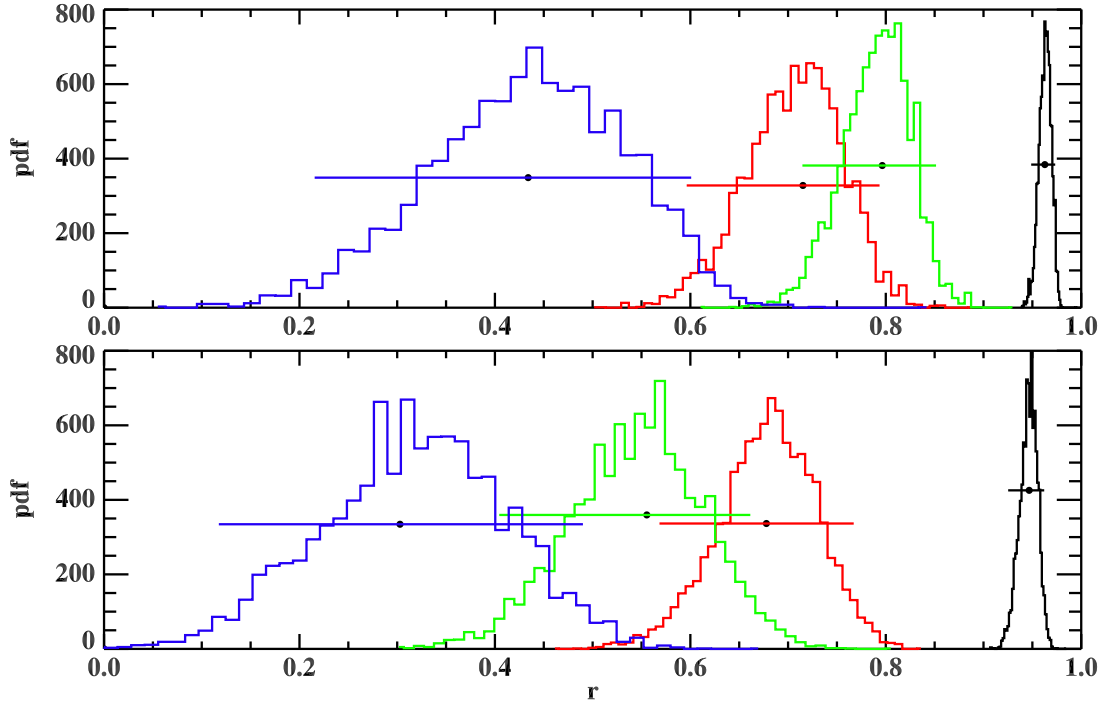

FIGURE A.4: Histograms of Pearson's correlation coefficient obtained by evaluating the correlation coefficient for 1000 realizations of couples of neutrino and proton signals. In particular black histograms are obtained by comparing neutrino and proton trends, red histograms correspond to comparison between neutrino and proton C_{low}, green histograms are obtained from C_{hi} modes comparison and blue histograms are relative to C_n modes.

A.3.2 Discussions

Through the Monte Carlo alghorithm applied to the EMD technique, from proton and neutrino distributions for first and second extractions of CNGS beams, we have extracted the significant IMFs toghether with the trends. In particular we have obtained from neutrino distributions two IMFs which strongly correlate with the corresponding IMFs extracted from proton distributions. However the IMF obtained from the low-frequency modes of neutrino dataset exhibits a modulation with characteristic period lower than the corresponding obtained from proton dataset. On the other hand the trend of neutrino distribution looks flatter, thus indicating that the main contribution in the amplitude of neutrino signal is in the trend, thus revealing a small distorsion in neutrino distribution.

Appendix B

Helioseismic Instabilities Induced by Time-Dependent Background Magnetic Fields

In Sec. 1.5.3 we have considered a phenomenological model to interpret the quasi-biennial modulation of neutrino flux as induced by a background magnetic field which varies slowly in time. Furthermore new features arise from magneto-gravity theory when a more complex time dependence is assumed for the background magnetic field. In this appendix we will show the results of the model which we have developed during this doctoral work, of magneto-gravity waves in presence of a time-dependent background magnetic field characterized by a low-pass bandwidth.

B.1 MHD Equations with a time-dependent Background Magnetic Field

We start our analysis from the basic set of MHD equations and the supplementary assumptions used for Magneto-Gravity Waves theory presented by [67]. The MHD equations considered are

- Continuity equation for mass density

$$\frac{d}{dt}\rho + \rho u = 0 \tag{B.1}$$

- Energy conservation

$$\frac{d}{dt}P - \gamma\frac{P}{\rho}\frac{d}{dt}\rho = -\left(\gamma - 1\right)Q \tag{B.2}$$

- Momentum equation

$$\rho \frac{d}{dt}\mathbf{v} = -\nabla P + \rho \mathbf{g} + \frac{1}{4\pi}\left[(\nabla \times \mathbf{B}) \times \mathbf{B}\right] \tag{B.3}$$

- Faraday's equation

$$\frac{\partial}{\partial t}\mathbf{B} = \nabla \times (\mathbf{v} \times \mathbf{B}) \tag{B.4}$$

In Eq. (B.1), $u \equiv \nabla \cdot \mathbf{v}$. In order to simplify the problem, we neglect the dissipative terms which appear in the velocity and magnetic field equations. The set of equations is completed by the supplementary equations for the divergence of magnetic field

$$\nabla \cdot \mathbf{B} = 0 \tag{B.5}$$

and the gravitational field equation

$$\nabla \cdot \mathbf{g} = 4\pi G\rho \tag{B.6}$$

The equations are symplified if we adopt the following assumptions

(i) An equilibrium situation is assumed where the velocity field and current density are both zero.

(ii) We neglect energy sources and losses ($Q = 0$).

(iii) We adopt low-frequency approximation, in order to filter out the pressure p-modes.

Furthermore we assume a rectangular geometry with z-axis correnspounding to the radius-direction and we consider a background density profile which decay exponentially following the law $\rho_0 = \rho_c \exp(-z/H)$, with H the pressure height scale (equals to $0.095\, R_{sun}$).
We will assume a constant gravitational field, i.e. $\mathbf{g} = -g\mathbf{e}_z$. This assumption is valid if we focus our analysis on the radiative zone, where the density scale is smaller than temperature and gravity scales, as shown in the solar models [1, 126, 127].

B.2 Linearization

The analysis of magneto-gravity waves starts by splitting each variable into background and fluctuating quantities. Background quatities are assumed constant in time and uniform, except for magnetic field which we assume having a time dipendence, with a bandwidth centered at zero and with a cut-off frequency which is smaller than the frequencies which compose helioseismic spectrum ($\omega_c \ll \{\omega_a\}$, with $\{\omega_a\}$ denoting the whole set of helioseismic modes). We are in fact interested on the effects induced on magneto-gravity modes by

the presence of a time-dependent background magnetic field originated, e.g. by dynamo mechanisms. The equations for the fluctuating quantities can be written as follows

$$\begin{cases} \partial_t \rho' - \frac{v_z}{H}\rho_0 + \rho_0 u = 0 \\ \partial_t P' - \frac{v_z}{H} P_0 + \gamma P_0 u = 0 \\ \partial_t \mathbf{B}_0 + \partial_t \mathbf{B}' = -u\mathbf{B}_0 + \mathbf{B}_0 \cdot \nabla \mathbf{v} \\ \rho_0 \partial_t \mathbf{v} = -\nabla P' - \rho' g \mathbf{e}_z + \rho_0 v_A^2 \left[\mathbf{f} \cdot \nabla \mathbf{b} - \nabla \left(\mathbf{f} \cdot \mathbf{b}\right)\right] \end{cases} \tag{B.7}$$

where $\mathbf{B}_0 = B_0 f\left(t\right) \mathbf{e}_x$ and $\mathbf{b} \equiv \mathbf{B}'/B_0$.
In order to find out the eigenfrequency spectrum of the system, each variable is decomposed into its Fourier components along x- and y- direction and in frequency space. In particular we assume the following convention

$$\mathbf{A}\left(t\right) = \frac{1}{\sqrt{2\pi}} \int_{-\infty}^{+\infty} d\omega_\alpha \mathbf{A}\left(\omega_\alpha\right) e^{-i\omega_\alpha t}$$

where with $\mathbf{A}\left(t\right)$ we denote the components in real space, i.e. $\mathbf{A}\left(t\right) = \mathbf{A}\left(x, y, z, t\right)$, while $\mathbf{A}\left(\omega_\alpha\right)$ represents the components in the reciprocal space, i.e. $\mathbf{A}\left(\omega_\alpha\right) = \mathbf{A}\left(k_x, k_y, z, \omega_\alpha\right)$. The Inverse Fourier transform from frequency to time domain is defined as

$$\mathbf{A}\left(\omega_\alpha\right) = \frac{1}{\sqrt{2\pi}} \int_{-\infty}^{+\infty} dt \mathbf{A}\left(t\right) e^{+i\omega_\alpha t}$$

The expression for background magnetic field assumes the form

$$\mathbf{B}_0\left(t\right) = B_0 \frac{1}{\sqrt{2\pi}} \int_{-\omega_c}^{+\omega_c} d\omega_\alpha f\left(\omega_\alpha\right) e^{-i\omega_\alpha t} \mathbf{e}_x$$

here B_0 may denote the mean value of background magnetic field. This imply that for $f\left(0\right)$ we can assume a delta function $\delta\left(0\right)$.
The equations for density and pressure become

$$\begin{cases} \rho' = -\frac{1}{i\omega}\left[\frac{v_z}{H}\rho_0 - \rho_0 u\right] \\ P' = -\frac{1}{i\omega}\left[\frac{v_z}{H} P_0 - \gamma P_0 u\right] \end{cases} \tag{B.8}$$

This couple of equations have the same form as the corresponding equations found in Ref. [67], as we expect from the linearity of the equations for mass density and pressure. Non-linear effects arise for velocity and magnetic induction equations, i.e. where the interaction of those fields are coupled with background magnetic field. Let we consider Faraday equation. In the frequency space it behaves as follows

$$
\begin{aligned}
-i\omega_\mu\left(\mathbf{f}_\mu+\mathbf{b}_\mu\right)= \quad & \tfrac{1}{\sqrt{2\pi}}\int_{-\infty}^{+\infty}dt\,e^{i\omega_\mu t}\tfrac{1}{2\pi}\int_{-\infty}^{+\infty}d\omega_\beta\int_{-\omega_c}^{+\omega_c}d\omega_\gamma \\
& \cdot\left(-u_\beta f_\gamma+\mathbf{f}_\gamma\cdot\nabla\mathbf{v}_\beta\right)e^{-i\left(\omega_\beta+\omega_\gamma\right)t}
\end{aligned}
\tag{B.9}
$$

By interchanging order of integration and integrating over time variable the exponential functions, we obtain a delta function $\delta\left[\omega_\mu-\left(\omega_\beta+\omega_\gamma\right)\right]$ which we can use to integrate over ω_β variable and the Faraday equation becomes

$$
-i\omega_\mu\left(\mathbf{f}_\mu+\mathbf{b}_\mu\right)=\frac{1}{\sqrt{2\pi}}\int_{-\omega_c}^{+\omega_c}d\omega_\gamma f_\gamma\left(-u_{\mu-\gamma}\mathbf{e}_x+\partial_x\mathbf{v}\right) \tag{B.10}
$$

Because of the structure assumed for background magnetic field, we can neglect $\mathbf{f}_\mu$. Furthermore the terms which appear in the form $A_{\mu-\gamma}$ can be developed in Taylor series around ω_μ

$$
\mathbf{A}_{\mu-\gamma}\equiv\mathbf{A}\left(\omega_\mu-\omega_\gamma\right)\simeq\mathbf{A}\left(\omega_\mu\right)-\omega_\gamma\partial_\mu\mathbf{A}\left(\omega_\mu\right)+O\left(\omega_\gamma^2\right) \tag{B.11}
$$

where $\partial_\mu\equiv\partial_{\omega_\mu}$.
The equations for x- and z- components of $\mathbf{b}_\mu$ become[1]

$$
\begin{cases}
-i\omega_\mu b_{x,\mu}=\hat{O}_\gamma f_\gamma\left(1-\omega_\gamma\partial_\mu\right)\left(-u_\mu+ik_x v_{x,\mu}\right) \\
-i\omega_\mu b_{z,\mu}=ik_x\hat{O}_\gamma f_\gamma\left(1-\omega_\gamma\partial_\mu\right)v_{z,\mu}
\end{cases}
\tag{B.12}
$$

where for simplicity we have introduced the operator $\hat{O}_\gamma\equiv 1/\sqrt{2\pi}\int_{-\omega_c}^{\omega_c}d\omega_\gamma$. Taking into account the above rules to approximate convolution products, the equations for x- and z-components of velocity vector become

$$
\begin{cases}
-\omega_\mu^2 v_{x,\mu}=ik_x\left(c_s^2u_\mu-gv_{z,\mu}\right) \\
-\omega_\mu^2 v_{z,\mu}= \quad -g\partial_z v_{z,\mu}-\left(\gamma-1\right)gu_\mu+c_s^2\partial_z u_\mu \\
\qquad\qquad +i\omega_\mu v_A^2\hat{O}_\gamma f_\gamma\left(1-\omega_\gamma\partial_\mu\right)\left(\partial_z b_{x,\mu}-ik_x b_{z,\mu}\right)
\end{cases}
\tag{B.13}
$$

It is more convenient to focus on the equation for $v_{z,\mu}$. All the other quantities can be derived from it. After some algebraic manipulation, the master equation for v_z can be written as follows

$$
\begin{aligned}
&\partial_z^2 v_{z,\mu}-\tfrac{N^2}{g}\partial_z v_{z,\mu}+k_\perp^2\left(-1+\tfrac{N^2}{\omega_\mu^2}\right)v_{z,\mu}=\tfrac{k_\perp^2 v_A^2}{\omega_\mu^2} \\
&\cdot\hat{O}_\gamma f_\gamma\hat{O}_{\gamma'}f_{\gamma'}\left(1-\omega_\gamma\partial_\mu\right)\left(1-\omega_{\gamma'}\partial_\mu\right)\left(-k_\perp^2+\partial_z^2\right)v_{z,\mu}
\end{aligned}
\tag{B.14}
$$

[1]The y- component of perturbations and wave vector can be set equal to zero.

where $k_\perp = k_x$. Introducing the variable $\xi \equiv k_\perp^2 v_A^2/\omega^2 e^{-z/H}$ and omitting terms of order $O\left[(\omega_\gamma/\omega_\mu)^2\right]$, eq. (B.14) becomes[2]

$$\begin{aligned} &4\theta\alpha\xi^4 \ddot{v} + \left[(1+12\theta)\,\alpha\xi - 1\right]\xi^2\ddot{v} \\ &+\left\{\left[1-4\left(K^2-1\right)\theta\right]\alpha\xi - \tfrac{1}{\gamma}\right\}\xi\dot{v} \\ &-K^2\left[\alpha\xi + \left(\kappa^2-1\right)\right]v = 0 \end{aligned} \tag{B.15}$$

where $\dot{v} \equiv dv/d\xi$, $\kappa \equiv N/\omega$ and where we have introduced the variables α and θ defined as

$$\alpha \equiv \frac{1}{2\pi}\left[\int_{-\omega_c}^{\omega_c} d\omega_\gamma f\left(\omega_\gamma\right)\right]^2 = \left[f\left(t=0\right)\right]^2 \tag{B.16}$$

and

$$\theta \equiv i\frac{\Delta\omega_\gamma}{\omega} \tag{B.17}$$

with

$$i\Delta\omega_\gamma \equiv \frac{\int_{-\omega_c}^{\omega_c} d\omega_\gamma f\left(\omega_\gamma\right)\omega_\gamma}{\int_{-\omega_c}^{\omega_c} d\omega_\gamma f\left(\omega_\gamma\right)} = i\frac{2\int_0^{\omega_c} d\omega_\gamma \Im\left[f\left(\omega_\gamma\right)\right]\omega_\gamma}{f\left(t=0\right)} \tag{B.18}$$

where $\Im\left(z\right)$ denotes the imaginary part of z. In defining the variables α and θ we have considered the reality condition for the background magnetic profile (i.e. $f\left(-\omega\right) = f^*\left(\omega\right)$). Eq. (B.15) reduces to Burgess equation in the limit $(\alpha, \theta) \to (1,\, 0)$. We search solutions of the form $v = \xi^\sigma Y$. Introducing this expression for v in Eq. (B.15) and using for σ the expression[3]

$$\sigma = \frac{1}{2}\left[\frac{\gamma-1}{\gamma} + \sqrt{\left(\frac{\gamma-1}{\gamma}\right) - 4K^2\left(\kappa^2-1\right)}\right] \simeq \frac{\gamma-1}{2\gamma} + i\frac{\beta}{2} \tag{B.19}$$

with $\beta \equiv 2KN/\omega \gg 1$ and $K \equiv k_\perp H$, we can rewrite the master equation in the form

$$\begin{aligned} &4\theta\alpha\xi^3\dddot{Y} + \left\{\left[1+12\left(\sigma+1\right)\theta\right]\alpha\xi - 1\right\}\xi\ddot{Y} \\ &+\left\{\left[\left(2\sigma+1\right) - 4\left(K^2 - 3\sigma^2 - 3\sigma - 1\right)\theta\right]\alpha\xi - 2\sigma - \tfrac{1}{\gamma}\right\}\dot{Y} \\ &-\left(K^2-\sigma^2\right)\left(1+4\sigma\theta\right)\alpha Y = 0 \end{aligned} \tag{B.20}$$

We note that the parameter σ is tha same as found in Ref. [67]. The general solution of this equation can be expressed in terms of Meijer-G functions [**?**, 128] as follows

$$v = \left(\frac{1}{4\theta\alpha}\right)^\sigma \sum_{q=1}^{3} C_q G_{23}^{12}\left(\begin{array}{c|ccc} \frac{1}{4\theta\alpha\xi} & a_1 & a_2 & \\ & b_q & b_{m+1} & b_{m+2} \end{array}\right) \tag{B.21}$$

where the $\{a_i\}$ and $\{b_i\}$ coefficients are defined as

[2] From this point we will omit μ subscript for helioseismic modes in order to simplify the notation.
[3] Here and throughout the work we will use the same notation used in Ref. [67].

$$\begin{cases} a_1 = 1-\sigma & a_2 = \frac{1}{\gamma}+\sigma \\ b_1 = K & b_2 = -K \qquad b_3 = \frac{1}{4\theta} \end{cases}$$

The coefficient C_2 can be set equal to zero, because it corresponds to the solution which grows as ξ^K. It is more convenient to pass from $(C_1,\, C_3)$ constants to the new couple of constants $(D_1,\, D_3)$ defined as

$$\begin{cases} \left(\frac{1}{4\theta\alpha}\right)^{\sigma} C_1 = D_1\, \Gamma\left(1-\frac{1}{4\theta}\right) \\ \left(\frac{1}{4\theta\alpha}\right)^{\sigma} C_3 = \frac{D_3}{\Gamma\left(\frac{1}{4\theta}\right)} \end{cases} \tag{B.22}$$

Through this choise it is easier to see how the solutions obtained behave in the limit of $\theta \to 0$. We have in fact that

$$\begin{cases} \lim\limits_{\substack{\frac{1}{4\theta}\to\infty \\ \alpha\to 1}} \Gamma\left(1-\frac{1}{4\theta}\right) G^{12}_{23}\left(\frac{1}{4\theta\alpha\xi}\middle| \begin{matrix} 1-\sigma & 1-\sigma* \\ K & -K \quad \frac{1}{4\theta} \end{matrix} \right) = G^{12}_{22}\left(-\frac{1}{\xi}\middle| \begin{matrix} 1-\sigma & 1-\sigma* \\ K & -K \end{matrix} \right) \\ \lim\limits_{\substack{\frac{1}{4\theta}\to\infty \\ \alpha\to 1}} \frac{1}{\Gamma\left(\frac{1}{4\theta}\right)} G^{12}_{23}\left(\frac{1}{4\theta\alpha\xi}\middle| \begin{matrix} 1-\sigma & 1-\sigma* \\ \frac{1}{4\theta} & -K \quad K \end{matrix} \right) = G^{02}_{23}\left(\frac{1}{\xi}\middle| \begin{matrix} 1-\sigma & 1-\sigma* \\ K & -K \end{matrix} \right) \end{cases} \tag{B.23}$$

Of the two asymptotic solutions, only the former coincides with that found by Burgess *et al.* so that we can set $D_3 = 0$.[4] The solution that we have obtained contains terms of order higher than $O(\theta)$. The solution which have terms of the correct order can be obtained using the integral definition of Mejier-G

$$G^{mn}_{pq}\left(z\middle| \begin{matrix} \mathbf{a} \\ \mathbf{b} \end{matrix} \right) = \frac{1}{2\pi i}\int_L ds\, z^{-s} \frac{\prod_{j=1}^{m}\Gamma(b_j+s)\prod_{j=1}^{n}\Gamma(1-a_j-s)}{\prod_{j=m+1}^{q}\Gamma(1-b_j-s)\prod_{j=n+1}^{p}\Gamma(a_j-s)} \tag{B.24}$$

For the properties of Mejier-G function and the definition of the path L see [129].
Taking into account the asymptotic form for Γ expressed in the form

$$\frac{\Gamma(z+a)}{\Gamma(z+b)} \sim z^{a-b}\left[1+\frac{1}{2}(a-b)(a+b-1)\frac{1}{z}+O\left(\frac{1}{z^2}\right)\right]$$

The final expression for the solution is

[4] We note that in principle there is no reason to descard the complete solution with both D_1 and D_3 different by zero, but the study of this solution is out of the aim of our analysis.

$$\begin{aligned}\frac{v}{D} = \; & G_{22}^{12}\left(\begin{array}{c|cc} -\frac{1}{\alpha\xi} & 1-\sigma & \frac{1}{\gamma}+\sigma \\ & K & -K \end{array} \right) \\ & +2\theta G_{33}^{13}\left(\begin{array}{c|ccc} -\frac{1}{\alpha\xi} & 1-\sigma & \frac{1}{\gamma}+\sigma & -1 \\ & K & -K & 1 \end{array} \right) \\ & = \left[1+2\theta\left(-\alpha\xi\right)^2\frac{\partial^2}{\partial(\alpha\xi)^2}\right] G_{22}^{12}\left(\begin{array}{c|cc} -\frac{1}{\alpha\xi} & 1-\sigma & \frac{1}{\gamma}+\sigma \\ & K & -K \end{array} \right)\end{aligned} \tag{B.25}$$

The dispersion relation is obtained using the boundary condition $v\left(z=0\right)=0$. In order to solve the equation, it is convenient to express Eq. (B.25) in terms of hypergeometric functions ${}_2F_1\left(\alpha,\beta;\gamma;1-\left(\alpha\xi_c\right)^{-1}\right)$ and, using the Watson asymptotic expansion of gaussian hypergeometric function [129, 130] respect to the parameter β (see Ref. [131] for more details), finally we obtain two branches of frequancy spectrum, depending on the sign of the variable d, defined through $\omega=\omega_r\left(1+id\right)$. In particular we have

- For $\text{sign}\left(d\right)=-1$

$$\begin{aligned}\chi = \; & \frac{\sqrt{\alpha}v_A}{4HN}\cosh\chi \\ & \left\{\left(2\pi n+\pi\frac{1+\gamma}{\gamma}-i\ln\left|\tan\frac{\pi}{\gamma}\right|\right)+\log\left[\frac{1+2i\theta K^2\left(1+\frac{a*}{K}\coth\chi+\frac{a*^2}{K^2}\coth^2\chi\right)}{1+2i\theta K^2\left(1-\frac{a*}{K}\coth\chi+\frac{a*^2}{K^2}\coth^2\chi\right)}\right]\right\}\end{aligned} \tag{B.26}$$

- For $\text{sign}\left(d\right)=1$

$$\left[1+2\theta K^2\right]\tanh^2\chi+2\theta K a^*\tanh\chi+2\theta a^{*2}=0 \tag{B.27}$$

where χ variable is related to ξ_c through the relation $\xi_c=\left(\cosh\chi\right)^{-2}$. The first branch corresponds to Burgess magnetogravity dispersion relation, a part from a corrective factor which is negligible in the range $\omega<N$. The second branch corresponds to instable modes. The spectrum for the second branch shows small dependence from B_0, so that we can omit its contribution in the Eq. (B.27) and an analytical expression can be given for frequency in the form

$$x=i\mu\left\{2\sqrt{\frac{1+\mu}{\mu}}\cosh\left[\frac{1}{3}\text{arccosh}\left(\frac{2\mu^2+3\mu+3}{2\sqrt{\mu\left(1+\mu\right)^3}}\right)-i\frac{\pi}{3}\right]-1\right\} \tag{B.28}$$

where x is the frequency normalized to N and $\mu\equiv 2K^2\Delta\omega_\gamma/N$. In the limit of high K values, the solution tends to an asymptotic value $\Re\left(x_{max}\right)=\sin\left(\pi/3\right)$ and $\Im\left(x_{max}\right)=\cos\left(\pi/3\right)$, with $\Re$ and $\Im$ respectively denoting real and imaginary part of the argument. We note that $\left|\omega_{max}\right|=N$. In Figs. B.1 and B.2 are shown the real and imaginary part, respectively, for the spectrum of the instable modes branch.

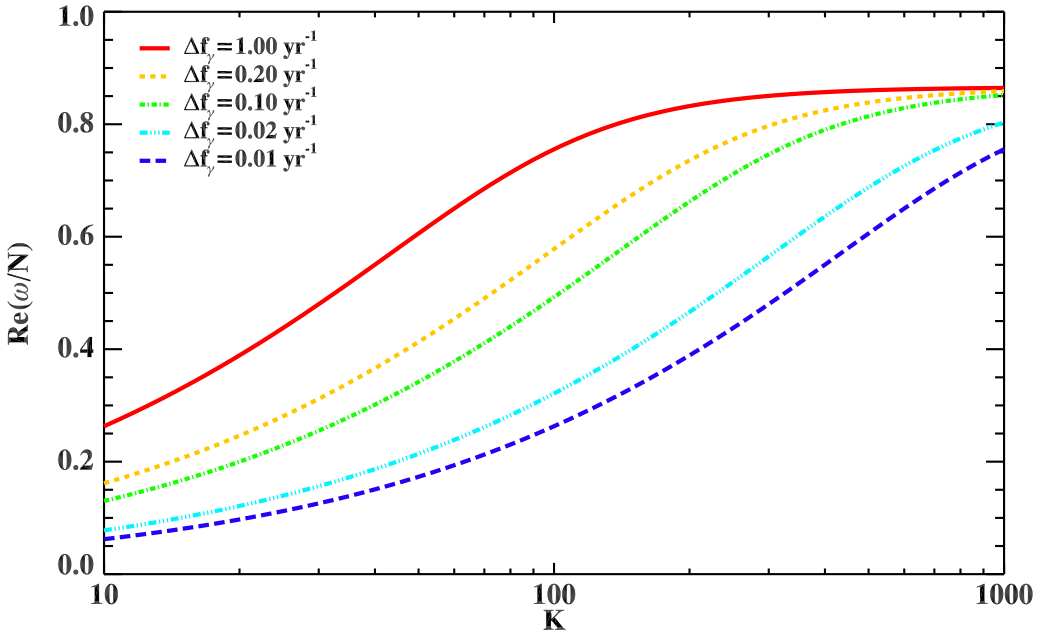

FIGURE B.1: Real part of Branch 2 solution for the dispersion relation for different values of $\Delta f = \Delta\omega/2\pi$.

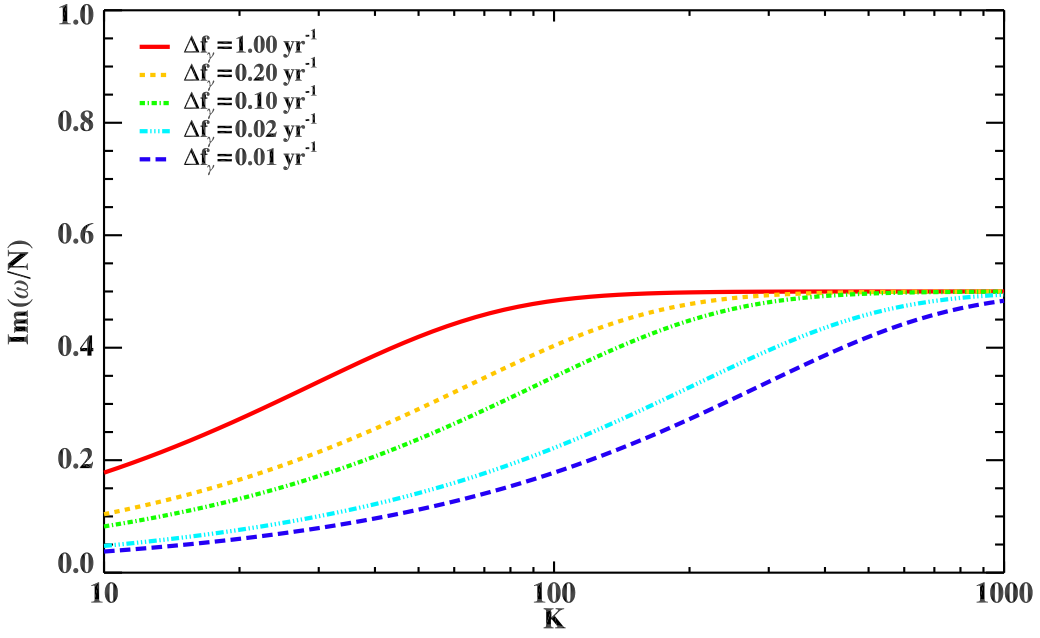

FIGURE B.2: Imaginary part of Branch 2 solution for the dispersion relation for different values of $\Delta f = \Delta\omega/2\pi$.

List of Pubblications

During my doctoral work the following articles have been published on quasi-biennial oscillations in solar neutrino flux:

- L. D'Alessi, A. Vecchio, V. Carbone, M. Laurenza and M. Storini, Quasi-Biennial Modulation of the Solar Neutrino Flux: A "Telescope" for the Solar Interior, *Journal of Modern Physics*, **4**, 49 (2013);

- A. Vecchio, L. D'Alessi, V. Carbone, M. Laurenza, M. Storini, The Empirical Mode Decomposition to Study the Quasi-Biennial Modulation of Solar Magnetic Activity and Solar Neutrino Flux, *Advances in Adaptive Data Analysis*, **4**, 1250014-1–17 (2012);

- L. D'Alessi, A. Vecchio, M. Laurenza, M. Storini and V. Carbone, Solar Neutrino Flux Modulated by Solar Activity, Proceedings of the International School of Physics "E. Fermi", ISAPP School 2011, Vol 182: "Neutrino Physics and Astrophysics", pp. 349-351, IOS Press, Amsterdam, 2012.

Bibliography

[1] J. N. Bahcall, *Neutrino Astrophysics* (Cambridge Univ. Press, Cambridge, 1989).

[2] A. Serenelli, Solar standard models, in *Neutrinos in Particle Physics, Astrophysics and Cosmology*, edited by F. J. P. Soler, C. D. Froggatt, and F. Muheim, pp. 119–145, CRC Press, Boca Raton FL, 2009.

[3] J. P. Cravens, *Solar Neutrino Measurement from the Second Phase of the Super-Kamiokande Experiment*, PhD thesis, University of California, Irvine, 2008.

[4] M. Fukugita and T. Yanagida, *Physics of Neutrinos and Applications to Astrophysics* (Springer-Verlag, 2003).

[5] J. N. Bahcall, A. M. Serenelli, and S. Basu, Astrophys.J.Suppl. **165**, 400 (2006), arXiv:astro-ph/0511337.

[6] J. N. Bahcall, A. M. Serenelli, and S. Basu, Astrophys.J. **621**, L85 (2005), arXiv:astro-ph/0412440.

[7] B. Pontecorvo, Sov.Phys.JETP **7**, 172 (1958).

[8] B. Pontecorvo, Sov.Phys.JETP **26**, 984 (1968).

[9] L. Wolfenstein, Phys.Rev. **D17**, 2369 (1978).

[10] S. Mikheyev and A. Y. Smirnov, Prog.Part.Nucl.Phys. **23**, 41 (1989).

[11] C. Giunti and W. K. Chung, *Fundamentals of Neutrino Physics and Astrophysics* (Oxford University Press, Oxford, UK, 2007).

[12] S. J. Parke, Phys.Rev.Lett. **57**, 1275 (1986).

[13] http://www.sns.ias.edu/ jnb/.

[14] KamLAND Collaboration, A. Gando *et al.*, Phys.Rev. **D83**, 052002 (2011), arXiv:1009.4771 [hep-ex].

[15] Borexino Collaboration, G. Bellini *et al.*, (2013), arXiv:1308.0443 [hep-ex].

[16] J. Davis, Raymond, D. S. Harmer, and K. C. Hoffman, Phys.Rev.Lett. **20**, 1205 (1968).

[17] B. Cleveland *et al.*, Astrophys.J. **496**, 505 (1998).

[18] SAGE Collaboration, J. Abdurashitov *et al.*, Phys.Rev. **C80**, 015807 (2009), arXiv:0901.2200 [nucl-ex].

[19] GALLEX Collaboration, P. Anselmann *et al.*, Phys.Lett. **B314**, 445 (1993).

[20] GALLEX Collaboration, P. Anselmann *et al.*, Phys.Lett. **B357**, 237 (1995).

[21] GALLEX Collaboration, W. Hampel *et al.*, Phys.Lett. **B388**, 384 (1996).

[22] GALLEX Collaboration, W. Hampel *et al.*, Phys.Lett. **B447**, 127 (1999).

[23] GNO COLLABORATION, M. Altmann *et al.*, Phys.Lett. **B616**, 174 (2005), arXiv:hep-ex/0504037.

[24] F. Kaether, W. Hampel, G. Heusser, J. Kiko, and T. Kirsten, Phys.Lett. **B685**, 47 (2010), arXiv:1001.2731 [hep-ex].

[25] Kamiokande Collaboration, Y. Fukuda *et al.*, Phys.Rev.Lett. **77**, 1683 (1996).

[26] Super-Kamiokande Collaboration, J. Hosaka *et al.*, Phys.Rev. **D73**, 112001 (2006), arXiv:hep-ex/0508053.

[27] Super-Kamiokande Collaboration, J. Cravens *et al.*, Phys.Rev. **D78**, 032002 (2008), arXiv:0803.4312 [hep-ex].

[28] Super-Kamiokande Collaboration, K. Abe *et al.*, Phys.Rev. **D83**, 052010 (2011), arXiv:1010.0118 [hep-ex].

[29] SNO Collaboration, Q. Ahmad *et al.*, Phys.Rev.Lett. **87**, 071301 (2001), arXiv:nucl-ex/0106015.

[30] SNO Collaboration, Q. Ahmad *et al.*, Phys.Rev.Lett. **89**, 011301 (2002), arXiv:nucl-ex/0204008.

[31] SNO Collaboration, S. Ahmed *et al.*, Phys.Rev.Lett. **92**, 181301 (2004), arXiv:nucl-ex/0309004.

[32] SNO Collaboration, B. Aharmim *et al.*, Phys.Rev. **C72**, 055502 (2005), arXiv:nucl-ex/0502021.

[33] SNO Collaboration, B. Aharmim *et al.*, Phys.Rev.Lett. **101**, 111301 (2008), arXiv:0806.0989 [nucl-ex].

[34] Borexino Collaboration, C. Arpesella *et al.*, Phys.Rev.Lett. **101**, 091302 (2008), arXiv:0805.3843 [astro-ph].

[35] J. N. Bahcall, Phys.Rev. **D49**, 3923 (1994), arXiv:astro-ph/9401024.

[36] J. N. Bahcall and R. M. May, Astrophys.J. **155**, 501 (1969).

[37] I. J. Iben, K. Kalata, and J. Schwartz, Ap.J. **150**, 1001 (1967).

[38] J. N. Bahcall, Astrophys.J. **139**, 318 (1964).

[39] Data availables on the web site: http://www.sns.ias.edu/ jnb/ .

[40] W. R. Sheldon, Nature **221**, 650 (1969).

[41] R. A. Donahue and S. L. Baliunas, Solar Physics **141**, 181 (1992).

[42] Y. B. Zeldovich, A. A. Ruzmaikin, and D. D. Sokoloff, *Magnetic Fields in Astrophysics* (Gordon and Breach, New York, 1983).

[43] A. Pontieri, F. Lepreti, L. Sorriso-Valvo, A. Vecchio, and V. Carbone, Solar Physics **213**, 195 (2003).

[44] K. Sakurai, Nature **278**, 146 (1979).

[45] L. J. Lanzerotti and R. S. Raghavan, Nature **293**, 122 (1981).

[46] G. A. Bazilevskaya *et al.*, Solar Physics **197**, 157 (2000).

[47] A. Vecchio and V. Carbone, The Astrophys. J. **683**, 536 (2008).

[48] J. F. Valdés-Galicia and V. M. Velasco, Advances in Space Research **41**, 297 (2008).

[49] A. Vecchio, M. Laurenza, V. Carbone, and M. Storini, The Astrophys. J. Lett. **709**, L1 (2010).

[50] A. Vecchio and V. Carbone, Astronomy & Astrophysics **502**, 981 (2009).

[51] J. F. Valdés-Galicia, R. Pérez-Enríquez, and J. A. Otaola, Solar Physics **167**, 409 (1996).

[52] K. Mursula and J. H. Vilppola, Solar Physics **221**, 337 (2004).

[53] M. Laurenza and M. Storini, Interpretation of quasi-periodic variations in solar cosmic ray data, in *Proceedings of the 31st ICRC, LÓDŹ*, 2009.

[54] M. Laurenza, A. Vecchio, V. Carbone, and M. Storini, Quasi-biennial Modulation of Galactic Cosmic Rays, 2012, in press.

[55] M. Laurenza, M. Storini, S. Giangravè, and G. Moreno, Journal of Geophysical Research (Space Physics) **114**, 1103 (2009).

[56] J. Javaraiah, R. K. Ulrich, L. Bertello, and J. E. Boyden, Solar Physics **257**, 61 (2009), arXiv:0903.4031 [astro-ph.SR].

[57] R. J. Davis and J. C. Evans, Experimental limits on extraterrestrial sources of neutrinos, in *Proceedings of 13th International Conference on Cosmic Rays* Vol. 3, pp. 2001–2006, 1973.

[58] Y. Fukuda *et al.*, Physical Review Letters **81**, 1158 (1998), arXiv:hep-ex/9805021.

[59] L. M. Krauss, Nature **348**, 403 (1990).

[60] J. N. Bahcall and W. H. Press, The Astrophys. J. **370**, 730 (1991).

[61] D. S. Oakley, H. B. Snodgrass, R. K. Ulrich, and T. L. Vandekop, The Astrophys. J. Lett. **437**, L63 (1994).

[62] R. L. McNutt, Jr., Science **270**, 1635 (1995).

[63] R. M. Wilson, The Astrophys. J. **545**, 532 (2000).

[64] P. Sturrock, The Astrophys. J. Lett. **688**, L53 (2008), arXiv:0810.2755.

[65] O. G. Miranda, T. I. Rashba, A. I. Rez, and J. W. Valle, Phys Rev D **70**, 113002 (2004), arXiv:hep-ph/0406066.

[66] P. Bamert, C. P. Burgess, and D. Michaud, Nuclear Physics B **513**, 319 (1998), arXiv:hep-ph/9707542.

[67] C. P. Burgess, N. S. Dzhalilov, T. I. Rashba, V. B. Semikoz, and J. W. F. Valle, Mon.Not.Roy.Astron.Soc. **348**, 609 (2004), arXiv:astro-ph/0304462.

[68] A. Vecchio, L. D'Alessi, V. Carbone, M. Laurenza, and M. Storini, Advances in Adaptive Data Analysis **4**, 1250014 (2012).

[69] L. D'Alessi, A. Vecchio, M. Laurenza, M. Storini, and V. Carbone, Solar neutrino flux modulated by solar activity, in *Proceedings of the International School of Physics 'E. Fermi', Vol.182: Neutrino Physics and Astrophysics* Vol. 182, pp. 349–351, IOS Press, Amsterdam, 2012.

[70] R. Davis, Private communication, 2004.

[71] D. M. Simpson, A. F. C. Infantosi, and D. A. Botero-Rosas, Medical and Biological Engineering and Computing **39**, 428 (2001).

[72] Fletcher *et al.*, The Astrophys. J. Lett. **718**, L19 (2010), arXiv:1006.4305 [astro-ph.SR].

[73] Particle Data Group, J. Beringer *et al.*, Phys.Rev. **D86**, 010001 (2012).

[74] A. H. Compton and I. A. Getting, Phys. Rev. **47**, 817 (1935).

[75] Super-Kamiokande Collaboration, G. Guillian *et al.*, Phys.Rev. **D75**, 062003 (2007), arXiv:astro-ph/0508468.

[76] Tibet AS-gamma Collaboration, M. Amenomori, Science **314**, 439 (2006), arXiv:astro-ph/0610671.

[77] A. Abdo *et al.*, Astrophys.J. **698**, 2121 (2009), arXiv:0806.2293 [astro-ph].

[78] IceCube Collaboration, R. Abbasi *et al.*, Astrophys.J. **746**, 33 (2012), arXiv:1109.1017 [hep-ex].

[79] M. Aartsen *et al.*, (2012), arXiv:1210.5278 [astro-ph.HE].

[80] IceCube Collaboration, R. Abbasi *et al.*, Astrophys.J. **718**, L194 (2010), arXiv:1005.2960 [astro-ph.HE].

[81] Figure from the web site: http://icecube.wisc.edu/ desiati/activity/anisotropy-/large/.

[82] Tibet AS Gamma Collaboration, M. Amenomori *et al.*, Phys.Rev.Lett. **93**, 061101 (2004), arXiv:astro-ph/0408187.

[83] K. Munakata *et al.*, Astrophys.J. **712**, 1100 (2010), arXiv:0911.1165 [astro-ph.HE].

[84] MACRO Collaboration, M. Ambrosio *et al.*, Astropart.Phys. **7**, 109 (1997).

[85] MACRO Collaboration, M. Ambrosio *et al.*, (2002), arXiv:hep-ex/0206027.

[86] MACRO Collaboration, M. Ambrosio *et al.*, Nucl.Instrum.Meth. **A486**, 663 (2002).

[87] for the LVD Collaboration, M. Selvi, Analysis of the seasonal modulation of the cosmic muon flux in the LVD detector during 2001-2008, in *Proc. 31st ICRC*, 2009.

[88] MINOS Collaboration, P. Adamson *et al.*, Phys.Rev. **D81**, 012001 (2010), arXiv:0909.4012 [hep-ex].

[89] Borexino Collaboration, G. Bellini *et al.*, JCAP **1205**, 015 (2012), arXiv:1202.6403 [hep-ex].

[90] Super-Kamiokande Collaboration, Y. Oyama, p. 33 (2006), arXiv:astro-ph/0605020.

[91] E. Fernandez-Martinez and R. Mahbubani, JCAP **1207**, 029 (2012), arXiv:1204.5180 [astro-ph.HE].

[92] I. Durre, R. S. Vose, and D. B. Wuertz, J.Climate **19**, 53 (2006).

[93] P. A. Dirac, Nature **139**, 323 (1937).

[94] P. A. Dirac, Proc.Roy.Soc.Lond. **A165**, 199 (1938).

[95] W. Marciano, Lect.Notes Phys. **648**, 97 (2004).

[96] J. D. Barrow, Astrophys.Space Sci. **283**, 645 (2003), gr-qc/0209080.

[97] C. Brans and R. Dicke, Phys.Rev. **124**, 925 (1961).

[98] S. Bize *et al.*, Lect.Notes Phys. **648**, 189 (2004), astro-ph/0310112.

[99] . Kramer, Michael, Lect.Notes Phys. **648**, 33 (2004), astro-ph/0405178.

[100] M. T. Murphy, J. Webb, and V. Flambaum, Mon.Not.Roy.Astron.Soc. **345**, 609 (2003), arXiv:astro-ph/0306483.

[101] J. A. King *et al.*, Mon.Not.Roy.Astron.Soc. **422**, 3370 (2012), arXiv:1202.4758 [astro-ph.CO].

[102] S. S. Vogt *et al.*, HIRES: the high-resolution echelle spectrometer on the Keck 10-m Telescope, in *Instrumentation in Astronomy VIII*, edited by D. L. Crawford and E. R. Craine, , Society of Photo-Optical Instrumentation Engineers (SPIE) Conference Series Vol. 2198, p. 362, 1994.

[103] http://www2.keck.hawaii.edu/inst/hires/ .

[104] H. Dekker, S. D'Odorico, A. Kaufer, B. Delabre, and H. Kotzlowski, Design, construction, and performance of UVES, the echelle spectrograph for the UT2 Kueyen Telescope at the ESO Paranal Observatory, in *Optical and IR Telescope Instrumentation and Detectors*, edited by M. Iye and A. F. Moorwood, , Society of Photo-Optical Instrumentation Engineers (SPIE) Conference Series Vol. 4008, pp. 534–545, 2000.

[105] M. T. Murphy, *Probing variations in the fundamental constants with quasar absorption lines*, PhD thesis, Institute of Astronomy, University of Cambridge, 2002.

[106] http://astronomy.swin.edu.au/ mmurphy/research/are-natures-laws-really-universal/ .

[107] V. Dzuba, V. Flambaum, and J. Webb, Phys.Rev. **A59**, 230 (1999), arXiv:physics/9808021.

[108] V. Dzuba, V. Flambaum, and J. Webb, Phys.Rev.Lett. **82**, 888 (1999), arXiv:physics/9802029.

[109] M. T. Murphy, J. K. Webb, and V. V. Flambaum, Phys.Rev.Lett. **99**, 239001 (2007), 0708.3677.

[110] Keck and VLT data available at web site: http://astronomy.swin.edu.au/ mmurphy/refereed-journal-articles/ .

[111] Z. Wu and N. E. Huang, Royal Society of London Proceedings Series A **460**, 1597 (2004).

[112] WMAP Collaboration, G. Hinshaw *et al.*, Astrophys.J.Suppl. **180**, 225 (2009), 0803.0732.

[113] Y. Fujii, Lect.Notes Phys. **648**, 167 (2004), hep-ph/0311026.

[114] Y. Fujii, Phys.Lett. **B573**, 39 (2003), arXiv:astro-ph/0307263.

[115] OPERA Collaboration, T. Adam *et al.*, arXiv:1109.4897v2 [hep-ex].

[116] Huang *et al.*, Royal Society of London Proceedings Series A **454**, 903 (1998).

[117] D. A. T. Cummings *et al.*, Nature **427**, 344 (2004).

[118] J. Terradas, R. Oliver, and J. L. Ballester, The Astrophys. J. **614**, 435 (2004).

[119] Huang *et al.*, Royal Society of London Proceedings Series A **459**, 2317 (2003).

[120] OPERA Collaboration, T. Adam *et al.*, JHEP **1210**, 093 (2012), arXiv:1109.4897 [hep-ex].

[121] OPERA Collaboration, T. Adam *et al.*, JHEP **1301**, 153 (2013), arXiv:1212.1276 [hep-ex].

[122] OPERA Collaboration, M. Dracos, Nucl.Phys.Proc.Suppl. **235-236**, 283 (2013).

[123] Borexino Collaboration, P. Alvarez Sanchez *et al.*, Phys.Lett. **B716**, 401 (2012), arXiv:1207.6860 [hep-ex].

[124] LVD Collaboration, N. Y. Agafonova *et al.*, Phys.Rev.Lett. **109**, 070801 (2012), arXiv:1208.1392 [hep-ex].

[125] M. Antonello *et al.*, JHEP **1211**, 049 (2012), arXiv:1208.2629 [hep-ex].

[126] J. N. Bahcall and M. Pinsonneault, Rev.Mod.Phys. **67**, 781 (1995), arXiv:hep-ph/9505425.

[127] M. Stix, *The Sun* (Springer-Verlag, Berlin, 1989).

[128] http://functions.wolfram.com/HypergeometricFunctions/MeijerG/.

[129] H. Bateman and A. Erdelyi, *Higher Trancendental Functions, Vol. 1* (McGraw-Hill, New York, 1953).

[130] G. N. Watson, Trans. Camb. Phil. Soc. **22**, 277 (1918).

[131] C. P. Burgess, N. S. Dzhalilov, T. I. Rashba, V. B. Semikoz, and J. W. F. Valle, MNRAS **348**, 609 (2004), arXiv:astro-ph/0304462.